

# **Development of Beam Halo Monitors for the European XFEL using radiation hard sensors and Demonstration of the Technology at FLASH**

Von der Fakultät für Mathematik, Naturwissenschaften und Informatik  
der Brandenburgischen Technischen Universität Cottbus-Senftenberg

zur Erlangung des akademischen Grades

Doktor der Naturwissenschaften  
(Dr. rer. nat.)

genehmigte Dissertation

vorgelegt von

Diplom-Physiker

Alexandr Ignatenko

Geboren am 10. November 1980 in Minsk

Gutachter: Prof. Dr. Wolfgang Lohmann

Gutachter: Prof. Dr. Andreas Jankowiak

Gutachter: Prof. Dr. Jürgen Reif

Tag der mündlichen Prüfung: 7. November 2014



# Erklärung über frühere Promotionsanträge

Hiermit versichere ich, dass ich bisher noch keinen Antrag für ein Promotionsverfahren eingereicht habe.

Cottbus, den 14.04.2014

Alexandr Ignatenko



# Selbständigkeitserklärung

Hiermit versichere ich, dass ich die vorliegende Arbeit selbständig und nur unter Verwendung der angegebenen Quellen und Hilfsmittel angefertigt habe.

Cottbus, den 14.04.2014

Alexandr Ignatenko



# Erklärung zu Schutzrechten

Hiermit versichere ich, dass die Veröffentlichung der Dissertation keine bestehenden Schutzrechte verletzt.

Cottbus, den 14.04.2014

Alexandr Ignatenko





## **Abstract**

The **E**uropean **X**-Ray **F**ree-**E**lectron **L**aser (E-XFEL), currently under construction in Hamburg, Germany, is intended to be an international linear accelerator (linac) based user facility. Its electron beam can carry maximal average power of 600 kW. A beam with such a high power needs to be carefully transmitted through the machine and safely dumped after utilization. This is supported by various diagnostics tools. A Beam Halo Monitor (BHM) based on synthetic diamond and sapphire sensors has been designed.

Diamond sensors are developed by the company element6 for the detection of ionizing radiation and used previously elsewhere. Sapphire sensors are in this thesis applied for the first time.

The BHM concept has been applied already at the **F**ree-**e**lectron **L**aser in **H**amburg (FLASH). A module with four diamond and four sapphire sensors was designed, installed inside the beam pipe, commissioned, calibrated and has been successfully operated for 4 years. The system contributed significantly to safe and efficient operation of FLASH.

Both types of the sensors for the BHM were characterized. Measurements of radiation tolerance are done in a 10 MeV electron beam for polycrystalline CVD (pCVD) diamond sensors for the first time up to a dose of 10 MGy and for sapphire sensors up to 5 MGy. The charge collection efficiency (CCE) drops as a function of the absorbed dose, is however still sufficient for application as a BHM.

To improve a main sensor characteristic, the charge collection efficiency, for sapphire sensors the impurity concentration was reduced and different growth techniques were compared. Finally, charge collection efficiency of about 5 % for a bias voltage of 500 V was reached.

The BHM concept for the XFEL is designed and in the construction phase.

## Kurzfassung

Der European X-Ray Free-Electron Laser (E-XFEL), dessen Aufbau zur Zeit in Hamburg stattfindet, soll als international organisierte LINAC basierte Strahlungsquelle für Nutzer betrieben werden. Die mittlere Leistung im Elektronenstrahl wird 600 kW betragen. Ein Strahl mit so hoher Leistung muss sicher durch den Beschleuniger gesteuert, und nach seiner Nutzung sicher am vorgesehenen Ort vernichtet werden. Die Führung des Strahls wird von verschiedenen Diagnoseinstrumenten unterstützt. Hierzu zählt ein Beam Halo Monitor, der Sensoren aus hochreinem Diamant- und Saphirkristallen nutzt. Diamantsensoren wurden speziell für den Nachweis ionisierender Strahlung von der Firma Element6 entwickelt und wurden bereit an anderen Beschleunigern verwendet. Saphiresensoren werden in dieser Arbeit zum ersten Mal von verschiedenen Herstellern getestet und verwendet.

Das Konzept eines solchen Beam Halo Monitors wurde im Rahmen dieser Arbeit bereits beim Free-Electron Laser in Hamburg (FLASH) entwickelt und angewandt. Hier wurde ein Modul mit jeweils 4 Diamant- und 4 Saphirsensoren installiert, in Betrieb genommen und getestet. Seit nunmehr 4 Jahren ist es ohne Ausfall in Betrieb und hat in dieser Zeit signifikant zur Erhöhung der Effizienz von FLASH beigetragen.

Vor dem Einbau bei FLASH wurden beide Sensortypen charakterisiert. Polykristalline CVD (pCVD) Diamantsensoren wurden in einem 10 MeV Elektronenstrahl mit bis zu 10 MGy und Saphirsensoren bis zu 5 MGy Dosis getestet. Die sogenannte Charge Collection Efficiency (CCE) fällt dabei in Abhängigkeit von der applizierten Dosis ab, bleibt aber immer noch ausreichend hoch, so dass die Sensoren für einen BHM verwendet werden können.

Ferner wurde der Einfluss der Reinheit von Saphirsensoren auf die Charge Collection Efficiency untersucht. Die Konzentration Verunreinigungen wurde bei Auswahl der Sensoren verringert, und verschiedene Herstellungsverfahren wurden betrachtet. Im Resultat konnten Sensoren mit einer Charge Collection Efficiency von 5% bei einer Spannung von 500 V hergestellt werden.

Das Konzept für den XFEL ist entwickelt und bereits in der Phase der Realisierung.



# Contents

Abbreviations .....	vi
1 Introduction .....	1
2 Linac-based Free-electron Lasers .....	3
2.1 Basic principles of FEL radiation .....	5
2.2 European XFEL .....	10
2.3. FLASH .....	12
3 Beam Diagnostics .....	14
3.1 Unwanted conditions in particle accelerators .....	14
3.2 Standard beam diagnostics .....	16
3.2.1 Beam profile measurements .....	16
3.2.2 Beam position measurements .....	20
3.2.3 Bunch charge measurements .....	22
3.2.4. Beam loss monitoring .....	24
3.2.4.1 Ionization chambers .....	24
3.2.4.2 PIN diodes .....	26
3.2.4.3 Secondary emission monitors (SEMs) .....	27
3.2.4.4 Scintillator BLM .....	27
3.2.4.5 Cherenkov BLMs .....	28
3.3. Beam halo monitors (BHMs) .....	29
4 Radiation Hard Sensors .....	30
4.1 Working principle of solid state sensors .....	300
4.2 Interaction of charged particles with matter .....	32
4.3 Interaction of photons with matter .....	36
4.4 Energy deposition and signal creation .....	37

4.5 Polarization and pumping .....	40
4.6 Sensor characterization .....	44
4.6.1 The IV setup.....	44
4.6.2 The CCE setup .....	45
4.6.3 The setup for radiation hardness tests .....	47
4.7 Diamond sensors.....	48
4.7.1 Material and metallization.....	49
4.7.2 Sensor characterization .....	51
4.7.3 Beam profile measurements.....	54
4.8. Sapphire sensors .....	58
4.8.1. Material and metallization.....	59
4.8.2 Characterization of sensors from different manufacturers.....	62
4.8.3 Prototype of the sapphire beam condition monitor.....	64
5 Beam Halo Monitor at FLASH .....	66
5.1 FLASH beam dump line .....	66
5.2 BHM description.....	68
5.3 Commissioning and first tests.....	71
5.4 Calibration .....	76
5.5 BHM for FLASH2 .....	82
6 BHM for the European XFEL .....	84
6.1 Location and tasks .....	84
6.2 Description of the BHM for the E-XFEL .....	88
6.3 The MPS and BHM alarm signals .....	92
6.3.1 MPS system.....	92
6.3.2 BHM alarm signals .....	95
6.4. Calibration procedure .....	96
7 Summary and Conclusions .....	99
7.1 Summary.....	99
7.1.1 Development of diamond and sapphire sensors.....	99
7.1.2 Beam Halo Monitor for the European XFEL.....	100
7.2 Conclusions.....	100
Bibliography .....	101

# Abbreviations

ADC	Analog-to-Digital Converter
ALS	Advanced Light Source
AMC	Advanced Mezzanine Card
APS	Advanced Photon Source
ASEM	Aluminium Cathode Electron Multiplier
BC	Bunch Compressor
BCM	Beam Conditions Monitor
BESSY	Berlin Electron Storage Ring Society for Synchrotron Radiation
BHM	Beam Halo Monitor
BLM	Beam Loss Monitor
BPM	Beam Position Monitor
CCE	Charge Collection Efficiency
COTR	Coherent Optical Transition Radiation
CVD	Chemical Vapor Deposition
DAC	Digital-to-Analog Converter
DC	Direct Current
DESY	Deutsches Elektronen-Synchrotron
DORIS	Doppel-Ring Speicher, Double-Ring Storage
EEHG	Echo-Enabled Harmonic Generation
EFG	Edge-defined Film-fed Growth
EM	Electromagnetic
ENC	Equivalent Noise Charge
ESRF	European Synchrotron Radiation Facility
E-XFEL	European X-ray Free-electron Laser
FEL	Free-Electron Laser
FLASH	Free-electron Laser in Hamburg
FPGA	Field-Programmable Gate Array
FWHM	Full Width at Half Maximum
GEANT	Geometry and Tracking Software Package
GSI	Gesellschaft für Schwerionenforschung
HHG	High-order Harmonic Generation
HGHG	High-Gain Harmonic Generation
HPHT	High Pressure High Temperature

INJ	Injector
IV	Current-Voltage
LCLS	Linac Coherent Light Source
linac	Linear Accelerator
MIP	Minimum Ionizing Particle
MPS	Machine Protection System
OTR	Optical Transition Radiation
pCVD	Polycrystalline CVD
PETRA	Positron-Electron Tandem Ring Accelerator
PITZ	Photoinjector Test Facility in Zeuthen
PMT	Photomultiplier Tube
ppb	Parts per billion
RF	Radio Frequency
RTM	Rear Transition Module
SASE	Self-Amplified Spontaneous Emission
S-DALINAC	Superconducting Darmstadt Linear Accelerator
SEM	Secondary Emission Monitor
SPring-8	Super Photon ring 8 GeV
SR	Synchrotron Radiation
TCA	Telecommunications Computing Architecture
TDS	Transverse Deflecting Structure
TE	Transverse Electric
TESLA	TeV-Energy Superconducting Linear Accelerator
TM	Transverse Magnetic
TR	Transition Radiation





# Chapter 1

## Introduction

Scattering experiments, starting with the one by Geiger and Marsden in 1909 using alpha particles leading to Rutherford's model of the atom, became a key technology to understand the structure of matter. To resolve smaller structures high energy particle beams were needed, stimulating the development of particle accelerators.

Our current understanding of the basic constituents of matter was only possible by the impressing development of accelerator technologies. In the 1920 van-de-Graaf and Cockcroft-Walton machines allowed particle acceleration up to MeV. The first circular accelerator was the cyclotron, invented by Lawrence. A major breakthrough was the development of the synchrotron using strong focusing by Weksler and McMillan. Many fundamental discoveries are made using synchrotrons, recently the Higgs boson at LHC.

When electrons are accelerated in synchrotrons, they radiate synchrotron radiation, due to the acceleration of a circular orbit. For particle physicists this phenomenon was limiting the particle energy.

However, synchrotron radiation became interesting for the research in a variety of disciplines like surface science, semiconductor physics, materials science, atomic and molecular physics, chemistry, biology and medicine. Hence, special synchrotrons were built specifically for this research.

To enhance the intensity and energy of synchrotron radiation special technologies are developed using linear accelerators. Electron bunches are forced on a slalom paths in special magnets (undulators) to emit laser light, called free-electron lasers (FELs). For the stable operation of these accelerators beam diagnostics is of paramount importance. Sensors for beam diagnostics have to be installed near or in the beam-pipe, and must tolerate harsh radiation fields.

Diamond is one of the hardest substances on earth with other exceptional properties. A high radiation resistance was expected from its stable lattice and was demonstrated by irradiation experiments with different particle types. Two decades ago the advent of a production technology capable of manufacturing synthetic diamond of good quality, chemical vapor

deposition method (CVD), made the employment of diamond for sensor applications conceivable. Nevertheless, CVD diamonds were and still remain rather expensive; therefore the search of an alternative radiation tolerant sensor material is still an issue. Sapphire is a material that has drawn attention. It is a promising sensor material which is industrially produced.

This thesis deals with both the development of sensor materials and their application in the beam halo monitor (BHM) for the European XFEL (E-XFEL) [1.1, 1.2] based on polycrystalline CVD (pCVD) diamonds and synthetic sapphires. This monitor will be operated in the dump regions of this facility and has to withstand extreme radiation conditions due to beam halo coming with high duty cycle. The development is based on the experience gained during operation of the BHM installed in the dump area of Free-electron LASer in Hamburg (FLASH) [1.3, 1.4]. For this development in addition to the diamond detectors, sapphires are used. Therefore one of the tasks within this thesis was, to find synthetic sapphires with proper radiation hardness and electronic properties that make them suited as a sensor.

The thesis is organized in 7 chapters including this introduction. Chapter 2 gives an overview of the accelerator-based light sources and concentrates on the linac-based free-electron lasers (FEL) among them. The principle of the FEL radiation generation is introduced. Two FEL facilities – FLASH, already in operation since the year 2005, and the E-XFEL, being under construction at the time of writing, are described. The focus of chapter 3 is on beam diagnostics instruments for particle accelerators. The BHM is first introduced there as a novel beam dump diagnostics system. Chapter 4 is devoted to radiation hard sensors. The chapter starts with the principle of operation of solid state sensors. It covers the mechanisms of interaction with matter for charged particles and photons, their energy loss. Relation of the energy loss to energy deposition and mechanism of signal generation are described. The methods of sensor characterization and quality criteria are given. The results of characterization of pCVD diamonds and synthetic sapphires grown by different methods are adduced. At the end of the chapter a prototype of the sapphire sensor and the results of the first tests are given. Chapter 5 describes the BHM at FLASH, the experience gained during operation, calibration procedure and results. The BHM for the E-XFEL is presented in chapter 6. The BHM design, readout electronics, data acquisition procedure, alarm signals generation algorithms are under consideration there. Chapter 7 gives the summary of the thesis.

## Chapter 2

# Linac-based Free-electron Lasers

Accelerator-based light sources (later in the thesis referred to as simply light sources) are the largest and most successful scientific user facilities, serving the experiments of tens of thousands users each year. These important facilities provide a broad spectrum of research opportunities in diverse fields, including physics, chemistry, pharmaceuticals, medicine, geology, biology and materials science.

An important benchmark of the potential and quality of a light source is its brilliance. This is a measure of the number of photons generated in a specific wavelength range normalized to the beam size and the beam divergence, the latter described by a quantity called emittance. Four generations of accelerator-based light sources are distinguished.

Soon after it was realized that synchrotron radiation (SR) is not only an unwanted by-product in electron synchrotrons the light sources of the first generation appeared. These were synchrotrons developed for high energy physics research with parasitic utilization of SR emitted in the bending magnets. Later also partly dedicated and even fully dedicated to SR production storage rings still using the bending magnets were built.

The second generation light sources were already dedicated facilities where radiation is generated both by means of the bending magnets used to hold particles on their course, and also in special long magnet structures, an arrangement of alternating magnets – wigglers. Like in a bending magnet, in a wiggler the trajectory of particle bends. Due to more bends in the periodic structure the particles are forced to oscillate many times while propagating through the wiggler. Compared to a single magnet the brilliance is enhanced by a factor of  $N_w$  – the number of alternating magnet periods in the wiggler.

The third generation is custom-built storage rings which, due to small beam cross section and systematic use of undulators, are able to produce light with brilliance several orders of magnitude larger than their predecessors. The undulator is also an arrangement of alternating magnets. Unlike in a bending magnet, in an undulator the radiation emitted by a single particle in one period of the structure can interfere constructively for a given wavelength with the

radiation emitted in another period. The brilliance is then scaled with the number of undulator periods  $N_u^2$ .

The fourth generation light sources deploy the so-called Free-Electron laser (FEL) principle. Such facilities are driven by linear accelerators equipped with high-precision injectors. They give substantially more freedom in choosing time structure and shape of the beam. They can provide highly coherent radiation with the peak brilliance of 6-8 orders of magnitude larger than that of the conventional sources of the third generation.

The devices for different generations of the light sources and the characteristics of the emitted radiation are schematically shown in Figure 2.0.1. SR produced in the bending magnets has a broad continuous energy spectrum. The energy spectrum of SR produced in a wiggler or an undulator peaks around a certain main wavelength and its harmonics. The peak for an undulator is narrower than the one for a wiggler. It gets narrower with the increasing number of the undulator periods, and even more when the FEL process develops and the so-called microbunching occurs. More information about the FEL radiation is given in section 2.1 of this chapter.

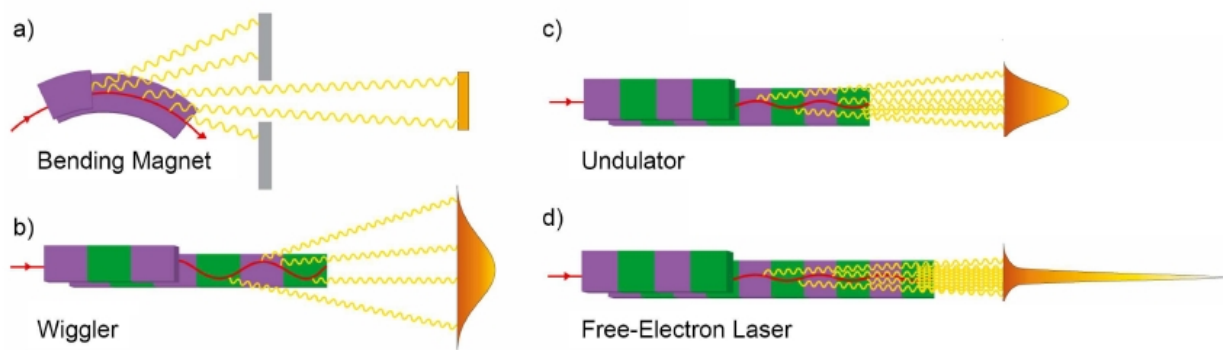


Figure 2.0.1: The devices for different generations of light sources and the characteristics of the emitted radiation: a) bending magnet, b) wiggler, c) short undulator for a third generation light source, d) long undulator for a FEL. To the right of each picture the spectrum of radiation produced by the device is schematically shown.

Figure 2.0.2 illustrates the peak brilliance as a function of the photon energy of different generations of light sources. The typical peak brilliance of a second generation light source using a bending magnet and a wiggler is compared with the one of various light sources from the third and fourth generations. Examples of the light sources of the second generation are DORIS in Hamburg [2.0.1, 2.0.2] and BESSY I in Berlin [2.0.3, 2.0.4]. The third generation light sources are PETRA III in Hamburg [2.0.5, 2.0.6, 2.0.7], BESSY II, Advanced Light Source (ALS) in Berkeley, USA [2.0.8, 2.0.9], Advanced Photon Source (APS) in Argonne, USA [2.0.10, 2.0.11], SPring-8 in Sayo-cho, Japan [2.0.12, 2.0.13], ESRF in Grenoble, France [2.0.14, 2.0.15]. LCLS in Stanford, USA [2.0.16, 2.0.17], FLASH and European XFEL in Hamburg are the light sources of the fourth generation.

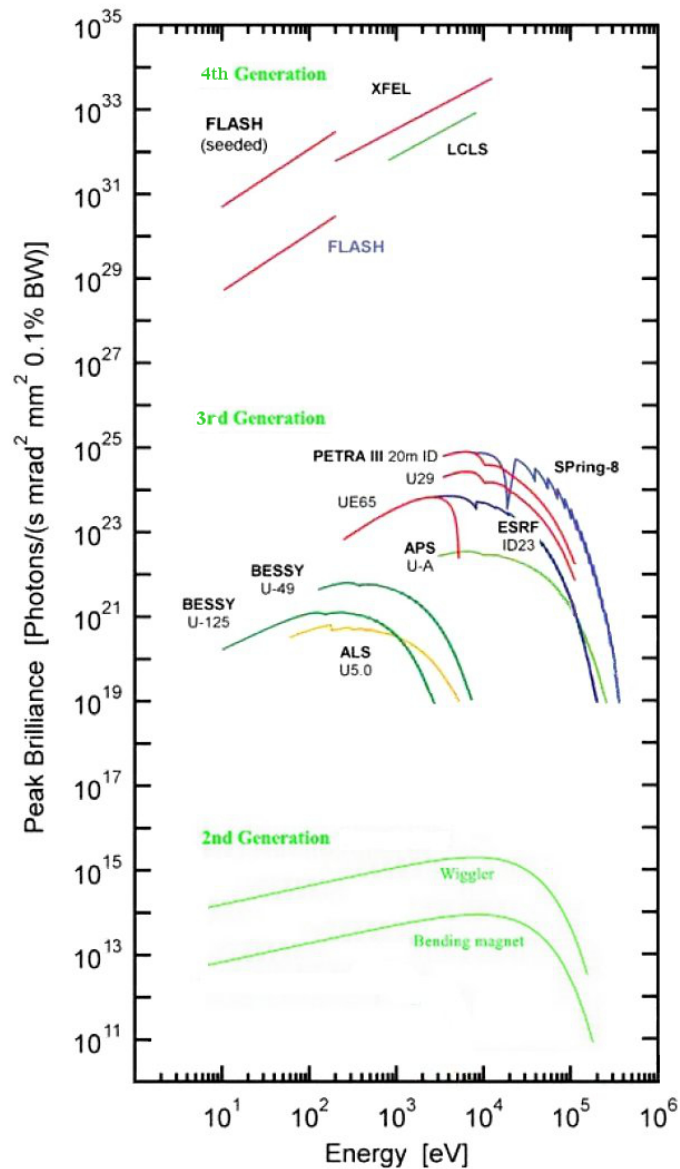


Figure 2.0.2: Peak brilliance of the light sources from the fourth generation in comparison with that for the third and the second generation light sources. According to the data taken from [2.0.18] and [2.0.19].

## 2.1 Basic principles of FEL radiation

The principle of the free-electron laser was first introduced in 1971 when J.M.J. Madey suggested the “stimulated emission of bremsstrahlung in a periodic magnetic field” [2.1.1] as a mechanism to generate radiation of high power in an undulator structure. In 1976 the applicability of the theory was demonstrated by a group from Stanford University [2.1.2].

The word “laser” is an acronym for light amplification by stimulated emission of radiation. A conventional quantum laser consists of three basic components: a laser medium with at least

three energy levels, an energy pump, and an optical resonator. Stimulated emission takes place between an excited state  $E_2$  and the ground state  $E_1$ . A higher level  $E_3$  is needed to achieve a population inversion by pumping many electrons from  $E_1$  to  $E_3$  from where they make a fast transition to  $E_2$ . The axis of the optical cavity defines the direction of the photon beam. In a mono-mode laser exactly one optical eigenmode of the cavity is excited. The photons in this mode are all in the same quantum state, and the probability for stimulated emission from  $E_2$  to  $E_1$  is proportional to the number of photons present in this state.

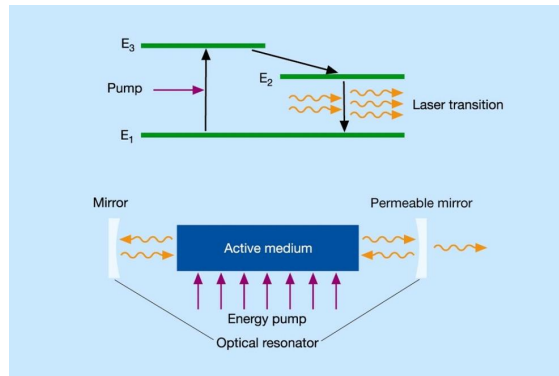


Figure 2.1.1: Principle of conventional laser.  $E_1$ ,  $E_2$ ,  $E_3$  are the electron energy levels. The mirrors form the optical resonator.

In a free-electron laser the role of the active laser medium and the energy pump are both taken over by a relativistic electron beam. The electrons are not bound to atomic, molecular or solid-state levels but are moving freely in the vacuum. The pump source is the large kinetic energy of the electrons. Stimulated emission takes place from higher to lower kinetic energies under the action of an initial, already existing light wave.

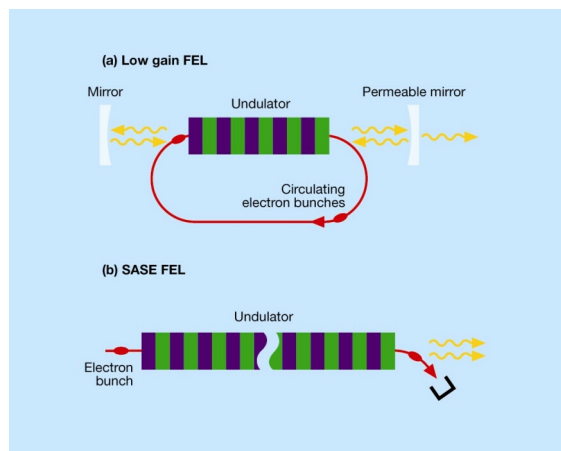


Figure 2.1.2: Principle of free-electron laser: a) low-gain FEL for infrared or visible light, b) high-gain single-pass FEL, self-seeding scheme as an example.

The motion of the electrons on their slalom path produces a velocity component along the transverse electric field of the light wave, resulting in an energy exchange between the electrons and the light wave. Specifically, the coupling between the electron and the light wave is proportional to the electric field strength of the wave, and the FEL gain is proportional to the number of photons in the light wave. Hence it is well justified to speak of light amplification by stimulated emission of radiation in a free-electron laser. Moreover, the light emerging from an FEL has the same properties as conventional laser light in that a huge number of coherent photons are contained in a single optical mode.

The basic principle of the free-electron laser can be described within the standard picture for the generation of SR. While travelling with relativistic velocity through the undulator, the electrons propagate along a sinusoidal path and emit SR in a narrow cone in the forward direction. The typical opening angle of the cone is:

$$\frac{1}{\gamma} = \frac{m_e c^2}{E_e}, \quad (2.1.1)$$

where  $\gamma$  is Lorentz factor,  $m_e$  and  $E_e$  are the electron mass and electron energy respectively. In the undulator, the deflection of the electrons from the forward direction is comparable to the opening angle of the synchrotron radiation cone. Thus the radiation generated by the electrons while travelling along the individual magnetic periods overlaps. This interference effect is reflected in the formula for the wavelength  $\lambda_l$  of the first harmonic of the spontaneous on-axis undulator emission:

$$\lambda_l = \frac{\lambda_u}{2\gamma^2} \left(1 + \frac{K^2}{2}\right), \quad (2.1.2)$$

where  $\lambda_u$  is the length of the magnetic period of the undulator and  $K$  is the strength parameter:

$$K = \frac{eB\lambda_u}{2\pi m_e c}, \quad (2.1.3)$$

where  $B$  is peak magnetic field in the undulator. Equation 2.1.2 gives the wavelength of light seen by the observer in the laboratory and incorporates the relativistic length contraction of the undulator and the relativistic Doppler effect of the radiation.

To achieve light amplification, the electron energy must exceed the resonance energy

$$E > E_r = \gamma_r m_e c^2, \quad (2.1.4)$$

where the resonant Lorentz factor is defined as

$$\gamma_r = \sqrt{\frac{\lambda_u}{2\lambda_l} \left(1 + \frac{K^2}{2}\right)}. \quad (2.1.5)$$

The interference condition (2.1.2) basically means that, while travelling along one period of the undulator, the electrons slip by one radiation wavelength with respect to the faster electromagnetic field. This is one of the prerequisites to obtain high gain in the FEL process. The other criteria are good electron beam quality and a sufficient overlap between radiation

pulse and electron bunch along the undulator. To achieve that one needs low emittance, low energy spread electron beam with an extremely high charge density in conjunction with a very precise magnetic field and accurate beam steering through the undulator. This is described by the gain length  $L_g$  (e-folding length) - a key quantity for the high-gain FEL:

$$L_g = \frac{1}{\sqrt{3}} \left( \frac{2m_e c \lambda_u}{\mu_0 e K^2} \cdot \frac{\gamma \varepsilon \beta}{I_{peak}} \right)^{1/3}, \quad (2.1.6)$$

where  $\mu_0$  is the magnetic permeability,  $\varepsilon$  – the electron beam emittance,  $\beta$  – the beta function and  $I_{peak}$  – the peak current.

Oscillating through the undulator, the electron bunch interacts with its own electromagnetic field created via spontaneous emission. Depending on the relative phase between radiation and electron oscillation, electrons experience either a deceleration or acceleration. Electrons that are in phase with the electromagnetic wave are retarded while the ones with opposite phase gain energy. Through this interaction a longitudinal fine structure, the so-called microbunching, is established which amplifies the electromagnetic field.

The principle of FEL radiation generation works well for a wide spectral range - from infrared to hard ultraviolet and X-ray regions. For infrared and visible wavelengths the low-gain FEL scheme can be realized as shown in Figure 2.1.2 a. Its main components are an electron storage ring or a recirculating linear accelerator, a short undulator and an optical cavity with mirrors. The initial light wave is generated by an external source and captured into an eigenmode of the cavity. The bunches take many turns in the machine. A gain of a few percent for each passage through the short undulator is achieved. Laser saturation, however does not prevent the FEL from reaching high output power, if the beam makes a sufficiently large number of turns. For ultraviolet and X-ray FELs mirrors can no longer be applied due to their low reflectivities in normal incidence geometry and potential damage due to the high absorbed powers. Hence, light amplification cannot be reached in a multi-pass setup any more.

In order to deliver light in the ultraviolet and X-ray range an FEL shall operate in a high-gain single pass regime as shown in Figure 2.1.2 b. This requires a linac, where the electron beam with high phase space density passes a long undulator just once. Due to less perturbative effects a much finer beam can be generated. There are two leading FEL concepts: self-amplified spontaneous emission (SASE) and seeding by an external field. In the SASE FEL [2.1.3, 2.1.4], schematically shown in Figure 2.1.2 b, an electron beam with high current density emits spontaneously in the first section of the undulator. This radiation is then amplified in the second section by several orders of magnitude. The consequence, originating from the statistical nature of the starting up the lasing process, is the uncontrollable spiky nature of the output. To avoid this, more sophisticated configurations have been proposed. A few examples to improve to the SASE scheme are regenerative amplification [2.1.5], two-stage SASE-FEL [2.1.6] and pulse compression [2.1.7].

An alternative approach is seeding using the high-gain harmonic generation (HG) concept [2.1.8]. The underlying idea is to overlap the electron bunch with the field of an external seed in the first undulator, called modulator. In the modulator the seed field interacts



with the electron beam introducing a small energy modulation. The energy-modulated electron beam then passes through a dispersive section, e. g. a three-dipole chicane, where the energy modulation is converted into density modulation. The density modulated beam is then sent through the second undulator (radiator) tuned to some harmonic of the seed laser. The up-frequency conversion efficiency for this classic HGHG scheme is relatively low: generation of the  $n^{\text{th}}$  harmonic of the seed laser requires the energy modulation amplitude approximately equal to  $n$  times the slice energy spread of the beam, the energy spread for slices - portions of the bunch associated with the so-called coherence length. Because a considerable increase of the slice energy spread would degrade the lasing process in the radiator, the harmonic numbers  $n$  used in the classic HGHG scheme are typically not larger than 6. In order to generate coherent ultraviolet and X-rays, multiple stages of the conventional HGHG FEL are to be used. At each stage heating occurs, the noise will be amplified as well and the quality of the FEL output radiation degrades. These unwanted effects could be avoided, if the seed is applied directly at shorter wavelengths close to or in the final output range, so that the number of repetitions could be minimized. To produce these short wavelengths high-order harmonic generation (HHG) in gases is a promising tool. If a gas is irradiated by a high intensity laser, some atoms are ionized. Upon recombination, the atoms coherently radiate at odd integer multiples of the fundamental laser frequency.

Recently a new method for generation of higher harmonics using the beam echo effect was proposed (EEHG) [2.1.9]. The echo scheme has remarkable conversion efficiency and allows for generation of high harmonics with a relatively small energy modulation. The echo scheme uses two modulators and two dispersion sections. In general, the frequencies of the first,  $f_1$ , and the second,  $f_2$ , modulators can be different. The beam modulation is observed at the wavelength  $1/k_{\text{echo}}$ , where  $ck_{\text{echo}} = nf_1 + mf_2$ , with  $n$  and  $m$  — integer numbers and  $c$  — a real number. The first dispersion section is chosen to be strong enough, so that the energy and the density modulations induced in the first modulator are macroscopically smeared due to the slippage effect. At the same time, this smearing introduces a complicated fine structure into the phase space of the beam. The echo then occurs as a recoherence effect caused by the mixing of the correlations between the modulation in the second modulator and the structures imprinted onto the phase space by the combined effect of the first modulator and the first dispersion section. The key advantage of the echo scheme is that the amplitude of high harmonics of the echo is a slow decaying function of the harmonic number.

The schematics of the conventional one-stage HGHG and EEHG are illustrated in Figure 2.1.3 [2.1.9].

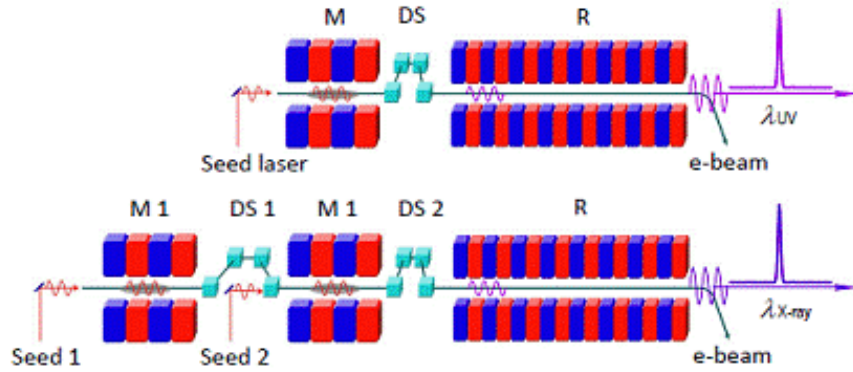


Figure 2.1.3: Top: conventional HGHG scheme, full temporal coherence with a limited harmonic number for a single stage; Bottom: EEHG scheme, full temporal coherence with a potentially very high harmonic number in a single stage. (M – modulator, DS – dispersive section, R – radiator).

## 2.2 European XFEL

The European X-Ray Free-Electron Laser is a new international facility being built in the north west of Hamburg [2.0.10]. The purpose of the facility is to generate extremely brilliant (peak brilliance  $\sim 10^{33}$  photons/s/mm<sup>2</sup>/mrad<sup>2</sup>/0.1% BW), ultra-short (about 100 fs) pulses of spatially coherent X-rays with wavelengths down to 0.1 nm, and to exploit them for scientific experiments in a variety of disciplines spanning physics, chemistry, materials science and biology. The basic process adopted to generate the X-ray pulses is SASE, whereby electron bunches are generated in a high brightness gun, brought to high energy (up to 17.5 GeV) through a superconducting linear accelerator (linac), and conveyed to up to 200 m long undulators, where the X-rays are generated. Five photon beamlines deliver the X-ray pulses to ten experimental stations, where state-of-the-art equipment is available for the experiments.

The layout of the facility is shown in Figure 2.2.1. The basic functions of the main components are schematically described in the following. In the injector, electron bunches are extracted from a solid cathode by a laser beam, accelerated by a radio frequency (RF) electron gun and directed towards the linac with an exit energy of 120 MeV. In the linac, consisting of a 1.6 km long sequence of superconducting accelerating modules, magnets for beam steering and focusing, and diagnostic equipment, the electrons are accelerated to energies of up to 17.5 GeV – the maximal energy foreseen for the standard mode of operation of the E-XFEL facility. The accelerating modules consist of TESLA cavities [2.2.1] shown in Figure 2.2.2, which are standing wave resonators excited by the high power RF of 1.3 GHz. The electron bunch enters each next cell of the cavity at the zero crossing of the field amplitude, thus being accelerated over the whole length of the cavity. A superconducting accelerating module driven at the third harmonic frequency of the TESLA structures, that means 3.9 GHz, is situated behind the first acceleration module close to the photo injector. It is used to linearize the longitudinal phase space distribution in order to improve bunch compression.

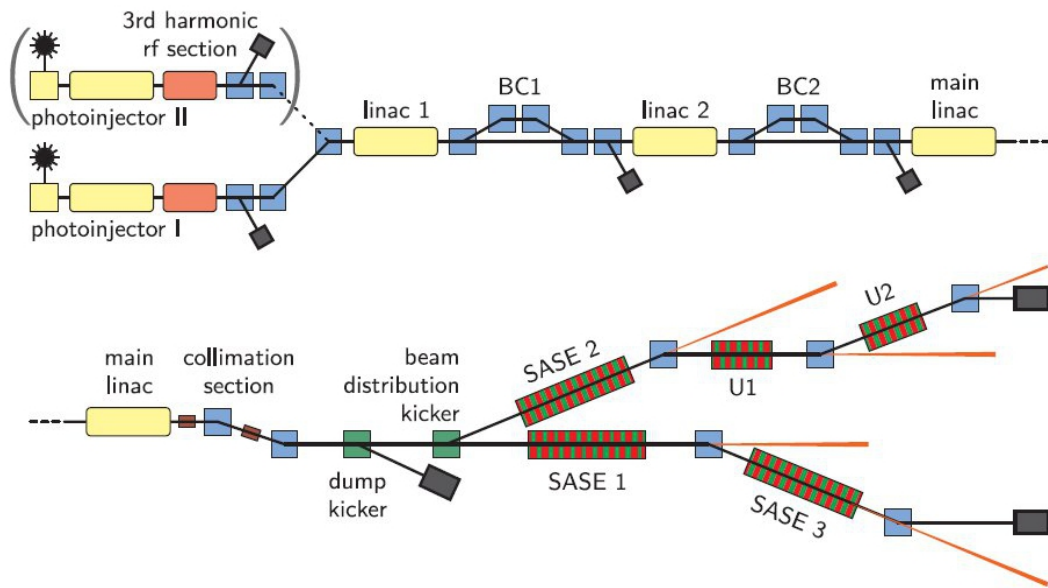


Figure 2.2.1: Layout of the European XFEL.

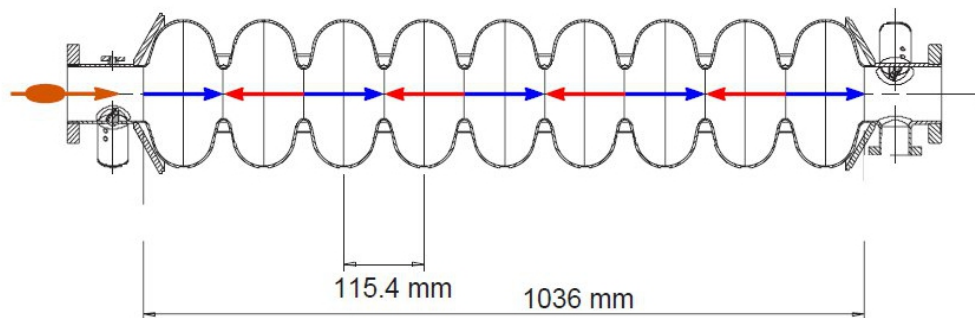


Figure 2.2.2: Side view of the nine-cell TESLA cavity. The amplitude of the electric field has opposite sign for each two neighboring cells.

Along the accelerator, two stages of bunch compression are located, to produce the short and very dense electron bunches required to trigger the SASE process. At the end of the linac, the individual electron bunches are channeled down to one of the two electron beamlines by the beam distribution system. The sections designated as SASE 1-3 are undulator lines long enough to support the SASE FEL process to produce X-ray photons, U 1-2 are comparatively short undulator lines for the generation of spontaneous radiation of very hard X-ray photons (wavelengths down to 0.014 nm and 0.06 nm, respectively). The photons generated by the five undulators are transported through the respective photon beamline to the experimental hall, where they are then fed into ten experimental stations. Reducing the electron energy at the end of the accelerator would generate longer wavelengths, in case they are required by some experiments; for example, electron energy of 10 GeV would correspond to X-rays of 4.9 nm wavelength from the SASE 3 undulator.

Electron beam energy for 0.1 nm wavelength	17.5 GeV
Bunch charge	1 nC
Repetition rate	10 Hz
Pulse rate	4.5 MHz
Maximum number of bunches per pulse at 17.5 GeV	3250
Maximum beam pulse length	650 $\mu$ s
Maximum average beam power	600 kW
Peak current	5 kA

Table 2.2.1: Electron beam parameters of the European XFEL.

There are electron beam dumps downstream the injector, each of the bunch compressors and at the end of all main electron beam lines. This allows for stopping the beam at any of those positions, so the commissioning of the machine or setting it up can be done in steps this way.

## 2.3. FLASH

FLASH is the world's first soft X-ray free-electron laser available to the photon science user community for experiments since 2005. This is a user facility of the SASE FEL beam at DESY [2.3.1] and also a test facility for the European XFEL and the ILC [2.3.2, 2.3.3].

The schematic view of FLASH is presented in Figure 2.3.1. The linear accelerator section of FLASH consists of an electron photoinjector, seven accelerating modules, each of them equipped with eight 1.3 GHz TESLA cavities, a module with four superconducting cavities operated at 3.9 GHz – 3<sup>rd</sup> harmonics cavity, two bunch compressors, a collimation section and numerous diagnostics sections. It has a length of about 200 m and is followed by the undulator section, where a variable-gap undulator for a direct laser seeding experiments (sFLASH) [2.3.4] and long fixed-gap SASE undulators are installed. Behind the undulator section the electron beam is steered to the dump section for proper stop. A dedicated extraction beamline allows sending photon pulses either to a diagnostics branch or to the experimental hall.

FLASH can produce SASE FEL light ranging from the vacuum ultraviolet to the soft X-ray range. In September 2010 FLASH has produced radiation with the fundamental wavelength of 4.12 nm (water window) for the first time. In April 2012 sFLASH has obtained first seeding at 38 nm. In 2014 a major extension of the facility (referred to as FLASH2) [2.3.5] will be commissioned. It includes a new experimental hall and an additional undulator section with a

variable-gap undulator. In addition to the SASE mode used in the first section, the HHG seeding scheme is foreseen for the wavelengths between 10 nm and 40 nm. The electron beam will be switched between FLASH1 and FLASH2. The extension will double the number of user stations thus allowing for more effective use of the facility.

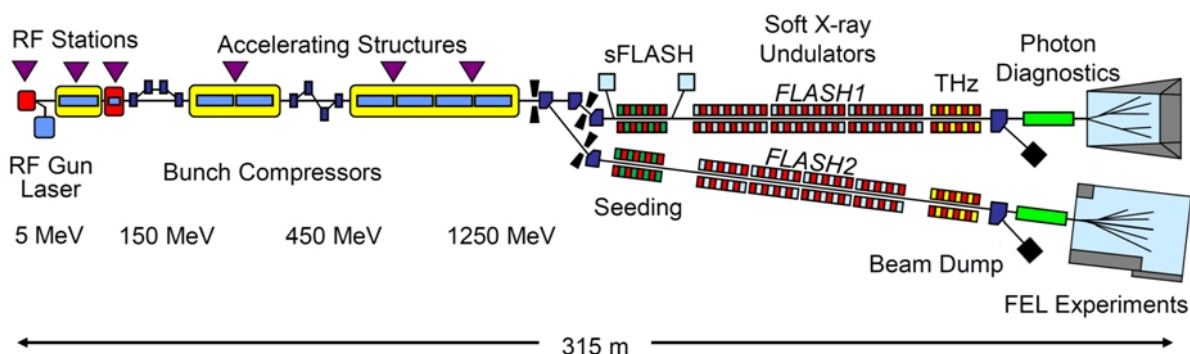


Figure 2.3.1: Layout of FLASH facility in 2014.

The main parameters of the electron beam of FLASH are listed in the Table 2.3.1.

Maximum electron beam energy	1.25 GeV
Maximum bunch charge, nominal (maximum)	1.2 nC (3nC)
Repetition rate	10 Hz
Pulse rate, nominal (maximum)	1 MHz (3 MHz)
Maximum number of bunches per pulse	800 (2400)
Beam pulse length	800 $\mu$ s
Maximum average beam power	300 kW
Peak current	1-2 kA

Table 2.3.1: Electron beam parameters of FLASH. The numbers in parenthesis give maximal values of the parameter.

# Chapter 3

## Beam Diagnostics

Beam diagnostics is essential in the machine operation. It lets us perceive what properties a beam has and how it behaves in the accelerator. It is important in two aspects. Firstly, the beam properties define the successfulness of the scientific use of the machine. Secondly, beam diagnostics has its purpose to prevent the beam from causing any damage or harm during machine operation. In this thesis hereafter electron beams will be considered in the context of beam diagnostics. High-power high-occupancy beams can impose damage to the machine itself and, by activation of the components, to the surroundings. In addition, activation can make maintenance complicated or even impossible. Whenever the beam is going to be stopped, the full power it carries is deposited to the dump. Therefore, special care should be taken in order to make it correctly. This is the main task for the beam dump diagnostics. As an example, the beam dump diagnostics at FLASH is described in this chapter. The major part of the tools mentioned here are common and widely used for such purposes. In contrast, the Beam Halo Monitor [3.0.1] based on synthetic diamonds and sapphires has been first introduced for FLASH.

### 3.1 Unwanted conditions in particle accelerators

In particle accelerators the high-density beam core consisting of particles following the projected trajectory is always surrounded by a low-density region. Sometimes the constituents of the low-density regions are distinguished between those attributed to disruptive beam losses and mild beam loss associated with the formation of a tenuous beam halo [3.1.1]. Nevertheless, from the point of view of beam diagnostics the origin of the low-density regions is not important; therefore the particles from these regions of any origin will be referred to as beam halo in this thesis. The beam core can often be approximated by a Gaussian distribution. The beam halo is then the particles which are outside the region of  $n \cdot \sigma$  from the beam center, where  $\sigma$  is the standard deviation of the particle density distribution and  $n$  is a natural number, typically equal to 3 or 4.

There are numerous sources of the beam halo. The main sources of the beam halo for high-intensity beams can be divided into two categories: disruptive beam losses and mild beam losses.

Physics of violent beam instabilities in high energy linacs and circular accelerators are described in section 3.1.2. Among them are energy spread and beam break-up. As the beam travels along the accelerator, the excited wake field produces a longitudinal retarding force on particles in the beam. The force causes energy changes of individual particles. This affects the total energy loss of individual particles as of the beam transverses impedance associated with the accelerator environment. The acquired energy spread of the particles in the bunch is the reason for each individual particle to follow a slightly different trajectory in the accelerator, being the reason of halo formation. The phenomenon of beam break-up [3.1.3-3.1.5] is observed when the beam is off-centered, e. g. due to its betatron oscillation. For high-intensity bunched beams, a dipole wake field excited by the head of the bunch causes transverse deflection of the bunch tail.

Some of the processes leading to mild beam losses are space-charge resonances [3.1.6, 3.1.7], intra-beam scattering [3.1.8], elastic and inelastic rest gas scatterings [3.1.9, 3.1.10] and RF noise of the injector [3.1.11].

Space-charge resonances include intrinsic incoherent resonances and space-charge coupling resonances. A class of resonances where individual particles inside the beam get into a resonance with an oscillating beam mode are referred to as intrinsic incoherent resonances. The space-charge coupling resonances are driven by the space charge potential itself rather than field potential of magnets. Space-charge structure resonances are collective modes of beam oscillation resonating with the lattice structure. These resonances lead to substantial emittance growth. Multiple Coulomb scattering or intra-beam scattering of particles in a bunched beam by others in the same bunch can lead to continuous growth of the energy spread and/or one or both transverse emittances. Elastic and inelastic scattering of the particles in the beam on the molecules of the residual gas in the beam pipe. In the elastic process of Mott scattering, the incident beam particle is deflected by the Coulomb potential of the particles in the residual gas. Elastic scattering changes the direction of the particle while its energy is not affected. Elastic scattering can lead to large betatron amplitudes and loss of particles at collimators or any other aperture restriction. At high energies inelastic scattering of the particles from the nucleus of the residual gas happens in the form of Bremsstrahlung. In the case of inelastic scattering both the direction and the energy of the beam particle. RF noise in the injector is due to the so-called coalescing process where high intensity bunches are generated by merging several smaller bunches. Coalescing typically leaves a certain amount of the beam particles outside RF buckets. These particles are transferred together with the main bunches.

Beam halo can be both transverse and longitudinal. Transverse halo is more relevant for the beam diagnostics and will be considered later on in the thesis.

Figure 3.1.1 shows the transverse beam profile at FLASH. The beam core and beam halo can be clearly distinguished.

In contrast to the halo accompanying the beam, the accelerator dark current appears in high field gradient structures in presence of radiofrequency pulse and can travel along the machine. Depending on the location of the emitters, the particles of the dark current can travel with the beam core or follow completely different trajectories.

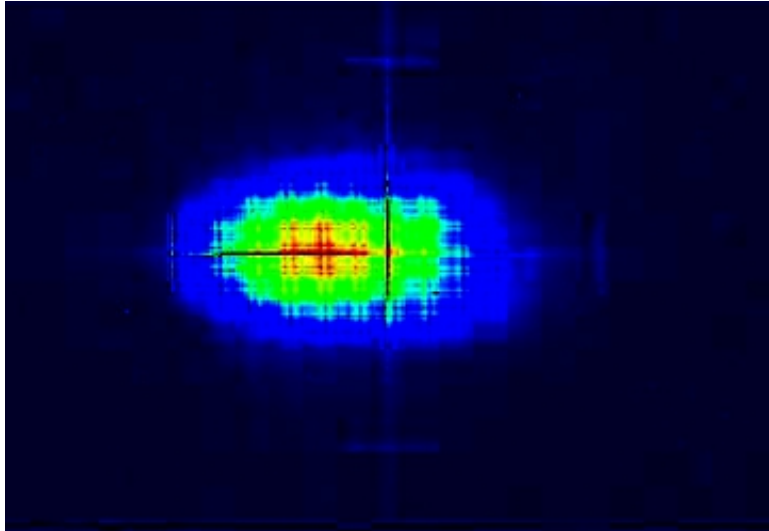


Figure 3.1.1: Transverse beam profile at FLASH. The beam core (green, yellow and red) is surrounded by halo (light blue).

In the dump area dangerous conditions can be the result of any of the the following reasons: strongly off-centered beam, high-intensity transverse beam halo and high dark current. The standard beam dump diagnostics components comprise tools for transverse beam profile, beam position, bunch charge and beam losses measurements. The next section of this chapter will be dedicated to their description. The aspects of interaction of the particles associated with the beam losses with matter will be considered in chapter 4.

## 3.2 Standard beam diagnostics

The diagnostics systems described below belong to well established types of diagnostics, and are not specific tools for the dump region.

### 3.2.1 Beam profile measurements

Luminescent screens and the screens that employ optical transition radiation (OTR) are widely used for beam profile measurements. The OTR screens are common tools for high energy electron beams, while luminescent screens are suitable for hadron and low energy electron beams, where the intensity of OTR is rather low. The experience gained at the modern linac-based light sources shows that the use of the OTR screens can be compromised even for



high energy electron beams due to coherent effects in the emission of the OTR (COTR) [3.2.1.1]. If the electron beam has full transverse coherence at visible wavelengths and the beam size is comparatively large, the OTR image of the beam will not show the beam distribution, but the absolute square of the gradient of the transverse beam shape. Therefore, one of the alternative options for those high energy electron machines is the use of luminescent screens, especially with inorganic scintillators. Let us consider these 2 types of the screens in some more details.

Transition radiation (TR) is emitted when a relativistic charged particle crosses the boundary between two media with different dielectric constants. The TR is radiated in the forward direction along the incidence and in the backward direction around the specular reflection of the incident beam. The case of the so-called oblique incidence is sketched in Figure 3.2.1.1. Such incidence angle of  $45^\circ$  allows for separation of the electron beam and the emitted light.

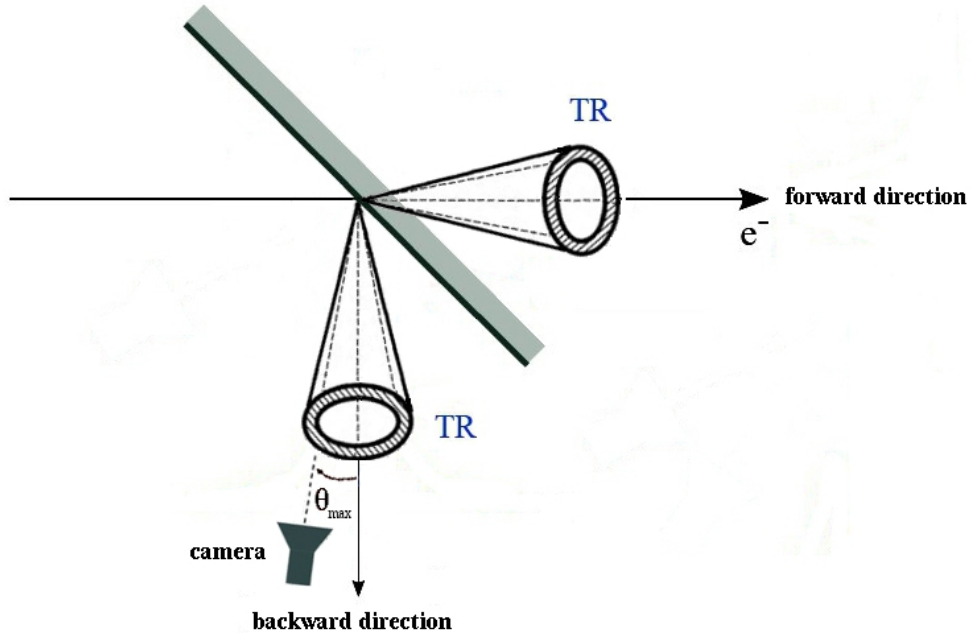


Figure 3.2.1.1: TR and its emission in the forward and reflected cone in case of oblique incidence.  $\theta_{max}$  gives the angle of the maximum intensity with respect to the axis of forward and reflected emission.

The spectral and spatial radiation energy from a single electron is given by the Ginzburg-Frank formula [3.2.1.2] valid for the far-field region and for the effective source size:

$$\frac{d^2U}{d\omega d\Omega} = \frac{e^2}{4\pi^3 \epsilon_0 c} \cdot \frac{\beta^2 \sin^2 \theta}{(1 - \beta^2 \cos^2 \theta)^2}, \quad (3.2.1.1)$$

where  $\beta=v/c$  with  $v$  being the velocity of the electron and  $\theta$  – the angle with respect to the specified directions of radiation. The angular distribution of the TR radiation is shown in Figure 3.2.1.2. The intensity has its maximum at the angle:

$$\theta_{\max} = \arcsin\left(\frac{\sqrt{1-\beta^2}}{\beta}\right) = \arcsin\left(\frac{1}{\beta\gamma}\right) \cong \frac{1}{\gamma}, \text{ for } \gamma \gg 1. \quad (3.2.1.2)$$

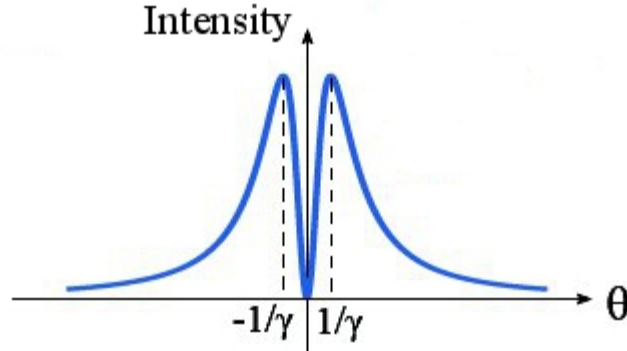


Figure 3.2.1.2: Angular distribution of the TR radiation.

OTR can be easily detected using a CCD camera positioned at the angle  $\theta_{\max}$ . In case of incoherent radiation, the resultant OTR image represents the convolution of the real transverse beam distribution with the image of a single electron. The OTR in the backward direction is usually used since it is separated from the electron beam. Aluminum coated silicon wafers have high radiation yield in the backward direction and good survival to thermal heating and are often used as a material for the OTR screens.

Microbunching instabilities inside the compressed bunch [3.2.1.3] are suggested to be the cause of the coherent effects in the OTR that make the radiation image to be no longer a true representation of the transverse charge distribution. If they create structures with a size of the order of the observed wavelength, the beam starts to emit TR coherently. In order to mitigate the COTR the attempts were made to apply the idea of spectral separation based on beam imaging in the wavelength range where the coherence effects are suppressed [3.2.1.4]. An alternative way is to use incoherent radiation from luminescent screen.

Luminescent screen utilize the ability of materials to emit light in response to energy lost by the beam particles passing through it and deposited in excited atomic states in the medium. The light is emitted in the radiative transitions of atomic electrons from the excited to the ground state, therefore the spectra are always discrete. Although various types of luminescence in principle can be used, inorganic scintillator is often a good choice for this type of screens [3.2.1.5, 3.2.1.6]. The properties of inorganic scintillators are a good match to the most important requirements for a good scintillator for such purpose. These are:

- 1) high efficiency in energy conversion into light,

- 2) emission spectra matched to the spectral response of the photon detector,
- 3) high dynamic range and good linearity between the incident particle flux and the light output,
- 4) no absorption of emitted light inside the bulk material,
- 5) fast decay time for observations of time dependent beam size variations and reduction of saturation effects,
- 6) good mechanical and thermal properties, high radiation hardness to prevent damages.

The light from the luminescent screen can be detected with a CCD camera. The electron beam crossing a luminescent screen does not only create scintillator light, the OTR radiation is also present. Detection of the OTR is suppressed using the principles of temporal and spatial separation. The pulse of the OTR radiation created by a bunch of electrons is typically shorter than that of the scintillator light. The gate of the CCD camera opens after the short OTR pulse. The principle of the spatial separation is illustrated in Figure 3.2.1.3. While the intensity of the TR has a strong angular dependence, the scintillation light is emitted isotropically. Positioning the camera at an angle much larger than  $\theta_{\max}$  allows the detection of incoherent scintillation light, while the intensity of the OTR at this angle is negligible.

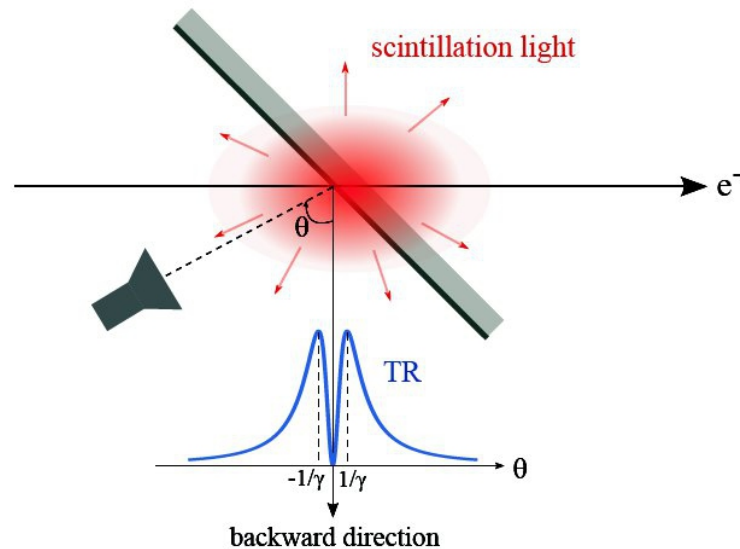


Figure 3.2.1.3: Principle of light detection from a luminescent screen. The scintillation light is separated from the OTR by positioning the camera at an angle much larger than  $\theta_{\max}$  or/and gating the camera after the short OTR pulse.

In the description above, the transverse beam profile measurement was considered. The longitudinal beam profile can also be measured with the OTR and luminescent screens in combination with a transverse deflecting structure (TDS) [3.2.1.7]. TDS is an RF transverse deflecting cavity operating at the same frequency as the main linac. It sweeps the beam transverse to the direction of propagation thus giving a strong correlation between longitudinal

coordinate and transverse position. The longitudinal charge distribution of the electron bunch is thus transformed into transverse distribution. The measurements are performed in the same way as described for the transverse beam profile.

### 3.2.2 Beam position measurements

There are many types of devices for determining the transverse beam position, referred to as beam position monitors (BPM). These devices are normally non-destructive and differ by the operating principle of the transducer, such as capacitive, inductive, travelling wave and resonant structure. Below the three most common types of BPM are shortly introduced.

Button BPM is an example of a BPM with capacitive transducer. It consists of two or more pairs of opposing electrodes. The circular arrangement of a rotated button BPMs is shown in Figure 3.2.2.1. The image current induced on an electrode by a passing bunch induces a voltage across the impedance between the electrode and the pipe. The beam position in the horizontal plane can be derived from a linear combination of all four button signals as:

$$x = S_x \cdot \frac{(U_1 + U_4) - (U_2 + U_3)}{U_1 + U_2 + U_3 + U_4} + \delta_x \dots\dots(3.2.2.1)$$

Similarly, the beam position in the vertical plane can be derived as:

$$y = S_y \cdot \frac{(U_1 + U_2) - (U_3 + U_4)}{U_1 + U_2 + U_3 + U_4} + \delta_y \dots\dots(3.2.2.2)$$

Here  $S_x$  and  $S_y$  are the sensitivity in vertical and horizontal planes determined from calibration,  $\delta_x$  and  $\delta_y$  are offset corrections arising from deviation of the center of the bunch charge and geometrical center.

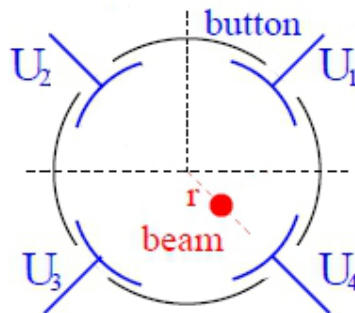


Figure 3.2.2.1: Sketch of the cross sectional view of a typical circular arrangement of a rotated button BPM. The beam position with an offset  $r(x, y)$  is shown.

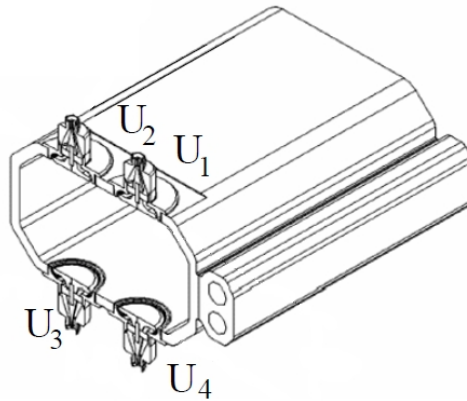


Figure 3.2.2.2: Typical planar button BPM arrangement.

If the beam pipe does not have a circular shape due to different emittances in horizontal and vertical directions, e. g. in synchrotron light sources, a planar BPM arrangement is required. A typical beam pipe shape and orientation of the BPMs is depicted in Figure 3.2.2.2. The beam position is determined using the equations 3.2.2.1 and 3.2.2.2.

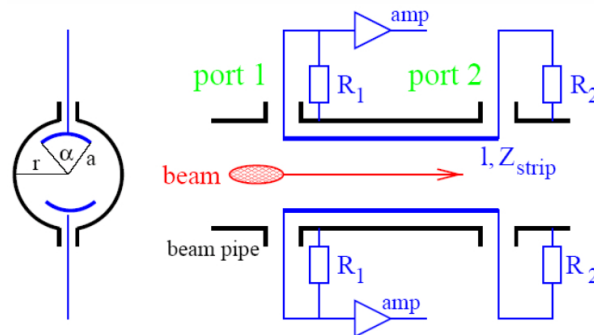


Figure 3.2.2.3: Schematic view of a stripline BPM in transverse (left) and longitudinal (right) planes.

Stripline BPM operates on the principle of a traveling wave [3.2.2.2]. The scheme of a stripline BPM with two pick-ups is shown in Figure 3.2.2.3. When a bunch of relativistic charged particles passes the striplines of the length  $l$  and the characteristic impedance  $Z$ , it induces an electromagnetic pulse. Half of the induced pulse generates a voltage across the resistance  $R_1$  at the port 1 of the stripline, while the other half of the induced pulse travels along the stripline. On arrival at the port 2, the half of the traveling pulse gets reflected and returns to port 1, while the other half generates a voltage across a resistance  $R_2$ . At any time  $t$  the induced voltage at the port 1 can be calculated as:

$$U(t) = \frac{1}{2} \cdot \frac{\alpha}{2\pi} \cdot R_1 \left( I_b(t) - I_b\left(t - \frac{2l}{c}\right) \right), \quad (3.2.2.2)$$

where  $I_b$  is the beam image current,  $\alpha$  is the angular dimension of the stripline and  $c$  is the speed of light. The signal appears as two pulses out of phase with the time difference of  $2l/c$ .

In case of the stripline BPM with four strips the beam position can be calculated in the same way as for button BPM.

A cavity BPM is essentially a form of waveguide [3.2.2.3]. The electric and magnetic fields at any position inside the cavity are always orthogonal to each other. The values of the electromagnetic (EM) field components can be calculated by solving Maxwell equations and applying appropriate boundary conditions at the walls. These conditions limit the EM field to oscillate with specific field distribution patterns, known as the resonant modes of the cavity. Based on the direction of the EM field components, the resonant modes can be classified in either a transverse electric (TE) type mode, with its electric field perpendicular to the cylindrical axis of the cavity, or a transverse magnetic (TM) type mode, with its electric field aligned parallel to the cavity axis. When a bunch of high energy charged particles passes through a resonant cavity, some of its energy gets coupled in the cavity and induces oscillating EM fields over the different resonant modes. The electric of the two primary TM modes are of interest: the first monopole  $TM_{010}$  and dipole  $TM_{110}$  modes. The amplitude of the induced dipole mode is proportional to the charge and position offset of the bunch from the center of the cavity, hence it can be used to measure the beam position. However, for a small position offset, the amplitude of the induced monopole mode does not depend on the bunch position, but it is sensitive to the bunch charge. It can be used to provide reference measurements for the bunch charge and bunch arrival time.

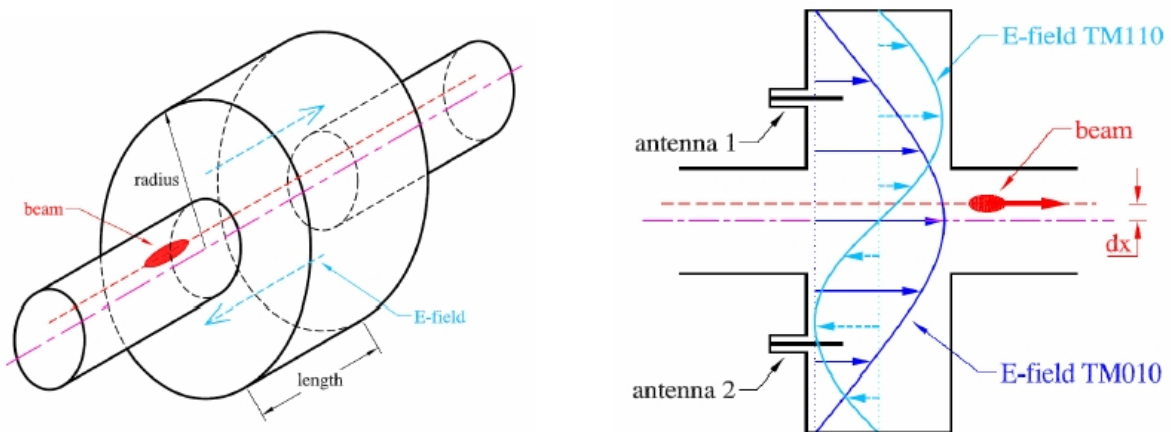


Figure 3.2.2.4: View to a simple cylindrical cavity geometry. Left: 3-dimensional view. Right: a simplified cross section in the beam direction.  $dx$  is the vertical beam offset. Two antennas serve for signal pick-up.

### 3.2.3 Bunch charge measurements

From the early days of the accelerators Faraday cups have been used for direct measurements of the beam charge. Such measurements are interceptive and are not applicable

for high current beams. For the latter current transformers are utilized to determine the beam charge.

For beams with no time-dependent structure the so-called direct-current transformers are used. In accelerators with multiple closely spaced bunches the integrating current transformers are often applied in order to measure the charge of a single bunch. Let us consider the latter in some more details.

The beam passing through a highly permeable torus acts as primary winding. An insulated wire, wound around the torus with  $N$  turns, serves as secondary winding. For an ideal current transformer the ratio between the primary and the secondary currents is given by the ratio of the turns in the primary and secondary windings. The voltage signal over time for a current transformer loaded to the resistance  $R$  is

$$U(t) = R \cdot I_{\text{sec}}(t) = \frac{R}{N} \cdot I_{\text{beam}} \cdot e^{-\left(\frac{R}{L}\right)t}, \quad (3.2.3.1)$$

where  $N$  is the number of turns in the secondary winding,  $I_{\text{sec}}$  is the secondary current,  $I_{\text{beam}}$  is the primary beam current, and  $L$  is the inductance. The latter is given by the following expression:

$$L = \frac{N^2 \mu_r \mu_0 A}{l}, \quad (3.2.3.2)$$

with  $\mu_r$  and  $\mu_0$  being the magnetic permeability of the medium and of free the vacuum respectively,  $A$  – the cross sectional area of the magnetic ring, and  $l$  – the circumference of the toroid.

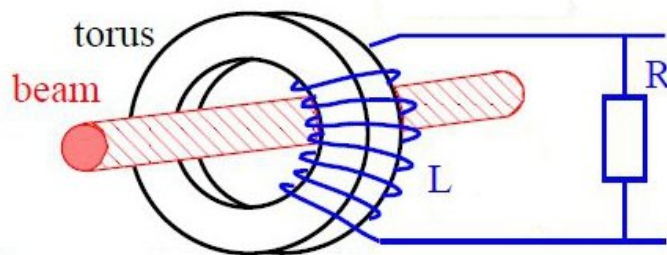


Figure 3.2.3.1: Schematic view of toroid system.

Beam current transformers for pulsed linacs approach a resolution of  $10^6$  electrons per pulse. The transformers for circulating beams can reach a resolution of 10 nA.

### 3.2.4. Beam loss monitoring

The task of beam loss monitors (BLMs) is to localize losses taking place at a certain location during a certain time interval. In general, they detect mostly secondary particles produced in collisions of the high energy particles in the beam with the residual gas, beam pipe or any material in the vicinity. Their signals should be proportional to the amount of the loss. Depending on application, BLMs can be localized or distributed systems. Fast systems with nanosecond time resolution allow detecting losses on a bunch-by-bunch basis. Slow system resolve time intervals of hundreds of milliseconds. Various technologies are used: short and long ionization chambers, PIN diodes, secondary emission monitors (SEM), scintillator and Cherenkov counters.

#### 3.2.4.1 Ionization chambers

Ionization chambers are one of the most common BLMs. In its simplest form an ionization chamber consists of a pair of electrodes, anode and cathode, separated by a gap filled with a gas like air, argon, xenon or a liquid. In this section the focus is on this type of ionization chambers. There are also solid state ionization chambers. They will be described in more detail in chapter 4.

The gap between the electrodes defines the sensitive volume of the chamber. Ionizing particles traversing the sensitive volume create pairs of an electron and a positive ion. High voltage applied between the two electrodes creates an electric field that forces the electrons and positive ions to separate and to drift to the corresponding electrode. The number of charge carriers reaching the electrode may depend on the applied voltage. Ionization chamber usually operates in the regime, where the signal does not change with the applied voltage and is proportional to the energy deposited in the sensitive volume as it is shown in Figure 3.2.4.1.1 [3.2.4.1.1]. The response time of an ionization chamber is defined by the transit time  $t$  of the charge carriers through the gap  $D$  between the electrodes:

$$t_i = D/v_i, \quad (3.2.4.1.1)$$

where  $v_i$  is the drift velocity of a charge carrier with  $i$  denoting either electrons or positive ions. The drift velocity can be fairly accurately predicted from the relation:

$$v_i = \frac{\mu_i \cdot E_{e.f.}}{P} = \frac{\mu_i \cdot V}{P \cdot D}, \quad (3.2.4.1.2)$$

with  $E_{e.f.}$  being the electric field strength,  $\mu_i$  – the mobility of charge carriers,  $V$  – the voltage applied between the electrodes,  $P$  – the pressure in units of normal atmospheric pressure and  $D$  – the gap between the electrodes.

The number of electron-ion pairs produced in the gap  $D$  of the ionization chamber is:



$$n = \frac{D \cdot \rho}{W} \cdot \frac{dE}{dx}, \quad (3.2.4.1.3)$$

with  $dE/dx$  being energy deposition in the medium,  $\rho$  – its mass density and  $W$  – the energy to create one electron-ion pair [3.2.4.1.2]. The process of energy loss by electrons in media is considered in some more detail in chapter 4.

The signal from an ionization chamber is a superposition of the drift of both types of charge carriers. The electron mobility in gases and liquids is typically much higher than that of positive ions. Therefore, in the applications either the electron current only is collected or attempts are made to shorten the charge collection for positive ions by e.g. making the gap between electrodes smaller.

The dynamic range of an ionization chamber should be wide to be able to detect small losses and remain in operation even in case of large losses. The lower limit is given by the leakage current between the electrodes. The upper limit is reached when the response becomes non-linear due to recombination process at high ionization densities.

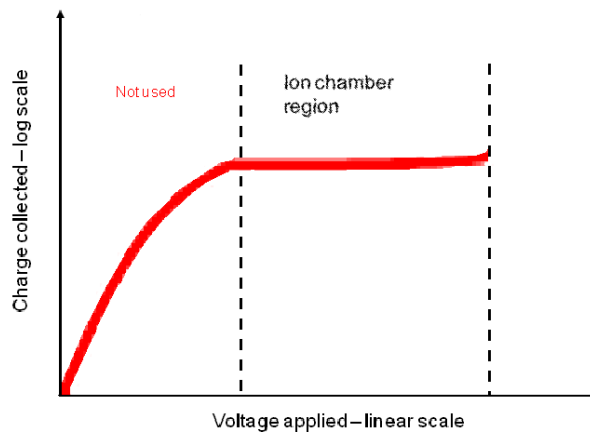


Figure 3.2.4.1.1: Dependence of the collected charge on the voltage applied for an ionization chamber at a constant ionization rate.

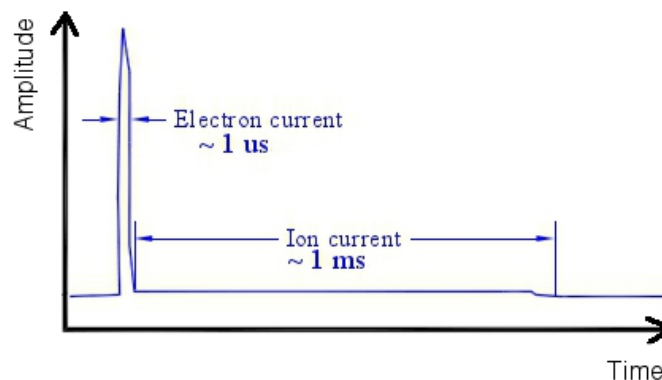


Figure 3.2.4.1.2: Typical signal from an ionization chamber.

There are short and long ionization chambers. Short ionization chambers allow for position measurement. In order to achieve good coverage at accelerators a large number of the chambers need to be installed. To overcome the problem long ionization chambers, consisting of long coaxial cable filled with air or other gases, are used. The position sensitivity can be improved either by reading out both the direct signal and the signal reflected at the rear end of the chamber or by segmentation of long ionization chambers and reading out each segment separately.

### 3.2.4.2 PIN diodes

The required energy to create an electron-hole pair in a semiconductor is much smaller than that to create an electron-ion pair in gas. In addition, the density of a semiconductor is a few orders of magnitude larger than the one for a gas under normal pressure. Therefore semiconductor is an interesting material for ionization chambers – the so-called solid state ionization chambers. Semiconductor diodes with p-n junction are one of the most widely used devices of this type. There is another device of such kind suitable for radiation detection – the PIN diode.

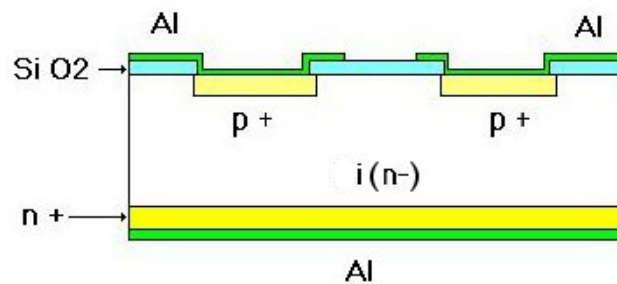


Figure 3.2.4.2.1: Basic structure of a PIN diode. Al – aluminium contact, p+, i(n-) and n+ are respectively highly doped “p” region, near intrinsic (lightly doped “n”) region and highly doped “n” region.

The PIN diode is a diode with a wide, lightly n-doped semiconductor region (near intrinsic, “i” region) between a p- and an n-type regions as shown in Figure 3.2.4.2.1. It operates under what is known high-level injection: the intrinsic region is flooded with charge carriers created by the energy deposited by incident particles from the “p” and “n” regions. The region where the mobile charge carriers have been forced away by an electric field (space charge region) of PIN diode is larger than that of a conventional diode and is almost completely in the “i” region. Its size has no strong dependence on bias voltage. There are two modes of operation of PIN diodes: photovoltaic mode without bias voltage and conventional photoconductive mode with reverse bias. It should be taken into account that in the photovoltaic mode the signal width can vary with the dose rate. In the photoconductive mode there is no such dependence.

PIN diodes are a good alternative to short gas- or liquid-filled ionization chambers. They can be operated in moderate magnetic fields with no influence on the charge collection. However, like other semiconductor devices, they are subject to radiation damage if the dose exceeds  $10^4$  Gy [3.2.4.2.1].

In addition PIN diodes can be used as particle counters. Two face-to-face mounted devices operate in coincidence in order to count charged particles only and suppress background.

### 3.2.4.3 Secondary emission monitors (SEMs)

A SEM consists of few metal layers surrounded by positive grids placed inside vacuum chamber as sketched in Figure 3.2.4.3.1. The grids are needed to avoid repulsion of the emitted electrons. Incident charged particles release electrons from the surface of metal foil. Most of these secondary electrons have energies of less than a few tens of eV, although a small fraction of elastically and inelastically scattered primary electrons of higher energies is also present. Secondary electron emission is a rather linear process [3.2.4.3.1, 3.2.4.3.2] over a wide range of intensities. The characteristic time of the signal is of the order of nanoseconds and efficiency is about a few per cent. Therefore, SEM is a simple, fast, robust and cheap BLM capable to operate in high radiation fields.

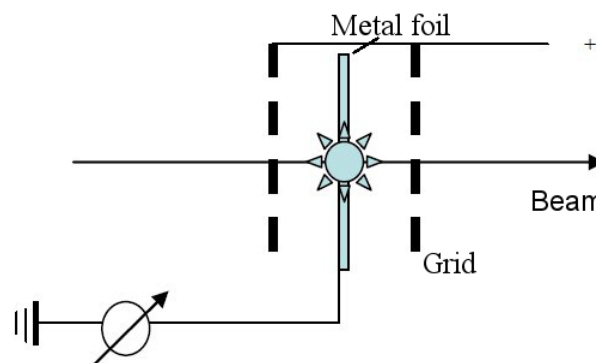


Figure 3.2.4.3.1: A sketch of a SEM.

At low intensities aluminium cathode electron multipliers (ACEM) [3.2.4.3.3, 3.2.4.3.4, 3.2.4.3.5] are employed, where an aluminium cathode instead of the photocathode is used. The working principle is the same as the one of a photomultiplier. Amplification of up to  $10^6$  is possible.

### 3.2.4.4 Scintillator BLM

Scintillator BLM consists of a scintillator block optically coupled to a photomultiplier tube (PMT) [3.2.4.4.1, 3.2.4.4.2]. The scintillation process is the fluorescence – the prompt emission of visible light from the material following its excitation by radiation of various types. A small

fraction of the kinetic energy lost by a charged particle in a scintillator is converted into fluorescent energy. The remaining part is dissipated nonradiatively, primary in the form of lattice vibrations or heat. There are two categories of scintillators: inorganic and organic. Noble gases, nitrogen and inorganic crystals belong to inorganic scintillators. Organic scintillators are plastics, organic liquid solutions and organic crystals

In gaseous scintillators the atoms are individually excited and returned to the ground states, so their response is within about 1 ns. They may or may not contain impurities, the so-called activation centers. Activation centers create energy states within the band gap through which the electron can de-excite back to the valence band. These energy states prevent the photons from re-absorption and thus enhance the light yield. Inorganic crystals used as scintillators contain activation centers. The scintillation mechanism depends on the energy states determined by the crystal lattice. There are two time components in their signal: within a few ns for fast recombination from activation centers and in the interval of  $\mu\text{s}$  to ms for the delayed recombination due to trapping.

The fluorescence process in organics arises from transitions in the energy level structure of a single molecule and therefore can be observed from a given molecular species independent of its aggregate state. The photons are emitted in general in spin-allowed radiative transition between the states with the same multiplicity. The light emitted by the scintillator is absorbed and then re-emitted by the activator centers. There are fast and slow components of the scintillation light. The fast component has characteristic time of a few to several ns, The slow component is due to delayed fluorescence. Its characteristic time is up to ms.

### 3.2.4.5 Cherenkov BLMs

Cherenkov light is emitted when the speed of a charged particle traversing a dielectric medium is larger than the speed of light in the medium. The photons are emitted at an angle  $\theta$  with respect to the trajectory of the particle defined by the velocity of the particle  $\beta$  and refraction index  $n$ :

$$\cos \theta = \frac{1}{\beta \cdot n}. \quad (3.2.4.5.1)$$

The light is focused by a mirror to a PMT for detection as shown in Figure 3.2.4.5.1 [3.2.4.5.1].

Cherenkov BLMs provide fast signals with rise time of a few nanoseconds and can be radiation hard up to 1 MGy, e. g. the ones with radiators made of synthetic fused silica [3.2.4.5.2]. Cherenkov BLMs are almost insensitive to X-rays. The sensitivity of Cherenkov BLM depends on the particle velocity, the refraction index of the media and the path length in the material.

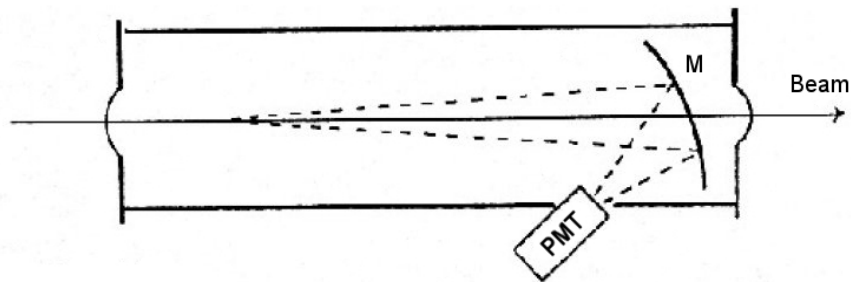


Figure 3.2.4.5.1: Sketch of a typical Cherenkov BLM. M – the mirror that focuses the light to the PMT.

### 3.3. Beam halo monitors (BHMs)

Beam halo monitors are diagnostics systems purposed to observe and characterize the beam halo. The goal is the minimization of beam losses to maximize performance and reduce activation of accelerator components and avoid their damage.

BHM is functionally close to BLM and so-called beam condition monitor (BCM). There are no exact criteria to distinguish them. BHM and BCM can use for the sensors the materials typical for the BLM, like plastic scintillators [3.3.1], or use other materials which are not common for BLM, like CVD diamond [3.3.2]. Although, since a few years CVD diamond sensors are used for BLMs [3.3.3]. BCMs are typically systems inside large detectors in particle colliders. They are purposed to monitor the particle flux outside the beam pipe and can also provide additional useful information, e. g. fast luminosity measurements [3.3.4]. The primary goal of the BLM is measurement of beam losses and machine protection. The task of BHMs is to measure the beam halo or to utilize the halo measurements for beam diagnostics purposes.

In this thesis, the BHM systems for FLASH and the European XFEL using pCVD diamonds and synthetic sapphires as sensors are described.

# Chapter 4

## Radiation Hard Sensors

For decades silicon sensors have been in use to detect radiation. For the application where radiation hardness is essential, a new radiation tolerant material can be an alternative to silicon sensors. Although there are silicon sensors able to withstand high radiation fields, they reveal high leakage currents rising with the dose at room temperatures. Cooling of such sensors is required and can impose technical difficulties to the systems based on these sensors. Therefore, sensors able to operate in high radiation fields at room temperature were required.

Synthetic diamond is an interesting material. Its radiation hardness has been investigated intensively. Outstanding radiation hardness compared to silicon was observed for hadrons, photons [4.0.1] and electrons [4.0.2]. Synthetic sapphire was used as a promising material for the first time.

The focus of this chapter is on radiation hard sensors. Firstly, the working principle of the sensors is explained. Then the mechanism of signal generation is described. Some relevant properties of synthetic diamond are given. The results of radiation hardness measurements with electrons are shown. The properties of synthetic sapphire are discussed. For the first time the results of for sapphire sensor as detector for radiation as well as the results of radiation hardness studies are described in the chapter.

### **4.1 Working principle of solid state sensors**

Solid state sensors operate as ionization chambers. They consist of crystalline materials, where the outer shell electrons energy levels form a band structure. Depending on the size of the energy gap – the forbidden energy zone between the valence band and the conduction band – such materials can be insulators, semiconductors or conductors. Figure 4.1.1 illustrates the band structure of insulators and semiconductors in comparison to conductors. In case of narrow-gap semiconductors a p-n junction must be formed in order to obtain a low intrinsic carrier density. In contrast, wide-gap insulators, like diamond and sapphire, can operate without a p-n junction.

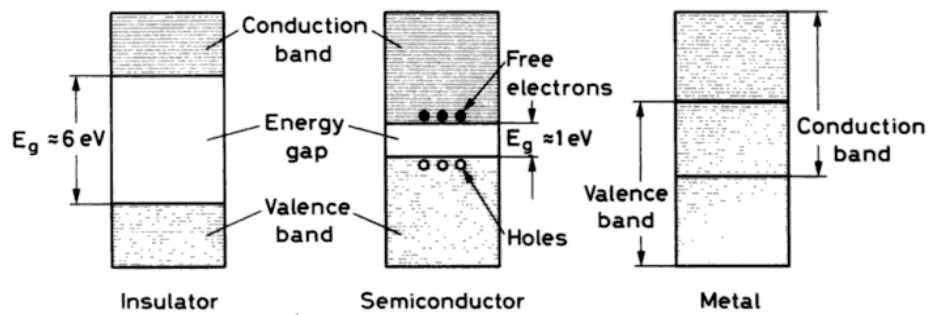


Figure 4.1.1: Energy band structure of insulators and semiconductors in comparison to conductors [3.2.4.4.1].

The working principle of a solid state sensor is illustrated in Figure 4.1.2. The sensitive volume – the volume of the sensor characterized by a low intrinsic carrier density – is defined by the depleted region in a reversed biased diode in case of semiconductors or given by the geometry of contacts on both sides of the sensor plate made of insulator.

An incident charged particle ionizes the material of the sensor along its trajectory. The produced charge carriers separate and start drifting toward the corresponding electrodes in an electric field created by a potential difference between the electrodes. The change of charge distribution induces mirror charge on the electrodes according to Ramo-Shockley theorem [4.1.1, 4.1.2]. This charge is compensated by the current in the external circuit to balance the potential difference.

The amount of charge created by an ionizing particle is given by the energy deposition in the material and the energy needed to create an electron-hole pair. The mechanisms of energy loss by charged particles in matter and the aspects of energy deposition in the sensitive volume of a sensor are explained in the following section.

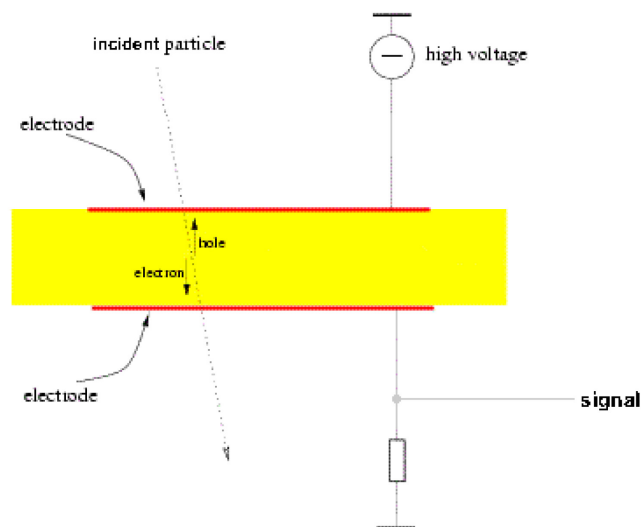


Figure 4.1.2: Sketch of the working principle of a solid state sensor.

## 4.2 Interaction of charged particles with matter

Charged particles moving through matter undergo the following processes:

- 1) inelastic collisions with the atomic electrons of the material
- 2) elastic scattering off nuclei
- 3) Bremsstrahlung and direct pair production in the Coulomb field of the nuclei
- 4) transition radiation
- 5) Cherenkov radiation
- 6) nuclear reactions.

These processes lead to a loss of energy by the particle or a deflection of the particle from its incident direction.

In inelastic collisions with atomic electrons energy is transferred from the particle to the electron. These atomic collisions are divided into soft collisions leading to excitation, and hard collisions in which the energy transferred is sufficient to release the electron from the atom, i. e. cause ionization.

Elastic scattering off nuclei results in mainly the change of the direction of the particle.

The energy losses due to Bremsstrahlung and direct pair production are important at high energy and grow linearly with increasing energy.

Transition radiation and Cherenkov radiation have been already discussed in the chapter 3. Their contribution to the total energy loss is rather small.

Figure 4.2.1 shows as an example the total energy loss of a positive muon transversing copper [4.2.1].

For very low energies the unified approach to the stopping and range theory for heavy ions was made by Lindhard, Scharff and Schiott [4.2.2]. Experimental stopping power data for many elements are summarized by Anderson and Ziegler [4.2.3]. The data is used to describe the stopping power (energy loss) at low energies in Fig. 4.2.1.

The energy loss due to ionization dominates at intermediate energies labeled “Bethe” in Fig. 4.2.1. The expression which gives quite accurate results for the total energy loss by ionization reads:

$$-\frac{dE}{dx} = 2\pi \cdot N_A \cdot r_e^2 \cdot m_e \cdot c^2 \cdot \rho \cdot \frac{Z}{A} \cdot \frac{z^2}{\beta^2} \cdot L(\beta), \quad (4.2.1)$$

where  $r_e$  is the classical electron radius,  $m_e$  – the electron mass,  $N_A$  – Avogadro’s number,  $I$  – the mean excitation potential,  $Z$  – the atomic number of the absorbing material,  $A$  – the atomic weight of the absorbing material,  $\rho$  – the mass density of absorbing material,  $z$  – the charge of the incident particle in units of electron charge and  $\beta=v/c$  – the velocity of the incident particle. The parameter  $L(\beta)$  can be expressed in the following form:



$$L(\beta) = L_0(\beta) + \sum_i \Delta L_i, \quad (4.2.2)$$

$$\text{where } L_0(\beta) = \ln\left(\frac{2m_e \cdot \gamma^2 \cdot v^2 \cdot T_{\max}}{I^2}\right) - 2\beta^2. \quad (4.2.3)$$

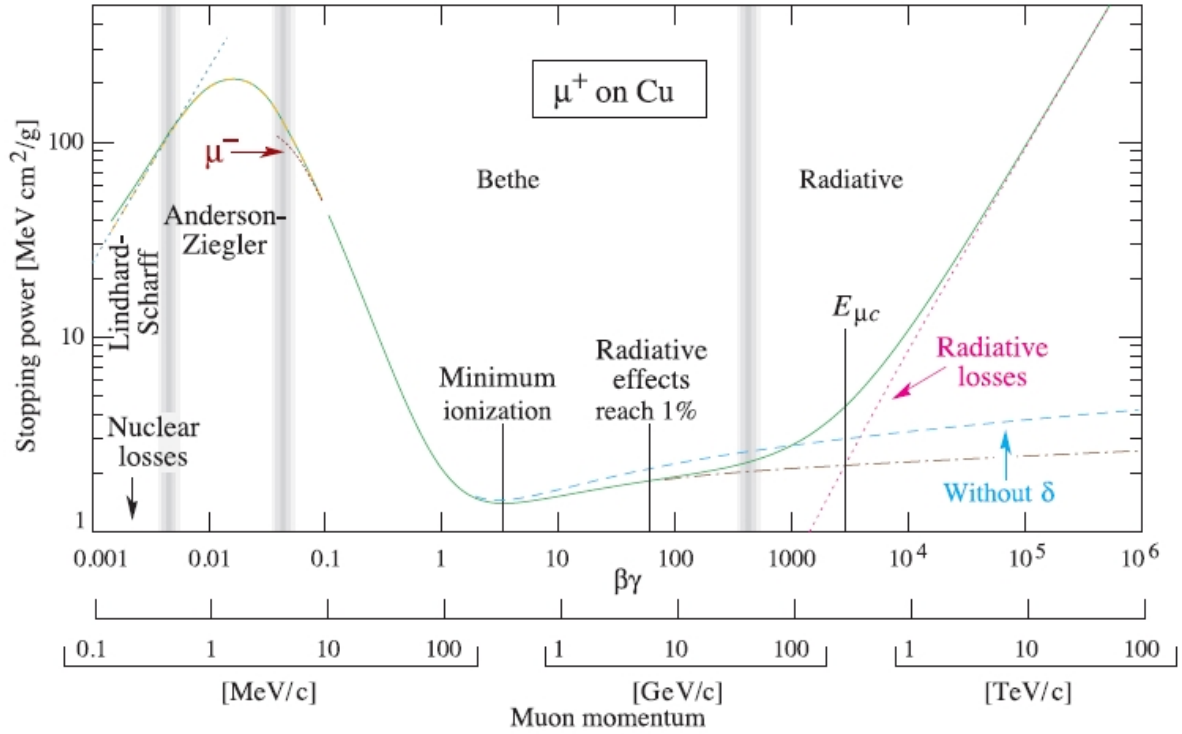


Figure 4.2.1: Total stopping power or total energy loss as a function of the momentum of a positive muon traversing copper (solid line). The short dotted curve labeled “ $\mu^-$ ” shows the dependence of the stopping power on projectile charge at low energies (“Barkas effect”). Radiation losses and losses according to the Bethe-Bloch formula without density correction are shown as dotted and dash-dotted curves, respectively. Vertical bands indicate boundaries between the different momentum (energy) ranges.

Here  $T_{\max}$  is the maximum energy transferred in a single collision and  $I$  – the mean excitation potential.

The maximum energy transfer is produced by a head-on collision. For an incident particle of mass  $M$ , it reads:

$$T_{\max} = \frac{2m_e \cdot c^2 \cdot (\beta\gamma)^2}{1 + 2\frac{m_e}{M}\sqrt{1 + (\beta\gamma)^2} + \left(\frac{m_e}{M}\right)^2}. \quad (4.2.4)$$

The mean excitation potential,  $I$ , is theoretically a logarithmic average of the orbital frequencies weighted by the so-called oscillator strength of the atomic levels. In practice, it is deduced from the measurements of  $(-dE/dx)$  and a semi-empirical formula for  $I$  as a function of  $Z$ . One approximation is [3.2.4.4.1]:

$$\frac{I}{Z} = \left(12 + \frac{7}{Z}\right) \text{ eV}, \quad Z < 13$$

$$\frac{I}{Z} = \left(9.76 + 58.8Z^{-1.19}\right) \text{ eV}, \quad Z \geq 13. \quad (4.2.5)$$

In case of  $L(\beta)=L_0(\beta)$  the expression (4.2.1) is referred to as Bethe-Bloch equation [4.2.4]. In practice two corrections  $\Delta L$  are normally added: the density effect correction  $\delta$ , and the shell correction  $C$ , so that the expression (4.2.1) can be written as

$$-\frac{dE}{dx} = 2\pi \cdot N_A \cdot r_e^2 \cdot m_e \cdot c^2 \cdot \rho \cdot \frac{Z}{A} \cdot \frac{z^2}{\beta^2} \cdot \left( \ln\left(\frac{2m_e \cdot \gamma^2 \cdot v^2 \cdot T_{\max}}{I^2}\right) - 2\beta^2 - \delta - 2\frac{C}{Z} \right). \quad (4.2.5)$$

The shell correction [4.2.5] accounts for effects which arise when the velocity of the incident particle is comparable or smaller than the orbital velocity of the bound electrons. At such energies, the assumption made to obtain expression (4.2.1), that the electron is stationary with respect to the incident particle is no longer valid. The density effect arises from the fact that the electric field of the particle also tends to polarize the atoms along its path. Because of this polarization, electrons far from the path of the particle will be shielded from the full electric field strength. Collisions with these outer lying electrons will therefore contribute less to the total energy loss than predicted by the Bethe-Bloch formula.

There are several more corrections to the Bethe-Bloch formula applied for heavier charged particles. The Barkas correction [4.2.6] is to account for the polarization effects for low energy distant collisions. Lindhard-Sørensen correction [4.2.7] takes into account a finite nuclear size.

The energy loss due to ionization has its minimum around  $\beta\gamma \approx 3$ . Particles matching this condition are referred to as minimum ionizing particles, MIPs.

The Bethe-Bloch formula describes the average energy loss by ionization per unit of length. Because of the statistical nature, the spectrum of the actual energy loss in a medium depends on the material layer thickness. In a thin layer the rare occurrences of scattering with high momentum transfer lead to an asymmetric spectrum with a tail towards higher energy losses. Approaches have been made to describe the resulting spectrum with the help of a struggling function introduced by Bohr, Landau [4.2.8], Vavilov, Shulek, Bichsel and others [4.2.9]. In a thick layer the spectrum of the lost energy approaches a Gaussian distribution because the number of scattering events is high.

Figure 4.2.2 taken from [4.2.1] shows a highly skewed distribution of energy deposition for a 10 GeV muon traversing 1.7 mm of silicon. The Landau-Vavilov function (dot-dashed) uses the Rutherford cross section without atomic binding corrections but with a limit in kinetic energy transfer in a single collision. The solid curve was calculated using Bethe-Fano theory

[4.2.10, 4.2.11, 4.2.12].  $M_0(\Delta)$  and  $M_1(\Delta)$  are the cumulative 0<sup>th</sup> moment (mean number of collisions) and 1<sup>st</sup> moment (mean energy deposition) when crossing the silicon.  $\Delta_p$  is the most probable energy deposition defined as:

$$\Delta_p = \xi \left( \ln \frac{2m_\mu \cdot c^2 \cdot \beta^2 \cdot \gamma^2}{I} + \ln \frac{\xi}{I} - \beta^2 - \delta(\beta \cdot \gamma) + j \right), \quad (4.2.6)$$

where  $m_\mu$  is the muon mass,  $\xi=(K/2)(Z/A)(x/\beta^2)$  for a detector with a thickness  $x$ ,  $j=0.200$  [4.2.9], and  $K=4\pi \cdot N_A \cdot A \cdot r_e^2 \cdot m_\mu \cdot c^2$ .

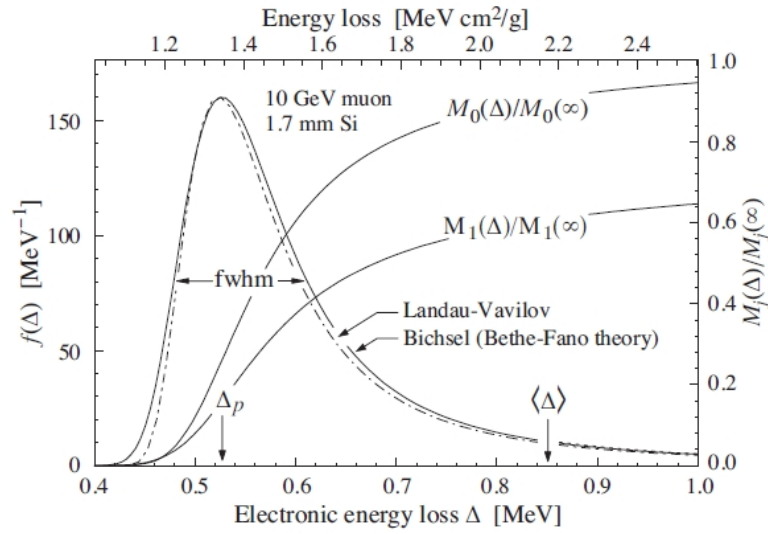


Figure 4.2.2: Energy loss spectrum for a 10 GeV muon traversing 1.7 mm of silicon (left scale). Also shown are the values of the 0<sup>th</sup> and 1<sup>st</sup> moments as a function of the energy loss (right scale).

The energy losses due to ionization are responsible for the signal formation in the sensor. In addition, there are energy losses which lead to the creation of permanent defects inside the lattice of the material and its degradation.

These are the energy losses by Coulomb scattering of a charged particle with the energy  $E$  off nuclei of the medium with the mass  $M_{nucl}$ . They read:

$$-\left(\frac{dE}{dx}\right)_{nucl} = 2\pi \cdot N_A \cdot (z \cdot Z \cdot e^2)^2 \cdot \frac{E^2}{p^2 \cdot M_{nucl} \cdot c^4} \left( \frac{A_s}{A_s + 1} - 1 + \ln \left( \frac{A_s + 1}{A_s} \right) \right), \quad (4.2.7)$$

with  $p$  being the momentum of the charged particle and  $A_s$  – the screening parameter for the single Coulomb scattering [4.2.13].

The Coulomb interactions of the incident charged particle with nuclei of the media lead to another energy losses dominating at high energies – the losses due to Bremsstrahlung:

$$-\left(\frac{dE}{dx}\right)_{Brems} = 4\alpha \cdot N_A \cdot \left(\frac{e^2}{mc^2}\right)^2 \cdot \frac{Z(Z+1)}{A} \cdot z^2 \cdot E \cdot \ln \frac{183}{Z^{\frac{1}{3}}}, \quad (4.2.8)$$

where  $\alpha$  is the fine structure constant and  $e$  – charge of the electron,  $m$  – mass of the incident particle,  $E$  – the energy of the incident particle. The Bremsstrahlung contribution is negligible for heavy charged particles. It becomes particularly important for high energy electrons and positrons.

### 4.3 Interaction of photons with matter

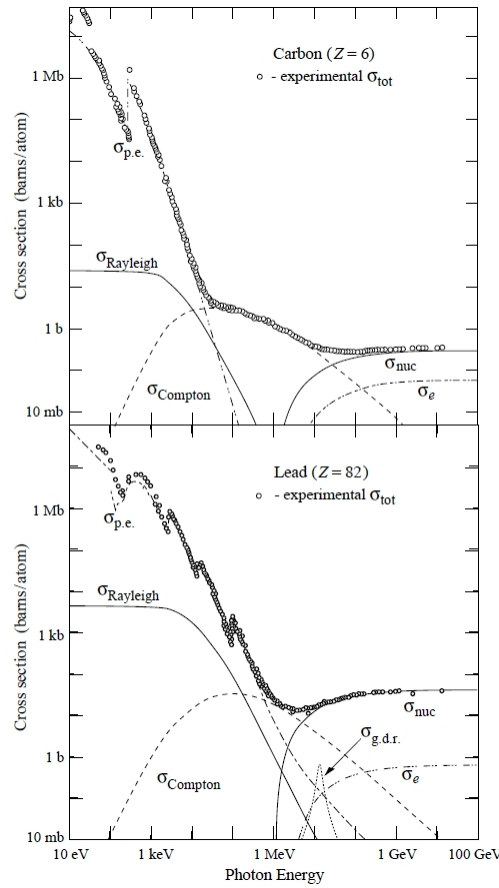


Figure 4.3.1: Photon total cross section as a function of energy in carbon and lead, showing the contributions of different processes [4.3.1];  $\sigma_{p.e.}$  denotes atomic photoelectric effect (electron ejection, photon absorption),  $\sigma_{Rayleigh}$  – Rayleigh (coherent) scattering,  $\sigma_{Compton}$  – Compton (incoherent) scattering,  $\sigma_{nucl}$  – pair production in the nuclear field,  $\sigma_e$  – pair production in the electron field,  $\sigma_{GDR}$  – photonuclear interactions, most notably the Giant Dipole Resonance [4.3.2].

Photons interact with matter via several processes. The cross-sections of the processes in a light (carbon) and heavy (lead) material are shown in Figure 4.3.1 as a function of the photon energy.

At low energies the photoelectric effect dominates. The photoelectric cross section is characterized by discontinuities, called absorption edges, which appear when the thresholds for photoionization at atomic levels are reached. At higher energies the contributions from Rayleigh and Compton scattering become more important. Rayleigh scattering is elastic scattering that leaves the state of the material unchanged. Compton scattering is inelastic scattering. Part of the energy of the photon is transferred to the scattered electron. If the photon energy exceeds twice the mass of electron, pair production becomes dominant. In this process the photon converts to an electron-positron pair or another elementary particle and its antiparticle.

In the photoelectric effect, Compton scattering and pair production charged particles are produced. These charged particles interact with matter as described in the previous section.

## 4.4 Energy deposition and signal creation

For a thin layer of material – like in case of a thin solid state sensor – only a part of the energy lost is deposited inside the material. An impinging charged particle creates electron-hole pairs. However, a few secondary electrons get larger energy, up to the kinematic limit given by Equation 4.2.4. These electrons ionize the material along their trajectories. Some of them, referred to as  $\delta$ -electrons, have energy enough to leave the thin sensor carrying away a certain amount of energy. Photons created in particles interactions, e. g. by Bremsstrahlung or by relaxation of previously excited material electrons, have a large probability to escape the sensor volume without interaction and thus without contributing to the energy deposition. A photon penetrating the sensor does not cause ionization directly, although it can produce an electron via photoelectric effect, Compton scattering or pair production.

The deposited energy creates ionization. In a semiconductor or isolator electrons are excited to the conduction band and holes – to the valence band. These free charge carriers drift inside an electric field. The total collected charge can be less than that created in ionization due to recombination and trapping of charge carriers. These processes are described later in the scope of the main sensor characteristics.

Figure 4.4.1 illustrates the connection between the energy loss and the signal from the sensor. It should be noted that the scheme reflects the situation for the case that the signal is represented by the integral of the collected charge. This representation is the most common, although not the only possible. The insights of an alternative representation will be discussed at the end of this chapter.

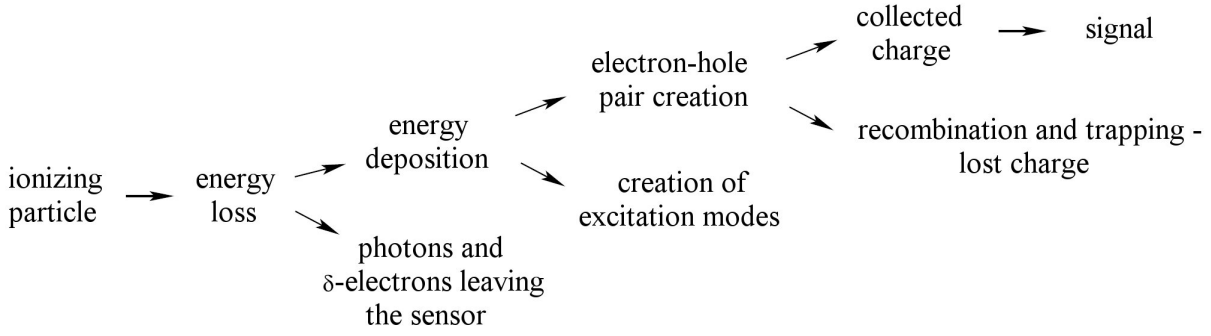


Figure 4.4.1: Scheme of the connection between the energy loss and the signal from the sensor.

Let us now consider the charge collection process in the sensor. For the parallel plate with  $d$  being the sensor thickness and the longitudinal dimensions of the electrodes much larger than  $d$ , a current flowing in the external circuit due to an electron or hole drifting with the velocity  $v$  in the electrical field is [4.4.1]:

$$I = \frac{e \cdot v}{d}. \quad (4.4.1)$$

The induced charge is given by the integral over a time interval:

$$Q_{coll}^i = \frac{e}{d} \int_0^{\tau_i} v^i(E_{e.f.}) dt = \frac{e}{d} \cdot v^i(E_{e.f.}) \cdot \tau^i \equiv \frac{e}{d} \cdot \delta^i, \quad (4.4.2)$$

where the index  $i$  represents either electron (e) or hole (h),  $E_{e.f.}$  is the electric field strength,  $\tau$  – the charge carrier lifetime and  $\delta$  – its drift length. Here a constant  $v^i(E_{f.e.})$  is assumed.

The charge carrier lifetime of an ideal crystal is infinite. In a real crystal imperfections are always present. These imperfections distort the band structure by introducing additional energy levels within the band gap. The drift length of the charge carriers,  $\delta^i$ , also known as Schubweg [4.4.2], describes the mean distance drifted by the charge carrier between the point of creation in the ionization process and the stopping point. The drift length is expressed as:

$$\delta^i = v^i(E) \cdot \tau^i = \mu(E) \cdot E \cdot \tau^i, \quad (4.4.3)$$

with  $\mu(E)$  being the mobility, which depends on the electric field strength. At some value of the electric field the product  $\mu(E) \cdot E$  becomes independent on  $E$ . The time the charge carrier can drift is limited by its lifetime and by the distance to the corresponding electrode.

Assuming  $n_0$  charge carriers of one sign at a certain moment of time at a distance  $z$  from the corresponding electrode, the amount of charge carriers after a time  $t$  can be calculated by:

$$n(t) = n_0 \cdot \exp\left(-\frac{t}{\tau^i}\right). \quad (4.4.4)$$

It can be also expressed in terms of the drift length and drifted distance  $z$ :

$$n(z) = n_0 \cdot \exp\left(-\frac{z}{\delta^i}\right). \quad (4.4.5)$$

To calculate the induced charge from  $n_0$  charge carriers drifting inside the sensor the expression (4.4.2) is then modified:

$$\begin{aligned} Q_{coll}^i &= \frac{e}{d} \cdot v^i(E_{e.f.}) \int_0^{z/v^i} n(t) dt = n_0 \cdot \frac{e}{d} \cdot v^i(E_{e.f.}) \cdot \tau^i \left(1 - \exp\left(-\frac{z/v^i}{\tau}\right)\right) \\ &= n_0 \cdot \frac{e}{d} \cdot \delta^i \cdot \left(1 - \exp\left(-\frac{z}{\delta^i}\right)\right). \end{aligned} \quad (4.4.6)$$

If the distribution of the charge carriers density  $\rho^i(z)$  in the sensor volume is such that

$$\int_0^d \rho^i(z) dz = n_0, \quad (4.4.7)$$

then the expression for the induced charge reads:

$$Q_{coll}^i = \frac{e}{d} \int_0^d \rho^i(z) \int_0^{(d-z)/v^i} \frac{n(t)}{n_0} \cdot v^i dt dz = \frac{e}{d} \cdot \delta^i \int_0^d \rho^i(z) \cdot \tau^i \left(1 - \exp\left(-\frac{z-d}{\delta^i}\right)\right) dz. \quad (4.4.8)$$

To obtain the expression (4.4.8) it was assumed that the lifetime of the charge carrier is constant. This may not be the case in a polycrystalline material like pCVD diamond where it may depend on the  $z$  position. Taking into account equation (4.4.3) the expression (4.4.8) can then be rewritten:

$$Q_{coll}^i = \frac{e}{d} \int_0^d \delta^i(z) \cdot \rho^i(z) \cdot \left(1 - \exp\left(-\frac{z-d}{\delta^i(z)}\right)\right) dz. \quad (4.4.9)$$

For the mean drift length of the charge carrier much smaller than the sensor thickness and constant  $\rho^i(z)$  the expression (4.4.9) simplifies

$$Q_{coll}^i \approx Q_{gen} \frac{\overline{\delta^i}}{d}, \quad (4.4.10)$$

with  $Q_{gen} = e \int_0^d \rho^i(z) dz$  and  $\bar{\delta}^i = \frac{1}{d} \int_0^d \delta^i(z) dz$ . The total induced signal is the sum of the hole and the electron contribution. Assuming that  $\rho^e(z) = \rho^h(z)$  which is true for ionization, the expression (4.4.10) reads:

$$Q_{coll} \approx Q_{gen} \frac{\bar{\delta}^e + \bar{\delta}^h}{d} \equiv Q_{gen} \frac{\delta^Q}{d}, \quad (4.4.11)$$

where the  $\delta^Q$  is the charge collection distance.

A more pragmatic quantity which does not require any approximation is the charge collection efficiency defined as

$$CCE = \frac{Q_{coll}}{Q_{gen}} \approx \frac{\delta^Q}{d}. \quad (4.4.12)$$

In the next section the effects of the sensor irradiation on its CCE are discussed.

## 4.5 Polarization and pumping

As it was already mentioned above, a real crystal always contains defects. Point, line, planar and bulk defects are distinguished. Point defects are defects that occur only at or around a single lattice point. Vacancies, interstitials, substitutional atoms, antisites (exchange positions of atoms of different types) belong to point defects [4.5.1]. Line defects are those which occur along a line. They are different types of dislocations [4.5.2]. Planar defects occur along a 2-dimensional surface [4.5.3]. Bulk defects are small regions of point defects clustered together.

Furthermore, the bulk damage by hadrons and high energetic leptons or gamma photons is caused primarily by displacing a primary knock on atom out of its lattice site resulting in an interstitial and a left over vacancy, the so-called Frenkel pair. Thus, irradiation increases the number of defects in the material, mainly the point defects. High energetic leptons and hadrons along with point defects can produce clusters. The cluster model was first introduced by Gossick [4.5.4]. In this section the influence of the point defects is considered only. Although the picture is simplified, it qualitatively describes the experimentally observed behavior. The point defects in a monatomic material are illustrated in Figure 4.5.1.

Defects distort the band structure by introducing additional energy levels  $E_d$  in the band gap. In thermal equilibrium the probability that the electronic state with energy  $E_d$  is occupied by an electron is given by the Fermi-Dirac distribution function:



$$F(E_d) = \frac{1}{1 + e^{\frac{E_d - E_F}{kT}}}, \quad (4.5.1)$$

with  $E_F$  being the Fermi level,  $T$  – the temperature and  $k$  – the Boltzmann constant. The energy levels can be deep or shallow. Energy levels with  $(E_d - E_F)$  nearly equal to the half of the band gap width,  $E_g$ , are shallow defect levels. They can be easily occupied at room temperatures. Energy levels close to the middle of the band gap, meaning that  $(E_d - E_F)$  is close to zero, are deep levels. They are practically not occupied at room temperature, but can be filled by excess charge carriers.

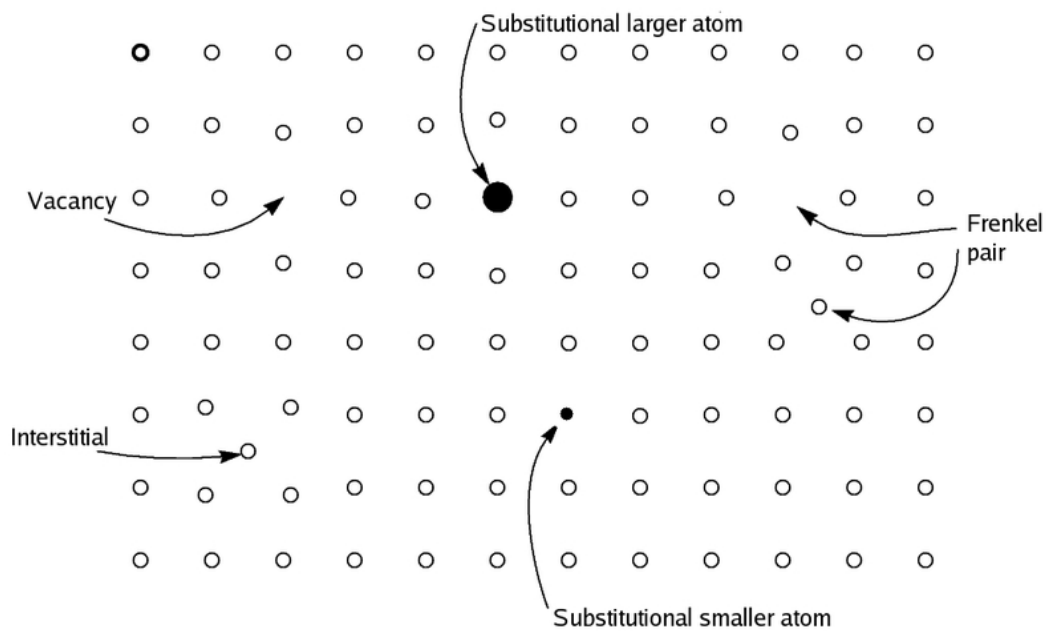


Figure 4.5.1: Schematic illustration of some simple point defect types in a monatomic solid.

Defect energy levels act via three processes schematically shown in Figure 4.5.2: trapping, recombination and generation of charge carriers. The charge carriers from the valence or conduction band can be captured by the defect level (process 1) and then re-emitted after some time (process 1'). The captured charge does not contribute to the signal, if the time constant is large. The rate per unit of volume for the process 1 is given by the density of not occupied defect levels  $n_d$ , the density of free charge carriers  $n_c$ , the capture cross section  $\sigma_t$  and the thermal velocity of the carrier  $v_{th}$ :

$$r_d = n_d \cdot n_c \cdot \sigma_t \cdot v_{th}. \quad (4.5.2)$$

An occupied energy level within the band gap can capture a carrier of the opposite sign and recombination occurs (process 2). It can also generate an electron-hole pair (process 3). The recombination rate is:

$$r_r = n_r \cdot n_{oc} \cdot \sigma_r \cdot v_{th}, \quad (4.5.3)$$

where  $n_{oc}$  is the density of occupied defect levels and  $\sigma_r$  is the capture cross section for charge carriers of the opposite sign.

A trapped charge can be emitted thermally. The temperature dependence of the emission rate is:

$$r_e = s \cdot n_{oc} \cdot \exp(-E_{\Delta}/kT), \quad (4.5.4)$$

where  $s$  is the frequency factor, typically in the range  $10^{12} \text{ s}^{-1}$  to  $10^{14} \text{ s}^{-1}$ ,  $E_{\Delta} = E_C - E_d$  for electrons and  $E_{\Delta} = E_d - E_V$  for holes,  $E_V$  and  $E_C$  are the top of the valence band and the bottom of the conduction band respectively.

The charge re-emitted after some delay (process 1') as well as the electron-hole pair generated in the process 3 do not contribute to the signal, if the time constants are large compared to the time interval set for the data acquisition system.

Trapped carriers give rise to two phenomena important for the sensor operation and experimentally observed: polarization and pumping (also known as priming).

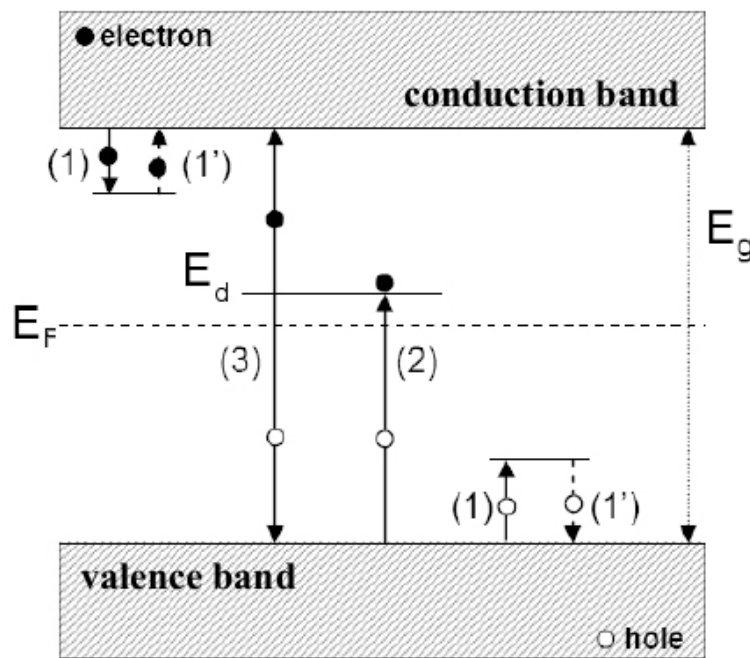


Figure 4.5.1: The simplified mechanism of trapping (1), re-emission (1'), recombination (2) and generation (3) of charge carriers according [4.5.5].

Figure 4.5.2 illustrates the development of polarization. Polarization occurs due to creation of space charge. Two cases are shown in the figure: inhomogeneous trap filling by the charge carriers created by short-range ionizing particles and homogeneous trap filling by long-range ionizing particles. For the short-range ionizing particles hitting the sensor, the region of ionization is limited to the volume close to one of the electrodes. The majority of the charge

carriers of one sign reach the corresponding electrode while the charge carriers of the opposite sign, drifting through the bulk, can be trapped and create the space charge. The space charge gives rise to an internal electric field  $E_{pol}$  which lowers the resultant electric field in the volume. In case of long-range ionizing particles and non-negligible CCE the charge carriers drift apart, each to the corresponding electrode, and are trapped at some point. The resulting space charge regions inside the sensor create an internal electric field opposed to the applied external field. This leads to recombination at low field, lowering the collected charge and therefore, the measured signal.

The mechanism of trap filling can lead to signal enhancement. If traps are occupied, the lifetime of free carriers increases due to the lower free trap density. This phenomenon is called pumping or priming [4.5.6, 4.5.7].

The CCE of the sensors under irradiation may be different from its initial CCE, lowered by polarization and enhanced due to pumping.

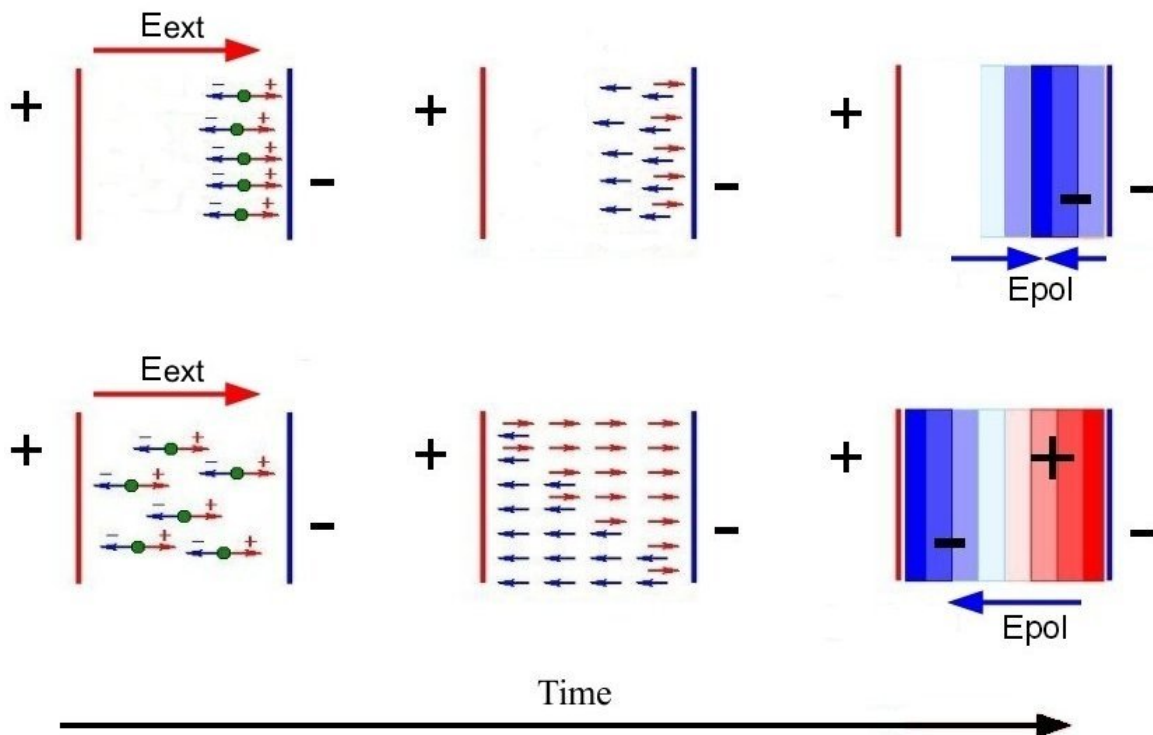


Figure 4.5.2: Development of polarization in case of short-ranged (top) and long-ranged (bottom) particles hitting the sensor. Pictures to the left show creation of electron-hole pairs due to ionization. Middle pictures show the drift of the charge carriers in the electric field. Right pictures show the regions of the space charge that create an internal electric field. The gradations of red and blue denote the regions of negative and positive trapped charge with different concentrations, respectively. The blue arrows denote the internal electric field  $E_{pol}$  which is reversed to the external electric field  $E_{ext}$ .

## 4.6 Sensor characterization

Among a variety of sensor characteristics there are two which are essential for operation: the current-voltage characteristics (IV) and the CCE. The IV represents the current through the sensor as a function of bias voltage. The current is measured when the sensor is not exposed to any ionizing particles – the so-called dark current. The dark current contributes to the noise of the readout electronics, therefore the dark current of the sensors should be kept low. Another characteristic is the CCE which defines the signal size to be expected from the sensor. All the sensors considered in the thesis were characterized using the setups described below.

### 4.6.1 The IV setup

The IV characteristics of the sensors were measured with the setup schematically shown in Figure 4.6.1.1. A picoammeter Keithley 487 with an integrated voltage supply provides bias voltage and measures the current in the circuit with a resolution of 10 fA. The sensor represented by its capacitance and resistance,  $C_s$  and  $R_s$  respectively, is placed inside shielded light-tight box filled with nitrogen. Dry nitrogen atmosphere is purposed to minimize the effect of moisture and maintain reproducibility of results. Parasitic capacitance and resistance of the clamps are represented by  $C_{||}$  and  $R_{||}$  respectively. The resistance  $r$  is the internal resistance of the picoammeter limiting the current fed into the device.

The measurement procedure is the following. Bias voltage is changed in steps of 25-50 V in the range -500 V to 500 V. Positive bias voltages are applied first. After each voltage change a period of 40 s is allowed for the current to settle. Then the current is measured once per second within 10 seconds. The result is the average of the 10 values.

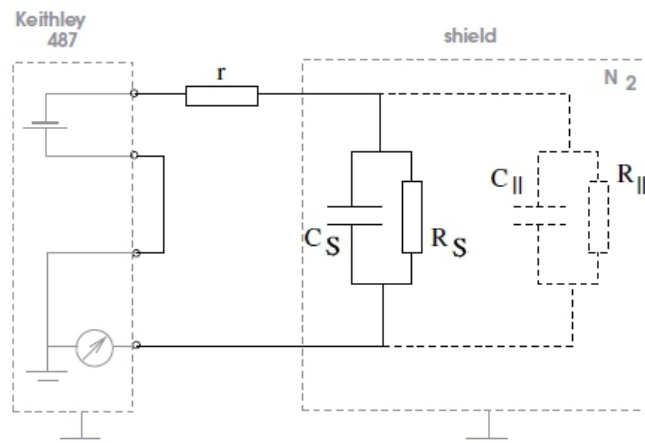


Figure 4.6.1.1: The schematic view of the IV setup.

## 4.6.2 The CCE setup

The CCE of the sensors is measured as response to single MIPs. The setup for the CCE measurements is schematically shown in Figure 4.6.2.1. The sensor is placed inside a shielded light-tight box. It is read out with a charge sensitive preamplifier Amptec 250, the output signal of which is fed to the charge integrating ADC CAEN v265 or v965. A holder with a collimator and a  $^{90}\text{Sr}$  source is positioned above the sensor. Two plastic scintillators inside a light-tight box are placed below the sensor. Each is read out by a PMT.

The collimated flux of electrons from the source hits the sensor. The distance from the sensor and the source and the size of the collimator opening are adjusted such that the signals from single electrons have only a small possibility to overlap. The most energetic electrons from the spectrum of a  $^{90}\text{Sr}$  source are MIPs. Only they are able to pass through the sensor and hit both scintillators. A coincidence signal from the two PMTs gates the ADC.

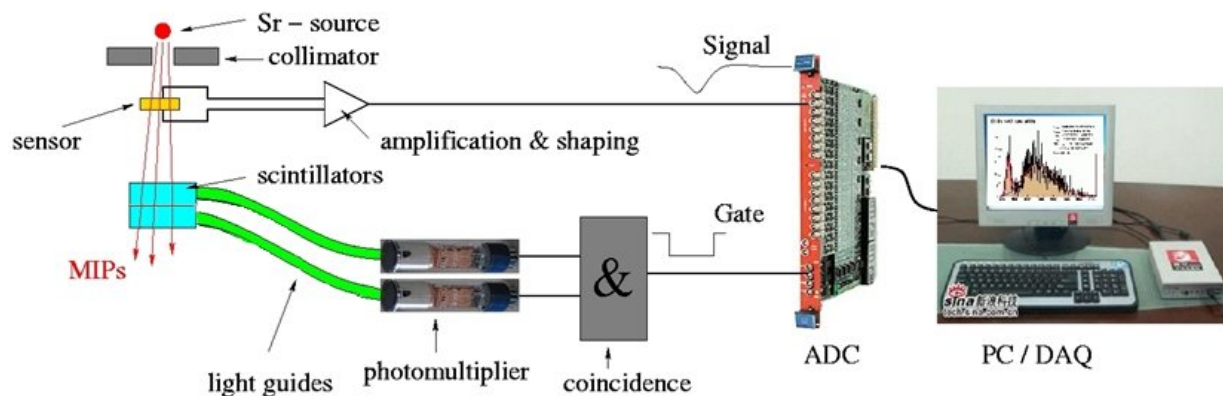


Figure 4.6.2.1: The CCE setup.

A typical measured signal spectrum is shown in Figure 4.6.2.2. Both signal (right) and pedestal (left) distributions are visible. The pedestal can be described with a Gaussian. Its width is defined by the total equivalent noise charge (ENC) of the electronics,  $\sigma_{\text{ENC}}$ . According to section 4.2, the signal distribution can well be described with a Landau distribution. The influence of the electronic noise can be taken into account by convolution the Landau distribution with a Gaussian distribution. For a typical fit of the signal spectrum, the width of the Gaussian convoluted with the signal Landau distribution is higher than the width of the pedestal peak. This can be explained by fluctuations of the drift length of the charge carriers in the sensor. The fluctuations introduce an additional Gaussian to the convolution with the width  $\sigma_{\text{drift}}$ .

The collected charge and therefore the CCE is proportional to the difference between the most probable value of the signal distribution and the mean value of the pedestal distribution, as indicated by the green arrow in Figure 4.6.2.2.

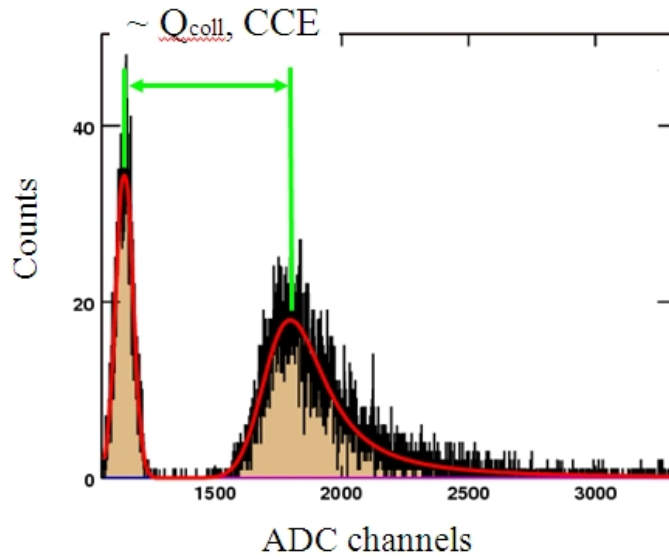


Figure 4.6.2.2: An example of the signal spectrum. The green arrow indicates the quantity proportional to the collected charge and the CCE.

The calibration procedure with charge injection from a pulse generator makes correspondence between the ADC channels and the charge.

For sensors with very low CCE the MIP signal may not be well separated from the pedestal. In such cases a modified IV setup shown in Figure 4.6.2.3 is used. The  $^{90}\text{Sr}$  source was placed at a certain distance above the sensor, and the IV characteristic was measured with the sensor under irradiation. The charge collection efficiency at a certain bias voltage was estimated using the following relation:

$$I = \varepsilon \Phi \cdot n \cdot d \cdot A, \quad (4.6.2.1)$$

where  $\varepsilon$  is the charge collection efficiency,  $\Phi$  – the flux of the particles passing through the sensor,  $n = (dE/dx)/E_{\text{eh}}$  – the number of the charge carriers created by the particles per unit length,  $E_{\text{eh}}$  – energy to create an electron-hole pair,  $d$  – the sensor thickness and  $A$  – the area of the pad. The signal current  $I$  – is the difference between the current measured with the source and the dark current. For simplicity it was assumed that all the particles passing through the sensors to be MIPs, so in fact  $\Phi$  denoted the equivalent flux of MIPs with the same total energy deposition in the sensor material as for the particles from the  $^{90}\text{Sr}$  spectrum.

The equivalent flux  $\Phi$  was obtained using the expression (4.6.2.1) and a reference measurement for a sensor with known CCE.

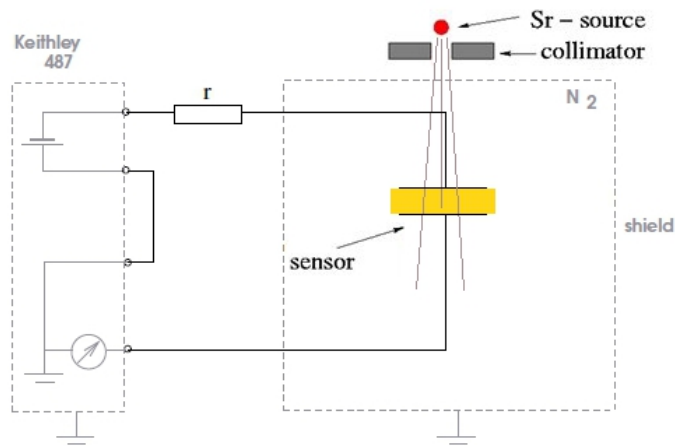


Figure 4.6.2.3: The IV setup modification for the CCE estimates.

### 4.6.3 The setup for radiation hardness tests

The radiation hardness of the sensors was studied with a 10 MeV electron beam of the Superconducting Darmstadt Linear Accelerator (S-DALINAC) [4.6.3.1]. The sensor under test was installed inside a portable shielded box that could fit to both the irradiation setup and the CCE setup. The procedure of the measurements is depicted in Figure 4.6.3.1. The sensor was biased with the operating voltage defined by previous measurements of the CCE as a function of bias voltage. The bias voltage was kept constant at all times till the end of the measurements. In the beginning, the CCE was measured. Simultaneously, the beam current was tuned to the required value. The beam current varied in the range of 10 nA to 100 nA, the lower values were used in the beginning. After the CCE measurement the sensor was transported to the beam area and installed into the irradiation setup. Irradiation for approximately one hour followed. After that the sensor was transported for the CCE measurement and the procedure repeated. In case of the sapphire sensors already the initial CCE was too low to be measured with the CCE setup. It was calculated using expression 4.6.2.1.

The schematic view of the irradiation setup is shown in Figure 4.6.3.2. A collimator with an opening aligned with the sensor. A large part of the beam went through the opening, the sensor and was stopped in a Faraday cup. The rest of the beam was absorbed by the collimator. The collimator size corresponded to the size of the sensor. The currents in the collimator, in the Faraday cup and in the sensor circuit were measured with ammeters.

The Faraday cup current is used to determine the beam current which in turn is utilized for the calculation of the absorbed dose. A GEANT 4 simulation of the setup [4.6.3.2] gives correspondence between the beam current, Faraday cup current and energy deposition in the sensor material allowing for correcting to electrons scattered at large angles in the sensor. The energy deposition is used for calculation of the absorbed dose. The collimator current along with Faraday cup current are used for a cross-check of the beam current.

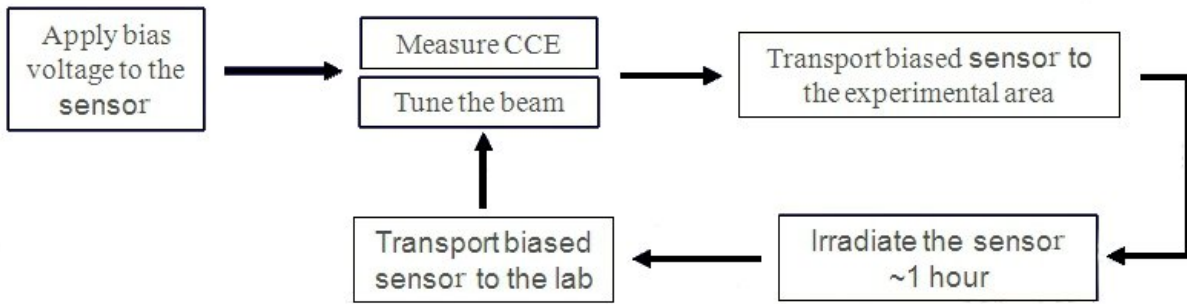


Figure 4.6.3.1: The scheme of the irradiation measurements.

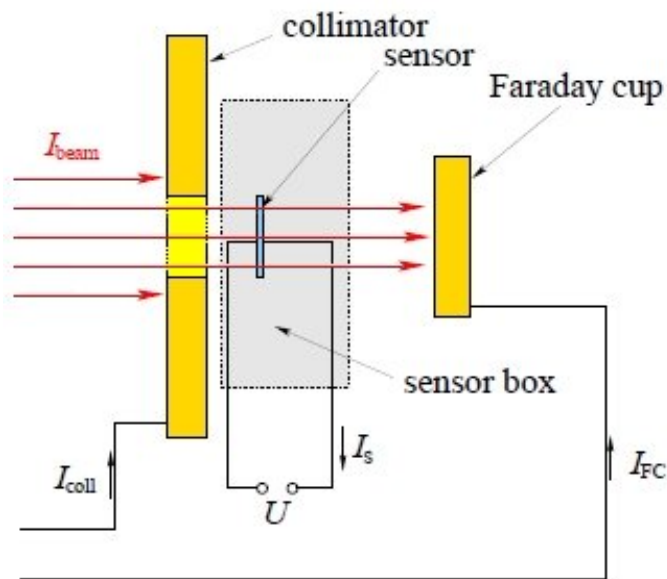


Figure 4.6.3.2: The schematic view of the irradiation setup.

## 4.7 Diamond sensors

Diamond is a unique material with excellent physical properties. Table 4.7.1 shows the main properties of diamond in comparison with those of silicon. However, only the CVD process of diamond growth brought the purity of synthetic diamond to an ultra-high level. This level of purity allows diamond to become radiation sensor material thanks to its properties that include a very low leakage current with negligible temperature dependence, relatively large signal size, very good radiation hardness and low dielectric constant. Diamond sensors were successfully operated in different types of application like strip detectors for the time-of-flight measurements [4.7.0.1], beam conditions and beam loss monitoring [3.3.2, 3.3.4], beam halo monitor [3.3.3] and tissue-equivalent beam profile monitor for medical application [4.7.0.2].



Property	Diamond	Silicon
Density, g/cm <sup>3</sup>	3.52	2.32
Hardness, Moh	10	7
Dielectric constant	5.7	11.9
Resistivity, Ω·cm	~10 <sup>6</sup>	2.3·10 <sup>5</sup>
Breakdown field, V/μm	1000	30
Thermal conductivity, W/(cm·K)	20	1.3
Band gap, E <sub>g</sub> , eV	5.47	1.12
Ionization energy, E <sub>eh</sub> , eV	13	3.6
Saturated carrier velocity, cm/s	2.7·10 <sup>10</sup>	8.2·10 <sup>9</sup>
Electron mobility, cm <sup>2</sup> /(V·s)	4500	1350
Hole mobility, cm <sup>2</sup> /(V·s)	3800	480
Ionization density (MIP), e-h/μm	36	92

Table 4.7.1: Properties of diamond and silicon under normal conditions.

#### 4.7.1 Material and metallization

Among several synthetic diamond manufacturers there is one known to have good reproducibility of the relevant characteristics, Element Six [4.7.1.1]. The company has developed a range of electronic grade CVD diamond material (single crystal and polycrystalline plates) that can be specifically utilized as sensors for ionizing radiation. The sensors are grown by the chemical vapor deposition (CVD) method. The CVD process involves gas-phase chemical reactions above a solid surface where the deposition occurs. The process of diamond growth by CVD can be described as:



The CVD diamond production involves three steps: activation of the gas phase, nucleation and diamond growth. Activation provides radicals for further chemical reactions. The activation can involve thermal methods (e.g., a hot filament), electric discharge (e.g., DC, RF or microwave), or a combustion flame (such as an oxyacetylene torch). To start diamond growth individual carbon atoms should be nucleated onto a substrate surface forming an initial lattice. The proper choice of the substrate is important. The perfect match is diamond, either natural or a synthetic grown by high pressure high temperature (HTHP) method. Silicon is another widely used material due to the same lattice structure and good availability of the material. Recently iridium substrates are under investigation [4.7.1.2].

Growth starts on a substrate (e. g. silicon) with randomly oriented micro-crystallites (clusters) at the nucleation sites. The nucleation finishes when the clusters reach a critical size and become stable. The growth phase starts in all three dimensions till the cluster coalesces with neighbor ones. Since this stage the growth occurs only in one direction upward from the substrate providing a columnar structure of the diamond. The quality on the substrate side is generally poor due to the small crystalline size and the high density of grain boundaries. The quality increases with the thickness. Therefore, the upper part is used as sensor material.

Element Six specifies the concentrations of the main impurities for the ultra-pure diamond material: nitrogen concentration below 50 ppb (purity better than 99.995 %), boron concentration below 1 ppb (better than 99.9999 %).

The diamond sensors investigated were made of plates measuring  $12 \times 12 \times 0.3 \text{ mm}^3$ . An example is shown in Figure 4.7.1.1. The price for a piece of such material was 1800 euro. The metallization is one square  $8 \times 8 \text{ mm}^2$  pad on both sides consisting of Ti/Pt/Au layers of 50/50/200 nm thickness, respectively, done in Target Lab of GSI. The following steps were made:

1. mount the sample into the mask holder for later metallization to check if spacer and masks fit to the diamond size, then dismount
2. clean/oxidize in  $\text{H}_2\text{SO}_4 + \text{HNO}_3$  (3:1) (270 °C for 30 min) and then cool down for ~1 hour
3. clean/swirl in ultrapure water
4. clean/oxidize in  $\text{HCl} + \text{H}_2\text{O}_2$  (1:1) (50 °C for 10 min) and then cool down for ~30 min
5. clean/swirl in ultrapure water
6. dry the sample by flushing with nitrogen and store the sample in a nitrogen box till the metallization procedure
7. apply oxygen plasma for 8 min at ~0.35 mbar and 85 W microwave power to each sample side
8. mount the sample into mask holder
9. move the mask holder into a vacuum chamber, evacuate chamber
10. do a short glow discharge in Argon
11. metalize the sample by sputtering
12. remove the sample out of chamber and holder
13. do annealing in Argon at ~500 °C for ~10 min
14. check metallization under microscope

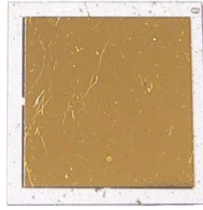


Figure 4.7.1.1: An example of metalized diamond sensor.

## 4.7.2 Sensor characterization

In this section the characteristics of the pCVD diamonds from the Element Six are presented. The results shown below are obtained from 300  $\mu\text{m}$  thick sensors at room temperature, around 20  $^{\circ}\text{C}$ .

A typical IV curve for the diamonds produced in 2010 is shown in Figure 4.7.2.1. The dark currents were within a few pA for both polarities of the bias voltage.

For some sensors erratic currents were observed at constant bias voltages as shown in Figure 4.7.2.2.

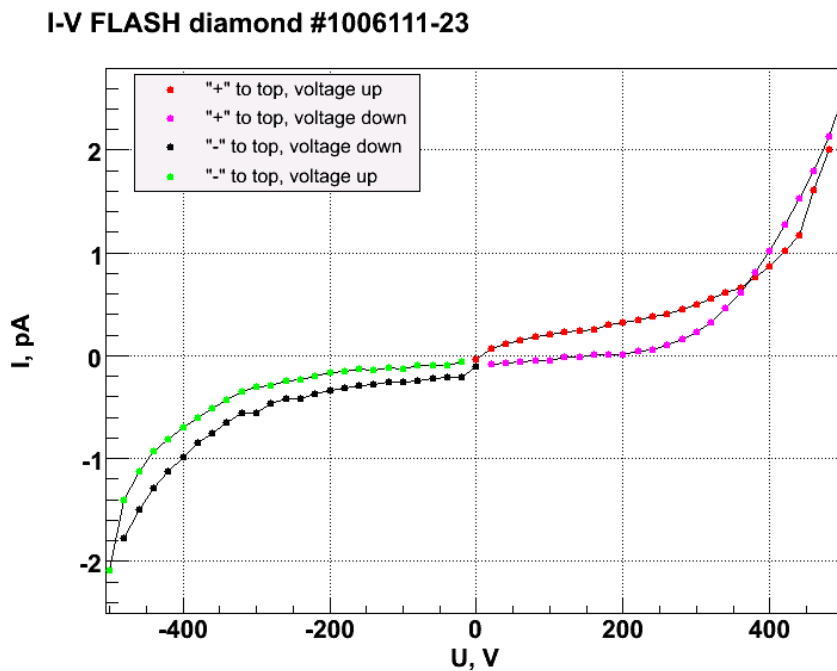


Figure 4.7.2.1: A typical I-V characteristics of diamond sensor.

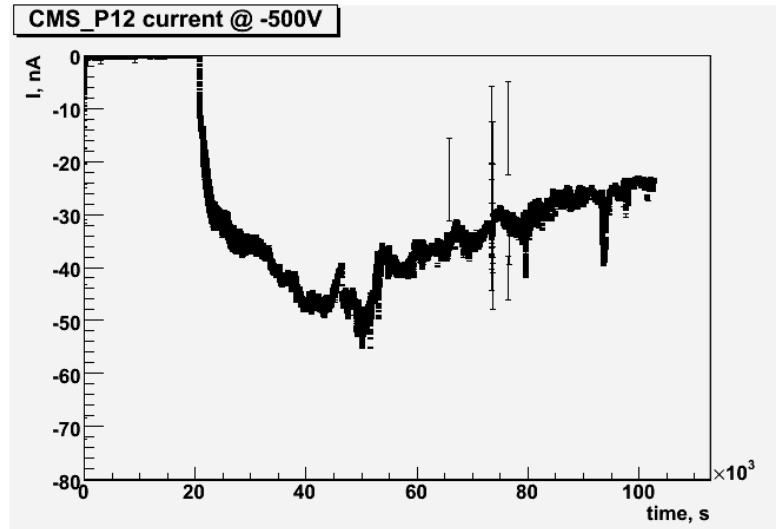


Figure 4.7.2.2: An example of behavior of the current of a diamond sensor with time at constant bias voltage.

The CCE of the sensor shown in Figure 4.7.2.3 rose with bias voltage and reached saturation at around 1 V/ $\mu\text{m}$ . At a constant bias voltage the CCE tended to decrease with time. Apparently, polarization grew up. The saturated value of the CCE was in the range 20-50 %. Under irradiation by the  $^{90}\text{Sr}$  source with the dose rate of about 0.2 Gy/h an enhancement of the CCE was observed, as demonstrated in Figure 4.7.2.4.

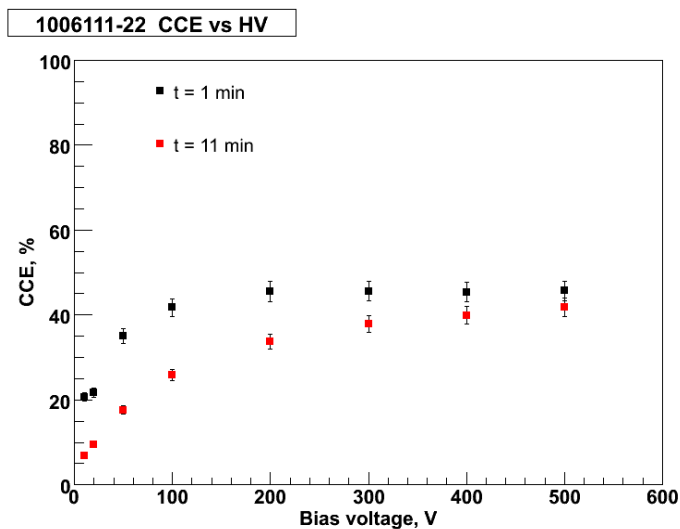


Figure 4.7.2.3: The CCE dependence on bias voltage measured immediately after a certain value of bias voltage was applied (black) and after 11 min (red).

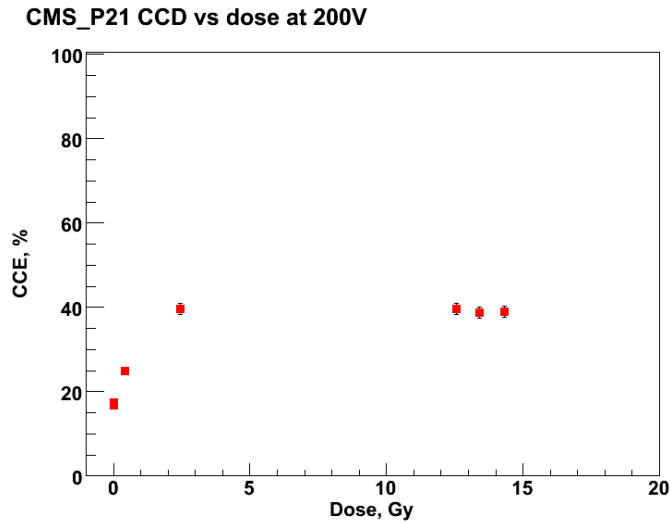


Figure 4.7.2.4: The CCE as a function of the dose from a  $^{90}\text{Sr}$  source.

As it was mentioned, radiation tolerance of the diamond material has been investigated with protons, pions and photons. To prove radiation hardness of the diamond under irradiation with high energy electrons, experiments with 10 MeV electrons have been carried out as described in section 4.6.3. The CCE dependence on the absorbed dose for two diamond sensors is shown in Figure 4.7.2.5 [4.7.2.1]. They revealed similar behavior. The CCE rose in the region of low doses and started to drop down for doses above 500 kGy. The initial rise can be explained by pumping. The degradation is assumed to be the result of material lattice degradation followed by polarization. The signal after absorption of around 7 MGy amounted to 70 % of its initial value.

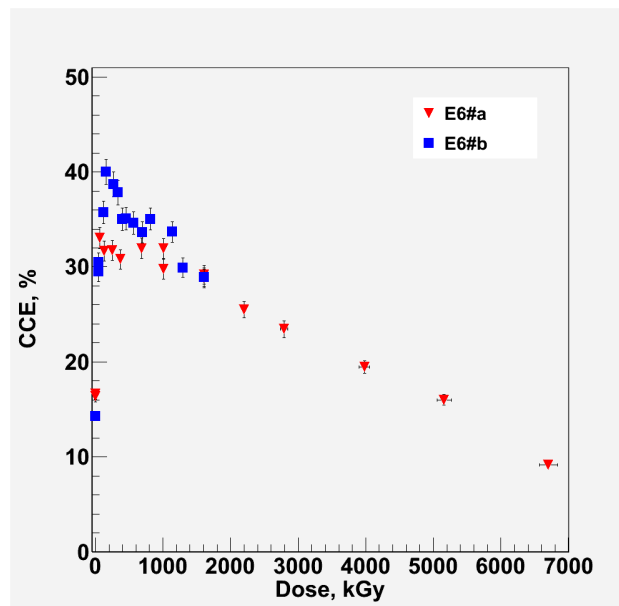


Figure 4.7.2.5: The CCE as a function of the absorbed dose for 2 diamond sensors.

The leakage current for diamond sensors rises up to 2 times after absorbing a dose of up to 7 MGy as shown in Figure 4.7.2.6.

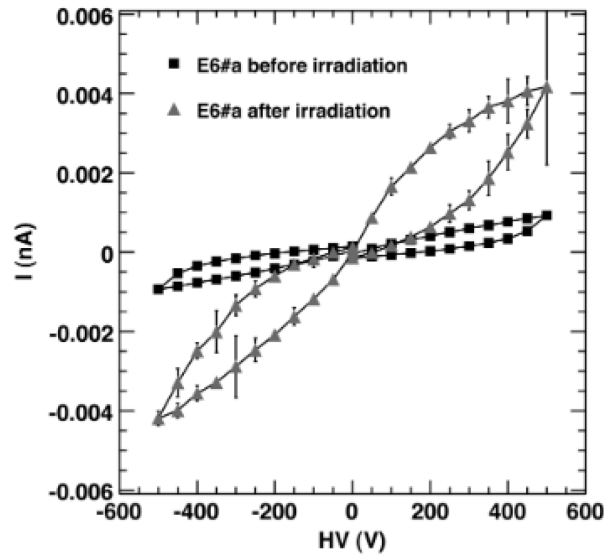


Figure 4.7.2.6: Leakage currents for a diamond sensor before and after irradiation, the absorbed dose is 7 MGy.

### 4.7.3 Beam profile measurements

In order to prove that diamond sensor can sense variations in the intensity of the impinging particles, beam profile measurements were carried out at photoinjector test facility in Zeuthen (PITZ) [4.7.3.1]. The tests also aimed to check the bias voltage and signal readout scheme. A diamond sensor was assembled in the holder as can be seen in Figure 4.7.3.1 and could be moved horizontally through the 6 MeV electron beam. The bias and signal readout scheme which later has been selected for the BHM at FLASH and the E-XFEL is shown in Figure 4.7.3.2. The cores of two coaxial cables were used to supply bias voltage and one coaxial cable was used to read out the signal. A high voltage filter box containing capacitors to support the charge necessary for signal generation was placed 1.5 m away from the sensor. The value of the capacitor was chosen to be large enough to contain the charge sufficient to support the signal current, but not too large to be able to release it fast. 40 m long cables connected the HV power source (Keithley 487) and the scope for signal readout.

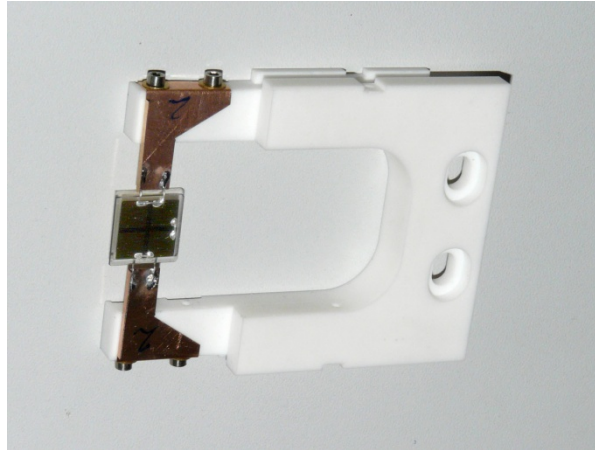


Figure 4.7.3.1: The diamond sensor assembled for beam profile measurement at PITZ.

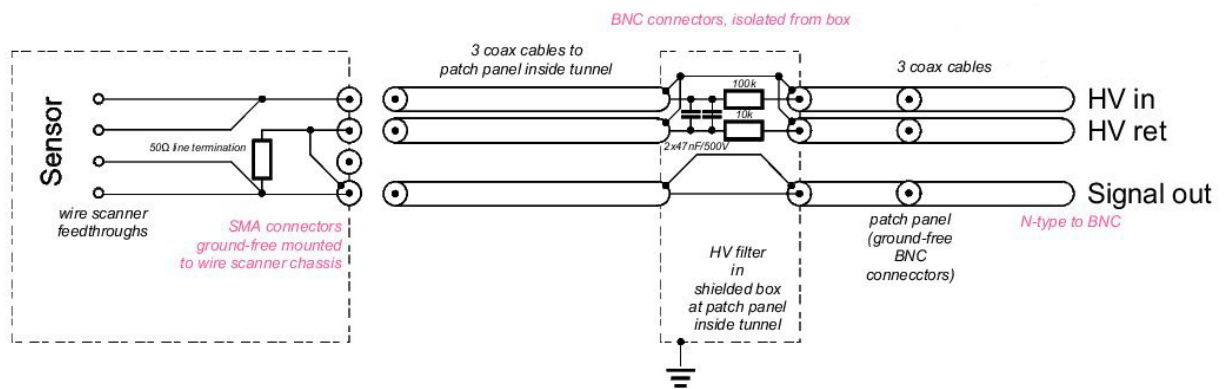


Figure 4.7.3.2: Sensor bias and signal readout scheme for the diamond sensor for the beam profile measurement at PITZ.

The beam size was adjusted such that the size of its core in the sensor plane was approximately equal to the sensitive area of the sensor. The beam profile and comparison with the sensor size is shown in Figure 4.7.3.3. As the sensor was moved through the beam, the signal size was calculated as the integral over the waveform of the response as shown in Figure 4.7.3.4. The signal obtained at a bias voltage of 200 V when an electron bunch of 10 pC crossed the sensor is shown as a function of the horizontal position of the sensor in Figure 4.7.3.5. The dependence is nearly the same for the forward and backward movement of the sensor. Both measurements show the beam displacement of 5 mm in horizontal direction.

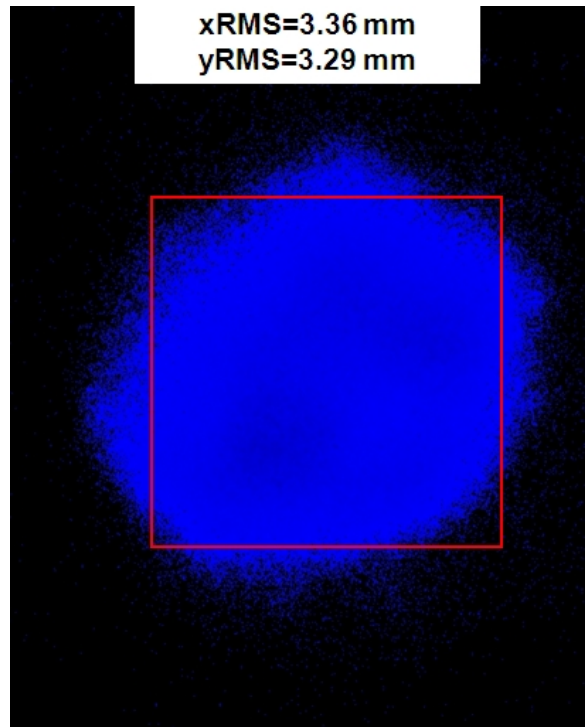


Figure 4.7.3.3: The beam profile (blue spot) and relative dimensions of the diamond sensor ( $12 \times 12 \text{ mm}^2$ ).

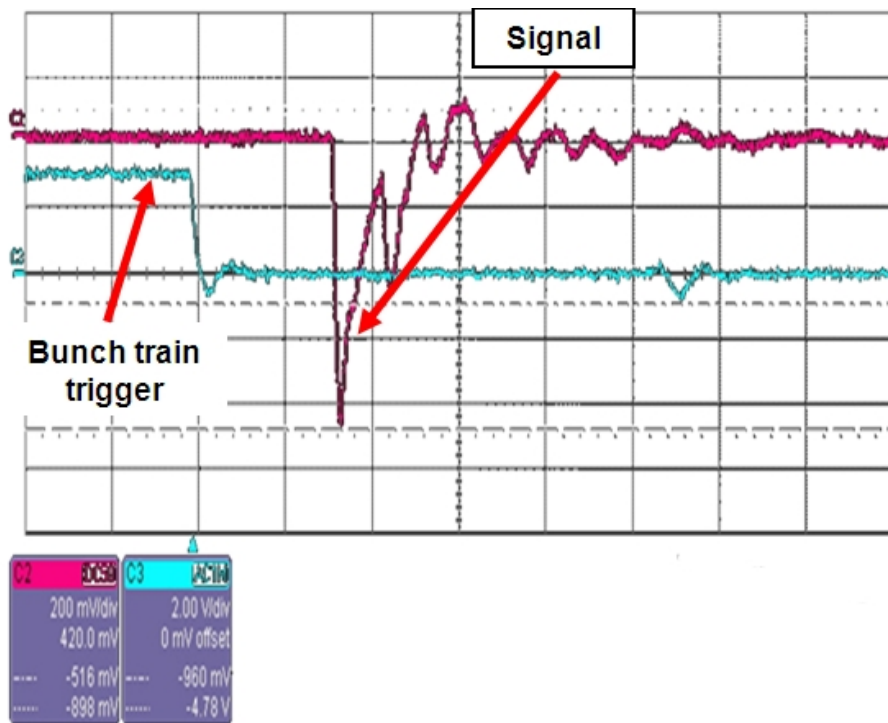


Figure 4.7.3.4: Signal from the diamond sensor during beam profile measurement at PITZ. The vertical scale for the signal is 200 mV/div, horizontal – 50 ns/div.



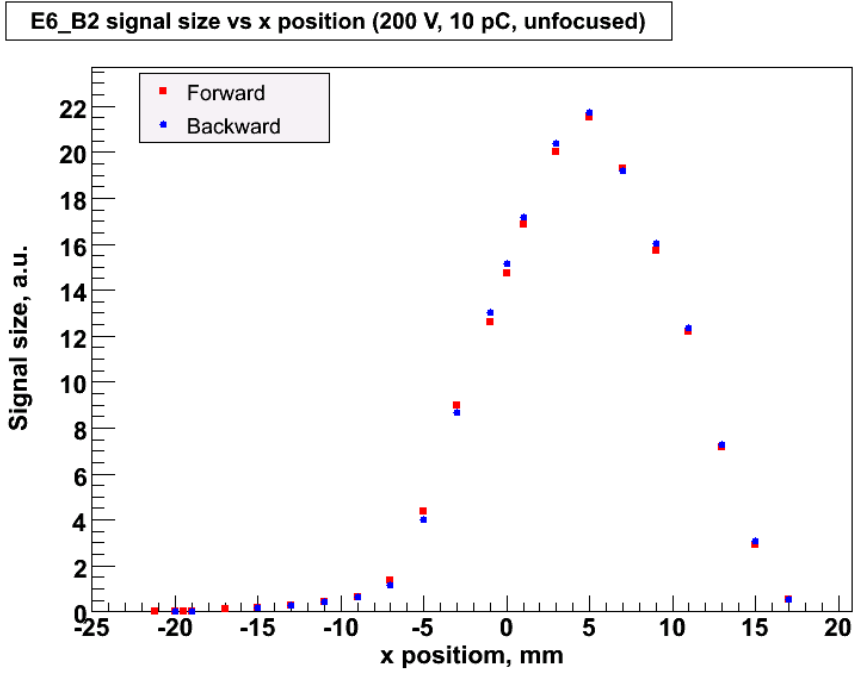


Figure 4.7.3.5: The dependence of the signal from the diamond sensor on its horizontal position.

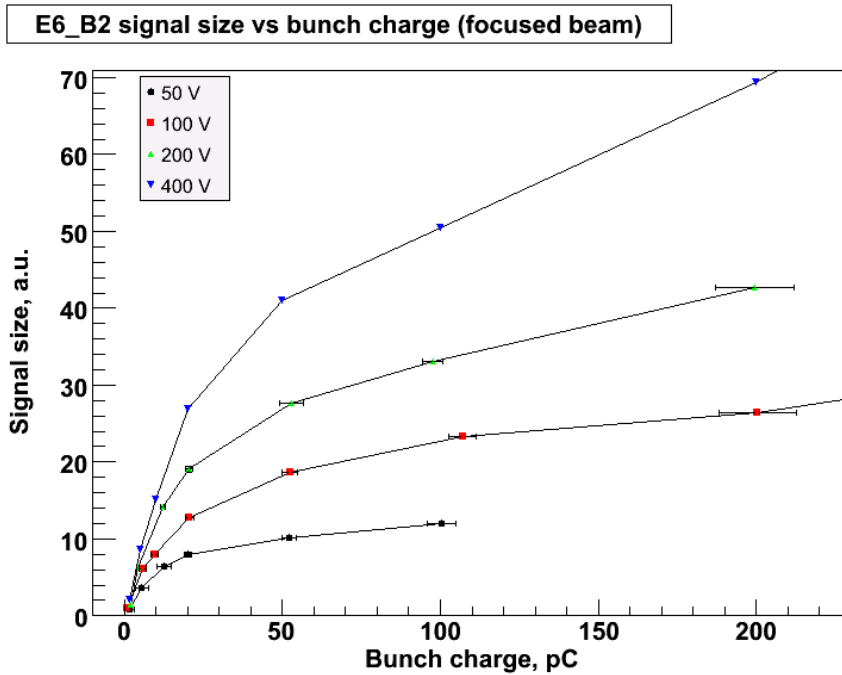


Figure 4.7.3.6: The dependence of the signal from the diamond sensor on the charge of the bunch hitting it for different values of bias voltage.

The charge released by ionization when a bunch of 1 pC crosses a 300 micron diamond sensor is about 11 nC. The signal size dependence on the bunch charge hitting the sensor

becomes non-linear for higher charges. This is determined, at least partially, due to insufficient amount of charge stored in the capacitor of the high voltage filter box. The non-linear behavior starts at higher bunch charges when the bias voltage rises and the capacitor stores higher charge. This is shown in Figure 4.7.3.6.

For the given sensor and the bias voltage and signal readout scheme, it was possible to distinguish the signal from noise down to the bunch charge of about 2 pC.

## 4.8. Sapphire sensors

Synthetic sapphire, chemical formula –  $\text{Al}_2\text{O}_3$ , is another promising sensor material. Its relevant properties are summarized in the Table 4.8.0.1. According to this, the sapphire sensors have even smaller leakage currents compared to diamond sensors under the same conditions. The signal for a MIP is 22 electron-hole pairs per micron of thickness, being only about 1.5 times smaller than that for diamond.

Synthetic sapphire is commercially available for a much lower price than CVD diamonds. The first few samples were bought from the CRYSTAL company [4.8.0.1] located close to DESY. These sapphires were proven to be operational as sensors with the CCE being much lower than that of the CVD diamond sensors. The impurity concentration in the material was on the level of a few tens of ppm, as summarized in Table 4.8.1.1 provided by the manufacturer. There are several manufacturers that supply sapphire material of high purity. It was suggested that relatively high impurity concentration could be the reason of low CCE values and more pure material could have larger CCE. The samples from two more manufacturers with different impurity concentrations - RSA Le Rubis [4.8.0.2] and Kyocera [4.8.0.3] have been characterized. The results are shown below.

Density, $\text{g}/\text{cm}^3$	3.98
Hardness, Mohs	9
Dielectric constant	11.5/9.3 (parallel/perpendicular to the C-axis)
Resistivity, $\Omega\cdot\text{cm}$	$\sim 10^{16}$
Breakdown field, $\text{V}/\mu\text{m}$	$\sim 10^6$
Thermal conductivity, $\text{W}/(\text{m}\cdot\text{K})$	46.06
Band gap, $E_g$ , eV	9.9
Ionization energy, $E_{\text{eh}}$ , eV	29.7
Mean energy loss (MIPs), $\text{MeV}/(\text{g}\cdot\text{cm}^2)$	1.65

Table 4.8.0.1: Properties of sapphire under normal conditions.

### 4.8.1. Material and metallization

Three methods of sapphire growth are used by the CRYSTAL company: Czochralski, Kyropoulos and Stepanov. The material grown by Czochralski method was used for my tests.

The principle of Czochralski method is sketched in Figure 4.8.1.1. The raw material is charged into a refractory crucible and is heated until it all melts down. Then a seed crystal shaped as a thin rod of a few mm in diameter is mounted onto a seed crystal holder and is dipped into the melt. All through the process the seed crystal holder is being cooled. The column of the melt which connects the grown crystal with the melt is maintained by surface tension force and this column forms a meniscus between the surface of the melt and the growing crystal. The solid-melt interface, or crystallization front, gets over the surfaces of the melt. The temperature of the melt and the conditions of the abstraction of heat from the seed crystal determine how high the crystallization front gets. When the end of the seed partially melts the seed is pulled out of the melt together with the crystallized material. At the same time the crystal is being rotated. It helps to keep the melt blended and to maintain the same temperature at the crystallization front. As a result of heat abstraction an oriented single crystal starts growing on the seed. The diameter of the crystal can be controlled by adjusting the speed of growth and the temperature of the melt.

The main advantages of pulling from the melt is that the crystal is grown in an open space, so the crystal does not come in contact with the crucible material, and it is easy to control the growing process and change the diameter of the crystal. A disadvantage consists in the difficulty to maintain chemical homogeneity of the crystal along the growth direction.

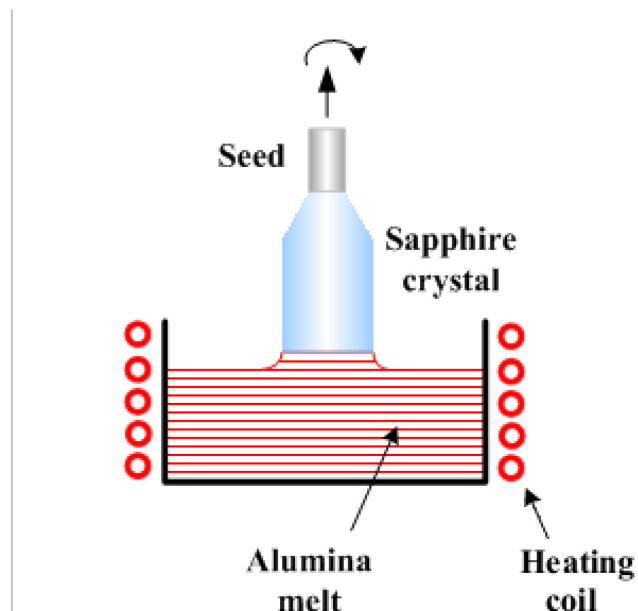


Figure 4.8.1.1: The scheme of the Czochralski method.

Impurity	Na	Si	Fe	Ca	Mg	Ni	Ti	Mn	Cu	Zr	Y
Concentration, ppm	8	2	5	5	1	<3	<1	3	<3	2	2

Table 4.8.1.1: Main impurities of the sapphires from the CRYSTAL company.

The total impurity concentration of the sapphires from the CRYSTAL company is on the level of few tens of ppm. The main impurities of the raw material and their concentrations are listed in the Table 4.8.1.1. The price per piece of about 1 cm<sup>2</sup> area and thickness of 300 micron is 15 euro.

The sapphires from the RSA Le Rubis are grown by Kyropoulos method as illustrated in Figure 4.8.1.2. The seed crystal is mounted onto a seed crystal holder cooled by water and the raw material melts in the crucible. Crystallization starts when the seed contacts the melt. The crystal grows into the melt forming a hemisphere or a cone. The crystal grows until its surface reaches the crucible walls. Then the crystal is pulled out (lifted) and the growing cycle repeats. There is also a version of the process with continuous pulling the crystal from the crucible. There are some modifications of this method, when the seed crystal holder rises continuously at a certain permanent speed.

The main advantage of Kyropoulos method is that the size of the grown crystal is limited only by the size of the crucible. Due to the low temperature gradient and natural cooling the crystal possesses very low dislocation density and is almost stress-free.

The guaranteed purity of the RSA Le Rubis sapphires is 99.996 %. The price for a piece of about 1 cm<sup>2</sup> area and thickness of 300 micron amounted to about 50 euro.

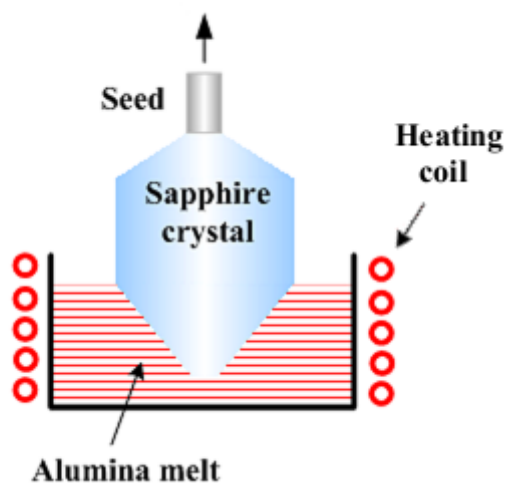


Figure 4.8.1.2: The scheme of the Kyropoulos method.

The sapphires from the Kyocera are grown by edge-defined film-fed growth (EFG) also known as Stepanov method. The principle of EFG method is schematically shown in Figure 4.8.1.3. The molten alumina is driven up to the crystallization front by the capillary forces within a die with thin channels (capillary die). The crystallization of the melt occurs on the top of the die (exit of the capillary channel) in an inert, e. g. argon, atmosphere. The crystal is continuously pulled out upwards.

The EFG method is used for growing sapphire of any given shape, including tubes, rods, sheets, and fibers. The EFG technology makes it possible to get unique shapes and sealed assemblies.

The guaranteed purity for the Kyocera sapphires is 99.994 %. The price for a piece of about 1 cm<sup>2</sup> area and thickness of 300 micron amounted to about 100 euro.

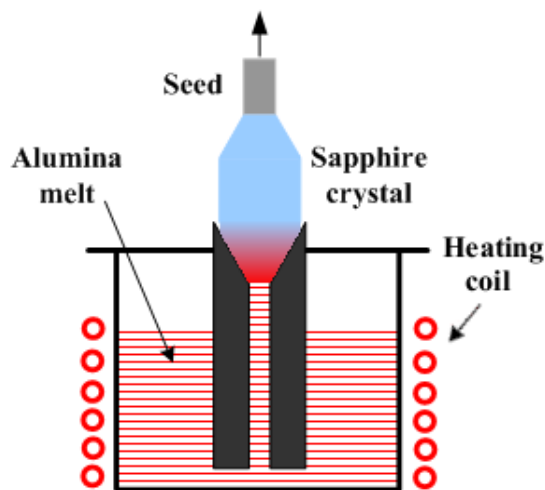


Figure 4.8.1.3: The scheme of the EFG method.

All investigated sensors were made of the plates measuring 10×10×0.5 mm<sup>3</sup> cut along the C-plane (0001) (see Figure 4.8.1.4). Two types of metallization were used: one squared 8×8 mm<sup>2</sup> pad on both sides, each consisting of either one Al layer 200 nm thick or three layers Al/Pt/Au, respectively 50/50/200 nm thick. Metallization for sapphire sensor was also formed in the Target Lab at GSI.

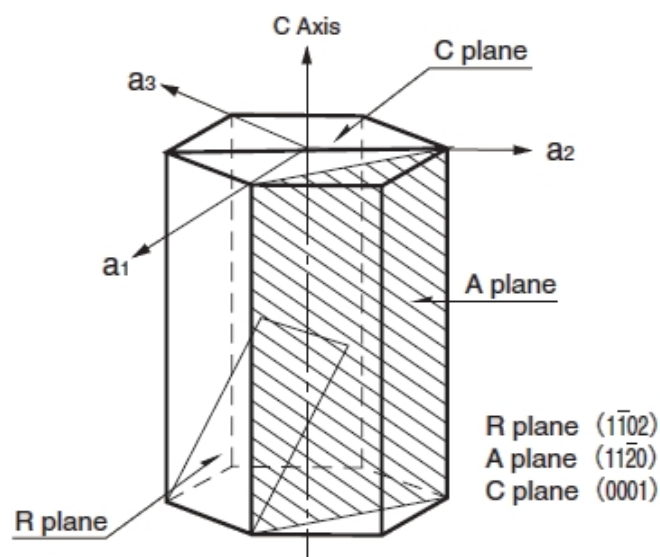


Figure 4.8.1.4: Typical orientations to cut the sapphire plates.

## 4.8.2 Characterization of sensors from different manufacturers

The first measurements were to ascertain whether or not the samples were usable as sensors [4.8.2.1]. The IV characteristics were measured with and without irradiation with a  $^{90}\text{Sr}$  source. Figure 4.8.2.1 shows the IV curves for three sapphire samples from the CRYSTAL company taken without and with irradiation. The leakage currents were within several pA up to applied voltage of 500 V. From the IV measurements with irradiation it should be noted that the signal currents for positive bias voltages were higher than that for negative bias for all three samples. If the sample was illuminated with UV light and the measurements were repeated for the reversed connection of the sample, the effect persisted. It is most probably due to irradiation during the measurement, i. e. pumping was present. The estimated values of CCE for the three CRYSTAL sensors in the unpumped state were 2-5 % for bias voltage of 500 V. The difference between the CCE in the unpumped and pumped states during the measurement was around 20 %.

A similar pumping effect was observed for the sapphires from RSA Le Rubis. The estimated CCE for the unpumped and pumped states at 500 V for 10 sapphires are listed in Table 4.8.2.1. The CCE values in the unpumped state are in the range 2 to 5 %. The difference between the pumped and the unpumped states was 50 – 100 %.

For the sapphire sensors from Kyocera no signal response due to irradiation with the source was observed.

### I-V characteristics

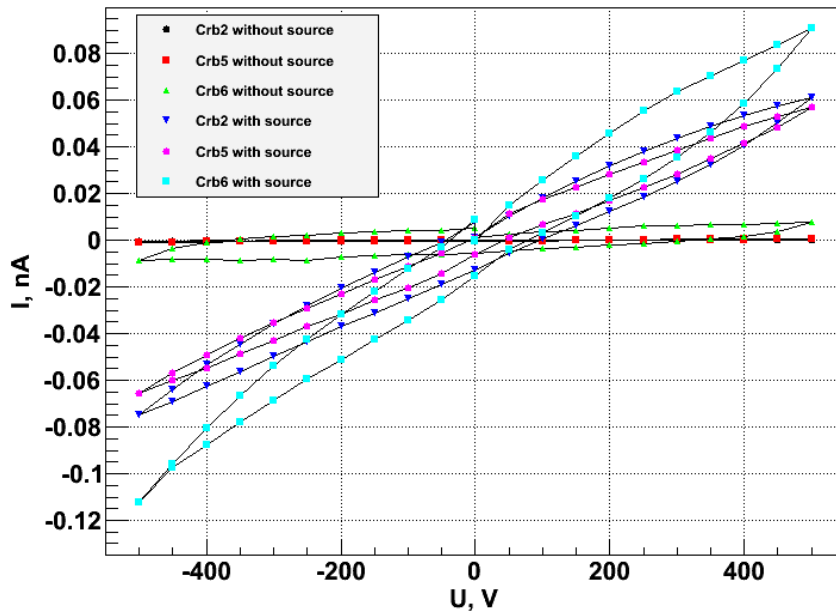


Figure 4.8.2.1: The I-V characteristics for 3 sapphire sensors under irradiation of a  $^{90}\text{Sr}$  source and without it.

Sample	CCE at 500 V, % Unpumped state	CCE at -500 V, % Pumped state
1	2.0	4.2
4	4.7	7.3
5	1.4	2.4
6	4.0	6.2
7	5.3	7.7
11	4.3	7.0
12	4.1	6.0
13	4.8	6.6
14	3.0	6.0

Table 4.8.2.1: CCE of the sapphire sensors from RSA Le Rubis.

Radiation tolerance for two CRYSTAL sapphire sensors has been investigated with a 8.5 MeV electron beam. The relative CCE as a function of the absorbed dose for them is

presented in Figure 4.8.2.2. For both sensors the CCE drops with the absorbed dose. The measurements show compatible results. The CCE of the sensor after absorption of 12 MGy amounted to 30 % of its initial value. The peaks on the rather smooth curves are due to an increased CCE after the periods when the beam was switched off. When the beam was switched back on, a larger CCE was observed for a short time.

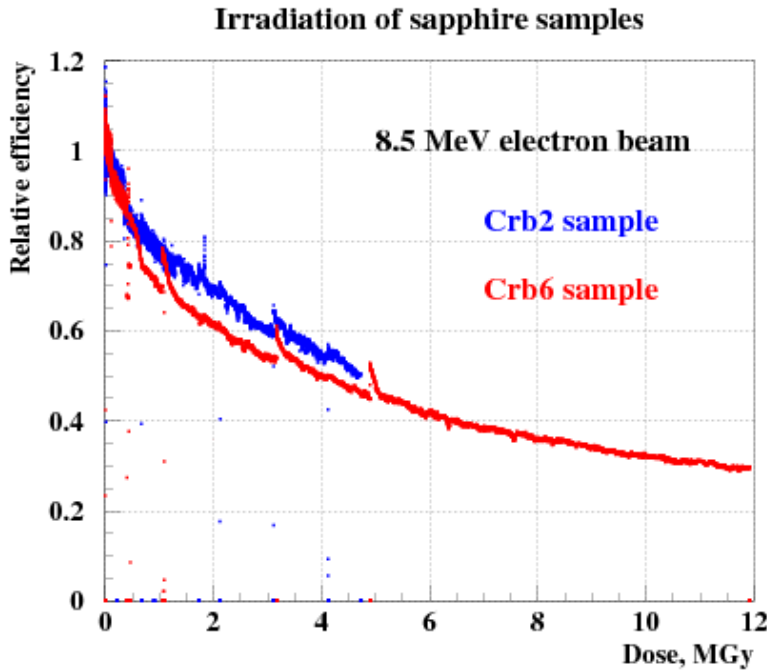


Figure 4.8.2.2: The relative CCE for two CRYSTAL sapphire sensors as a function of the absorbed dose.

There was no significant leakage current rise observed for the sapphire sensors after irradiation.

### 4.8.3 Prototype of the sapphire beam condition monitor

In order to enhance the performance of sapphire sensors with a relatively low CCE for single particle detection, a detector concept for beam loss and conditions monitoring made of an assembly of sapphires was proposed [4.8.3.1]. The detector consists of 8 individual sapphires of usual dimensions and Al/Pt/Au metallization with 4 readout channels (see Figure 4.8.3.1). The metal contacts have the area of  $9 \times 9 \text{ mm}^2$  from one side and  $9 \times 7 \text{ mm}^2$  from the other. The total sensitive area was  $7 \times 4 \text{ mm}^2$  (the height of the assembly – 4 mm).



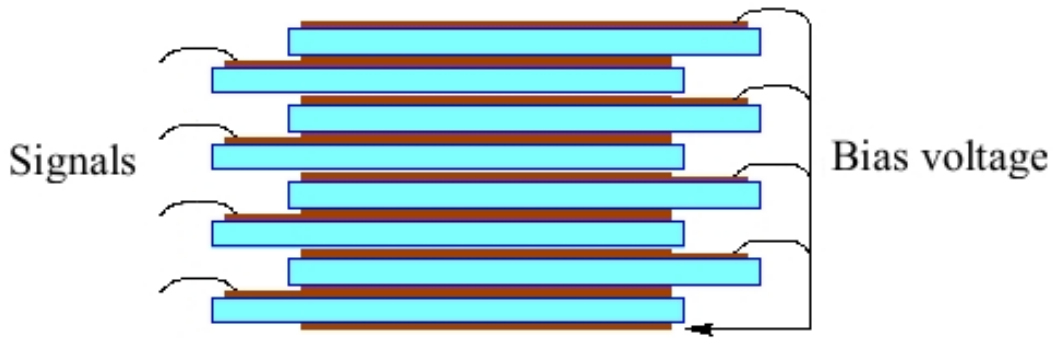


Figure 4.8.3.1: Schematic view of the detector assembly made of an assembly of sapphires.

The first experiment to prove the principle of operation has been conducted at DESY accelerator [4.8.3.2] with 5 GeV electrons. Single electrons were hitting the sensitive area of the detector and causing ionization along 10 mm of the detector width. Charge collection occurs along an individual sensor width as shown in Figure 4.8.3.2 b. As a result, the signal is enhanced compared to the case, when both ionization and charge collection occurs along the sensor thickness.

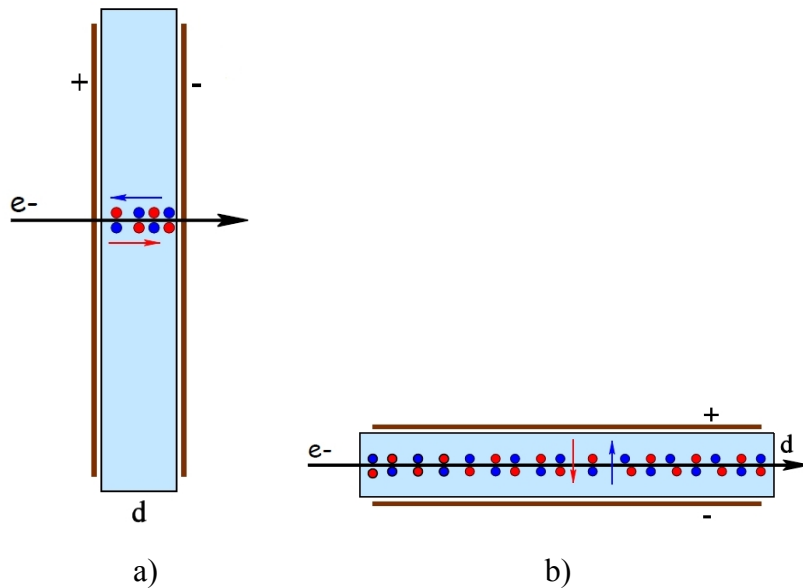


Figure 4.8.3.2: Illustration of the sensor orientation: a) typical orientation, b) orientation for signal enhancement.

As it was expected, the MIP signal from the sapphire sensor as a response to a single 5 GeV electron was 12000 electrons, which is comparable with the signal of the best sensors of CVD diamonds of 300  $\mu\text{m}$  thickness. In the future the sapphire sensor can be a good alternative to CVD diamonds in the applications for beam condition and beam halo monitors.

# Chapter 5

## Beam Halo Monitor at FLASH

In the year 2008 the beam pipe in the dump line was damaged by unrecognized beam loss during FLASH operation. A vacuum leak occurred near the dump vacuum window. The existing beam dump diagnostics was not sufficient to prevent the damage. The need for a fast reliable diagnostic system operating in conjunction with already existing dump diagnostics became obvious. The concept of the BHM based on synthetic diamond and sapphire sensors has been then introduced for the first time. The BHM has been installed during the upgrade in 2009 as a part of the new dump diagnostics. In this chapter the FLASH dump line is described, commissioning of the BHM and experience of operation as well as the calibration procedure are reported. In the end the characteristics of the BHM installed at FLASH2 are discussed.

### **5.1 FLASH beam dump line**

The FLASH beam dump line is purposed to safely deliver all electrons passed through the undulator section to the dump in order to stop them. The position of the beam dump in FLASH is marked in Figure 5.1.1. A dipole magnet deflects the electrons passed through undulators 17.5 degrees downwards. A steerer magnet allows correcting the trajectory in the horizontal plane. Two quadruple magnets defocus the beam in order to widen the beam spot on the exit window of the beam pipe and the dump. A sextuple magnet, the so-called sweeper or rotator, rotates the beam in the plane perpendicular to the beam direction to distribute the power over a larger area. It becomes useful with long trains of 30 and more bunches. Normally the sweeping radius lies within 10 mm. Safe operation in the dump region is supported by several diagnostic tools.

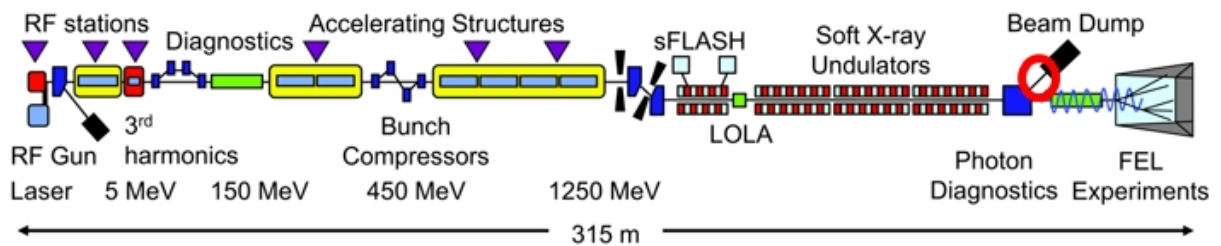


Figure 5.1.1: Schematic view of FLASH after upgrade in 2009. The beam dump line position is marked by the red circle.

The elements of the beam dump diagnostics before the year 2008 are shown in Figure 5.1.2. A toroid measured the bunch charge delivered to the dump. An OTR screen measured the transverse profile of the beam deflected to the dump section for only a few bunches in a train. Two BPMs, a stripline BPM and a button BPM, defined the center of charge of a bunch and assisted to correct the beam trajectory. Three short scintillator BLMs in front of the concrete shielding, hiding the last section of the dump line approximately 3.2 m long, delivered alarms when the losses are above a certain level.

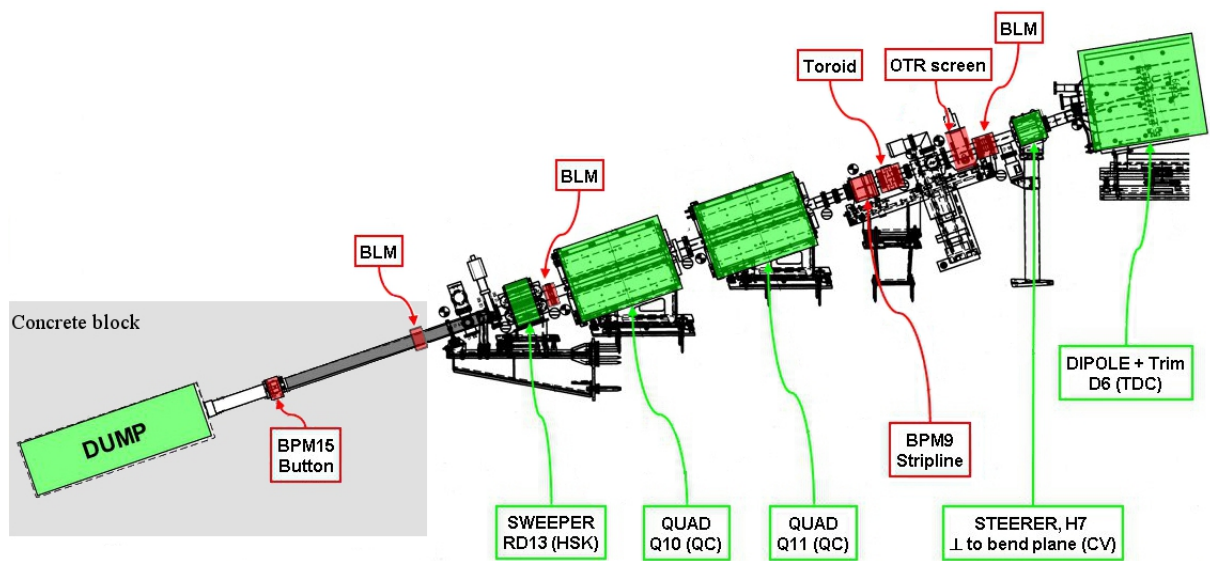


Figure 5.1.2: FLASH beam dump line in 2008.

From all mentioned above diagnostics tools there was only one BPM positioned close to the vacuum window, that was not robust enough for the given radiation level. Such scheme turned out to be insufficient for preventing dangerous conditions. The location of the BLMs leaving a long section of the beam pipe not covered allowed a substantial angular miss-steering of the beam. As a consequence, the damage of the beam pipe with the following vacuum leak occurred during an experiment with long bunch trains, high bunch charges and high repetition rates [5.1.1]. Therefore, a new concept for the beam dump diagnostics has been developed.

New components have been installed, mainly in the last section, during the upgrade in 2009 and have been commissioned successfully afterwards. These components intend to better define the electron path there. The status of the diagnostics after the upgrade is depicted in Figure 5.1.3.

Several new components supplemented the dump diagnostics. An additional button BPM module was placed between the quadrupole magnets. The previously installed button BPM has been replaced by a magnetic-coupled BPM [5.1.2], positioned in the gap between the vacuum window and the dump itself. A BHM, developed by the author of the thesis, has been installed in the gap. Four long ionization chambers and four long scintillator BLMs positioned azimuthally around the beam pipe now cover almost the full length of the section. Simultaneous operation of all the above mentioned systems ensures high level of redundancy. More than one system can signal upon dangerous conditions at the same time and failure one of them is not crucial.

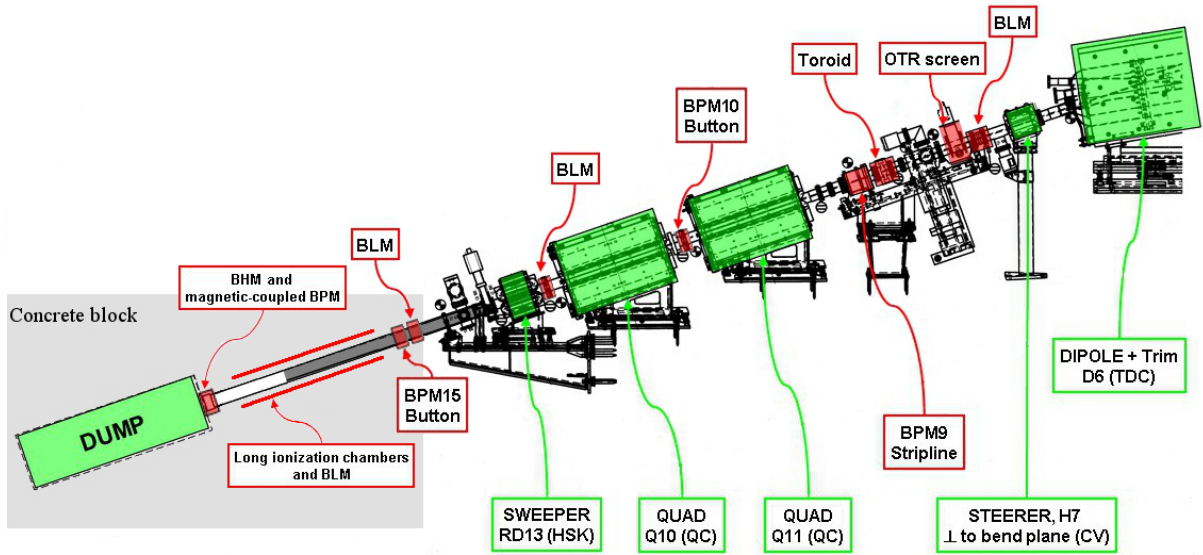


Figure 5.1.3: The last section of the beam dump line after FLASH upgrade in 2009.

## 5.2 BHM description

The BHM module is positioned in the end of the beam pipe behind the vacuum window directly in front of the dump. Four  $300\ \mu\text{m}$  thick pCVD diamond sensors with the area of  $12 \times 12\ \text{mm}^2$  and four  $500\ \mu\text{m}$  thick synthetic monocrystalline sapphires with the area of  $10 \times 10\ \text{mm}^2$  are placed alternately and uniformly distributed in azimuthal direction inside cups as shown in Figure 5.2.1. Both sides of the sensors were covered with metallization, one pad from each side. The metallization consists of 3 layers Ti/Pt/Au of the thickness 50/50/200 nm, respectively, for diamonds and Al/Ti/Au of the thickness 50/50/200 nm, respectively, for sapphires.

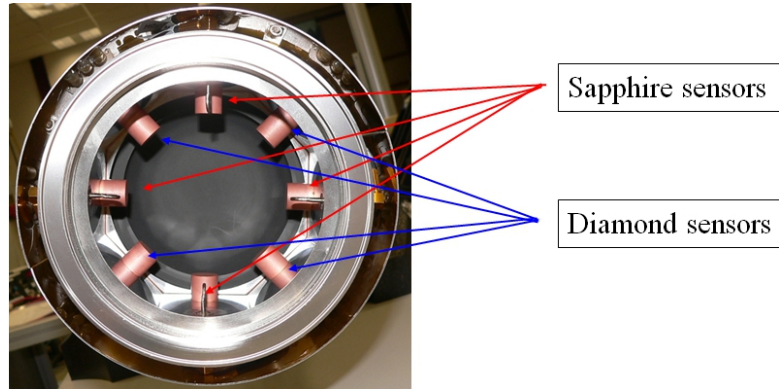


Figure 5.2.1: View to the BHM module from the dump. The pick-ups of the magnetic-coupled BPM can be seen in front of the cups with sapphire sensors.

The sensors are operated as solid state ionization chambers. The bias voltage supply and signal readout scheme for each sensor is shown in Figure 5.2.2. Three coaxial cables per sensor channel are used, two of them to provide bias voltage and one to readout the signal. The sensors are connected to a HV filter box with 4 meter long radiation hard GX 03272 D-06 cables. The HV filter purposes to suppress bias voltage pulsation, to protect the signal circuitry in case of the sensor failure and to store enough charge for large signal pulses. Coaxial cables of approx. 60 meter connect the filter box to the counting room which houses the readout electronics. The signals, integrated and limited by amplitude, are routed to a fast direct conversion 14-bit ADC [5.2.1] with 8 channels. Integration of the raw signal is required in order to match the specification of the ADC. The time constant for the integrated signal must be kept such that the signal width is within the inter-bunch pattern at 1 MHz repetition rate of the machine. The signals must be limited by the amplitude to the ADC input range. The ADC uses 1 MHz clock which is aligned with the maximum of the BHM sensors' signals. Its input resistance is set to 10 k $\Omega$ .

Figure 5.2.3 shows the CCE as a function of bias voltage for all 4 BHM diamond sensors. The CCE values are about the same for all diamond sensors. The leakage currents measured to be within few to several nA for bias voltages up to 500 V. No erratic currents were observed during the IV measurements.

The CCEs of the BHM sapphire sensors were estimated to be in the range of 3-5 % at bias voltage of 500 V. The leakage currents were within 1 pA for bias voltages up to 500 V. No erratic currents were observed during the IV measurements.

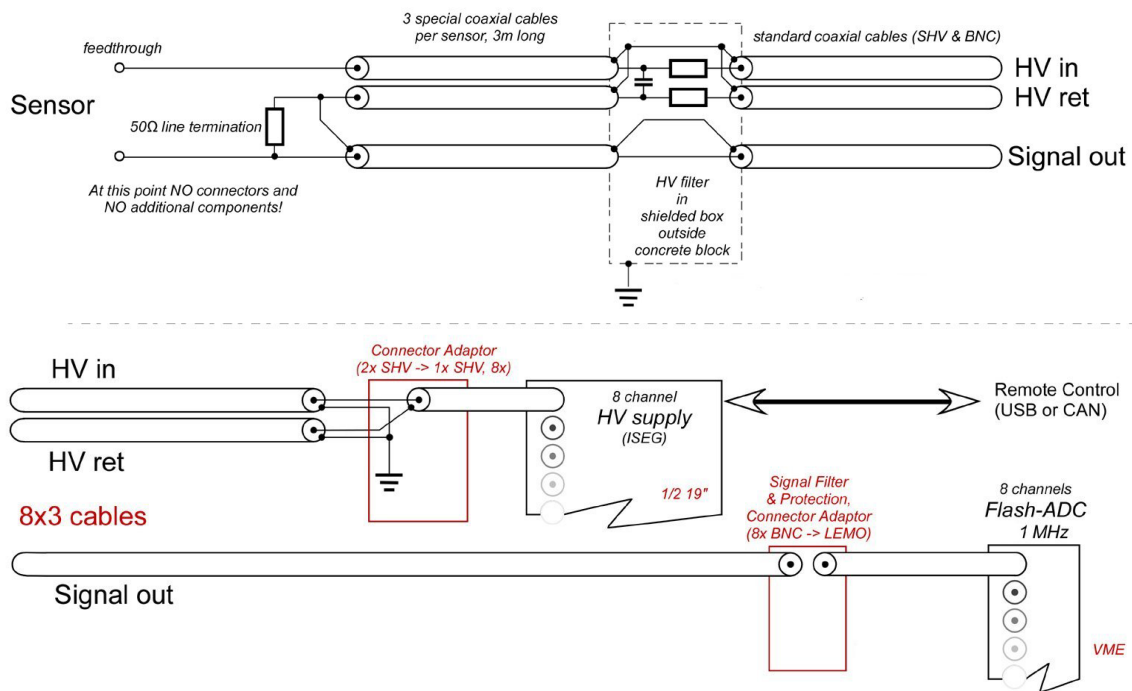


Figure 5.2.2: Bias voltage and signal readout scheme for each BHM sensor.

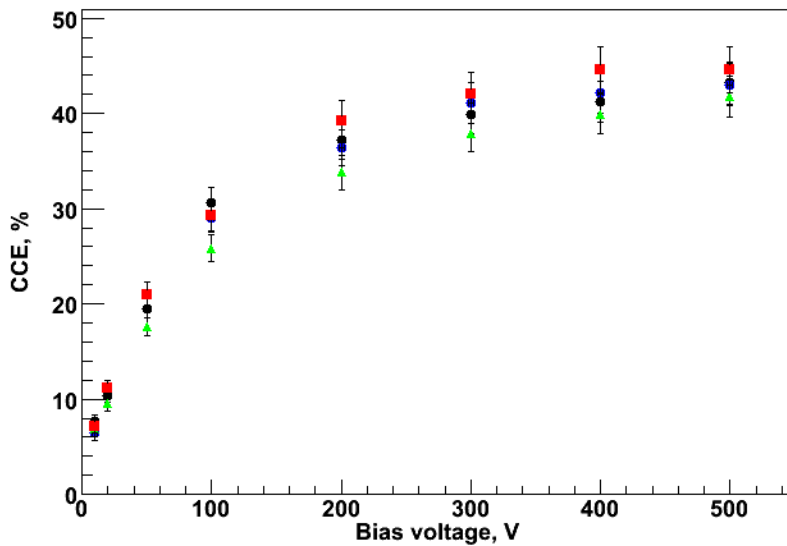


Figure 5.2.3: The CCE as a function of applied voltage for four diamond sensors for the BHM at FLASH. The points are measured in 10 min after the bias voltage was applied.

### 5.3 Commissioning and first tests

Commissioning of the BHM has been performed in September 2009 during the so-called “9 mA” experiment – a test aiming to run long trains of 800  $\mu\text{s}$  with bunch repetition rate of 3 MHz and bunch charge of 3 nC [5.3.1].

The first step was to observe signals from all the sensors in the presence of the beam. After elimination of a problem with the connector in one of the channels, all signals were observed. The signals in diamond channels were above the noise level whenever the beam was present and the bunch charges were above a few tens of pC. The signals in sapphire channels were observed at high bunch charges or when the beam was steered in the plane perpendicular towards the corresponding sensors. Raw signals from both types of sensors at the end of the long cables on the input of the signal filter and limitation box have FWHM of 10 ns, as can be seen in Figure 5.3.1 a. The box integrates the signals and limits their amplitudes to match the requirements of the ADC. The output impedance of the box is tuned to the input impedance of the ADC. The signal loaded to a high impedance of an oscilloscope is shown in Figure 5.3.1 b. The disturbance of the waveform is due to a 2 meter long 50  $\Omega$  coaxial cable connecting the filter box and the input of the ADC. Later on that has been corrected with an improved design of the filter box capable to operate with a load of 50  $\Omega$ . The timing for the ADC clock is adjusted in such a way that the ADC captures the maximal value of the signal. In this way digital signals appear as a single value once per bunch with repetition rate up to 1 MHz. Figure 5.3.2 shows the digitized signals from a BMH sensor as a response to 30 bunches.

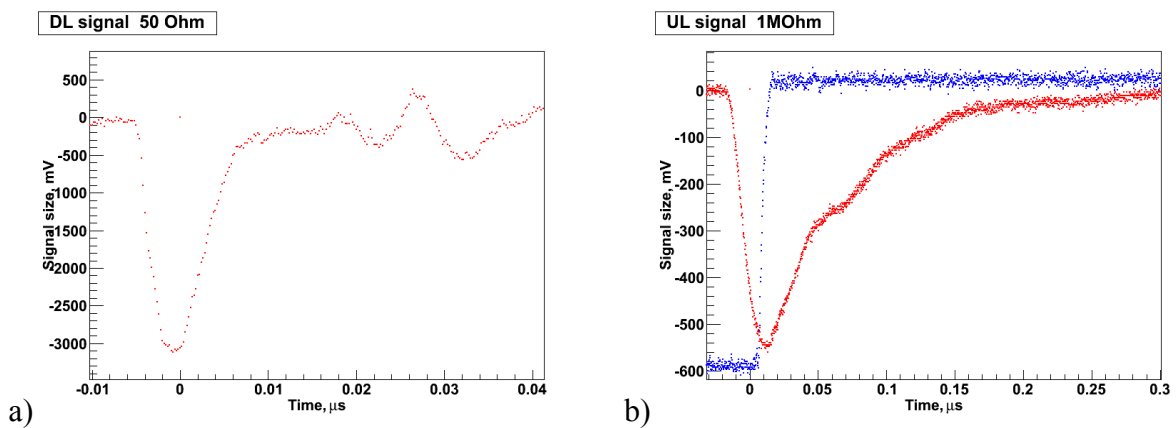


Figure 5.3.1: Signal from a BHM sensor (red): a) “raw” signal before the signal filter and protection box; b) signal on the output of the box, red waveform. The ADC clock adjusted to the maximum of amplitude is shown in blue on the right plot.

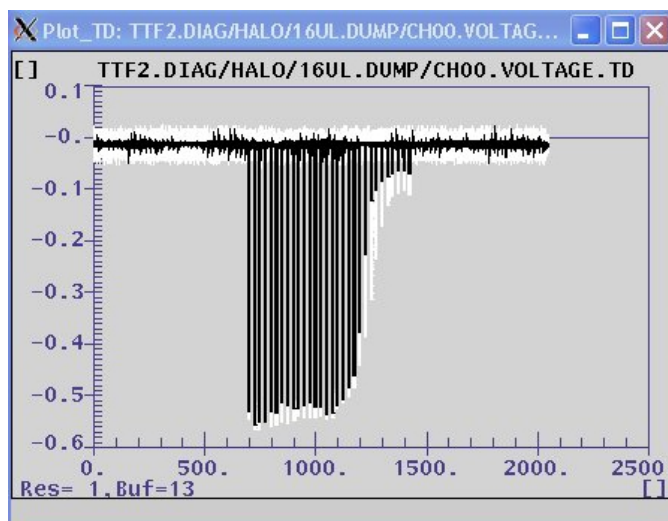


Figure 5.3.2: Digital signal from a BHM sensor as a response to 30 bunches. Vertical scale is in V, horizontal scale is in  $\mu\text{s}$ .

The BHM sensors are also sensitive to the dark current in the machine. When the constituent particles of the dark current reach the sensors simultaneously with the halo particles accompanying the beam, the signals in the sensors have contribution from both dark current and halo particles. The contribution from the dark current can be distinguished in case of long trains with either some empty bunches or/and with bunch repetition rate smaller than the ADC clock of 1 MHz. Figure 5.3.3 a shows an example of the digitized signals from a diamond sensor in case of long train with empty bunches and bunch repetition rate of 50 kHz. The timing for all digital signal plots is such that the first bunch of a train appears at 700  $\mu\text{s}$ . The contribution from the dark current is clearly seen for the empty bunches between and after the two filled bunches. The signal from the filled bunches contains also a contribution from the halo particles. The signals from a sapphire sensor in case of a long train with bunch repetition rate of 500 kHz are shown in Figure 5.3.3 b. The signals from a single bunch are not seen. Due to the fact that each second reading of the ADC corresponds to the non-filled bunch, the signals corresponding to the filled bunches appear in the figure on the top of contribution due to the dark current. This offset is the measure of the dark current contribution to the BHM signal.



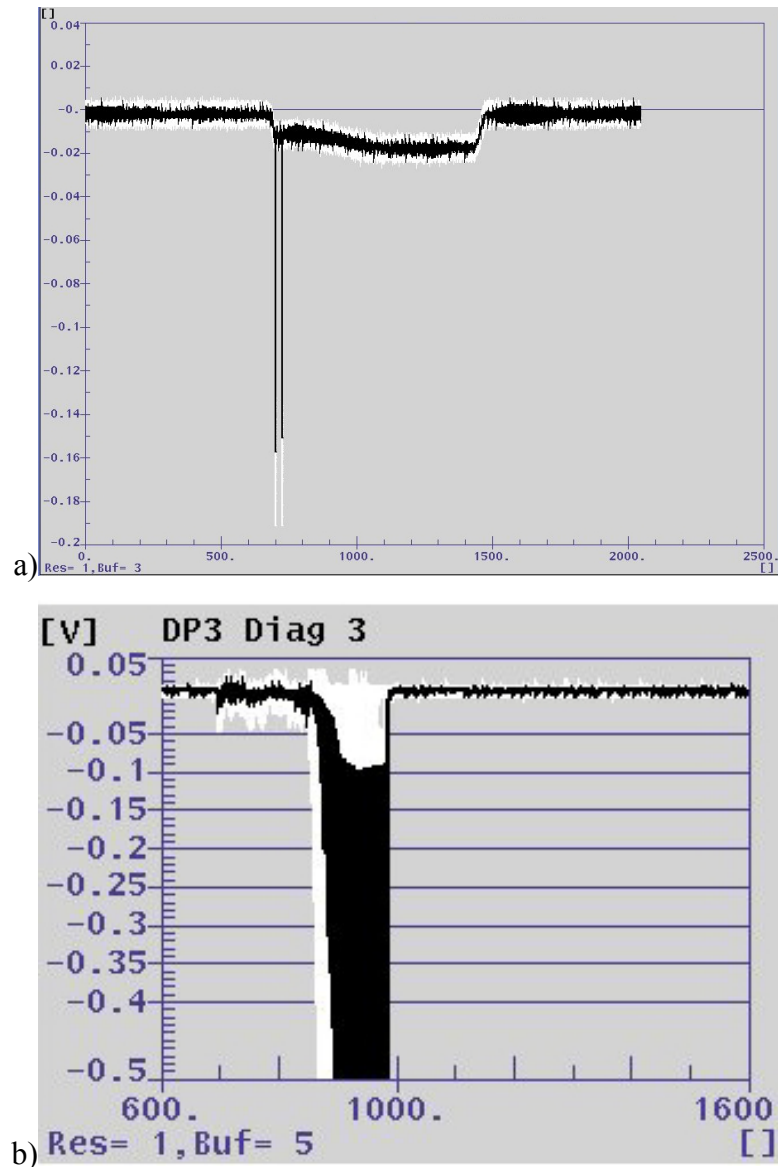


Figure 5.3.3: Signals from BHM sensors in case of high dark current in the machine: a) from a diamond sensor, b) from a sapphire sensor.

Another way to prove the functionality of the BHM was to investigate how the signal of each sensor depends on the beam position. A signal raise while the beam approaches a certain sensor indicates the correct operation, since the beam halo in the sensor's position becomes more intense. For this purpose a number of tests have been carried out. The results of one are shown in Figure 5.3.4. It displays the average response from all 8 BHM sensors normalized to the bunch charge delivered to the dump as a function of beam position. The measurement includes two periods of a few minutes of multi-bunch operation each with slightly different beam positions and sweeper magnet turned on. This is schematically shown in the center of the figure. All four diamond sensors and the two closest sapphire sensors show the significantly higher signals when the beam gets closer. The average response is defined as:

$$U_i^{av} = \frac{1}{n_i} \sum_{j=1}^{n_i} \frac{U_{i,j}}{Q_j}, \quad (5.3.1)$$

where  $U_i^{av}$  is an average signal of a sensor for the beam in the  $i^{\text{th}}$  position,  $U_{i,j}$  – sensor response to the  $j^{\text{th}}$  bunch of the beam in the  $i^{\text{th}}$  position (the bunch numbering is continuous over the entire measurement period),  $n_i$  – number of bunches detected in the  $i^{\text{th}}$  position,  $j$  – the index of the number of bunch in the position,  $Q_j$  – delivered to the bump charge of the  $j^{\text{th}}$  bunch.

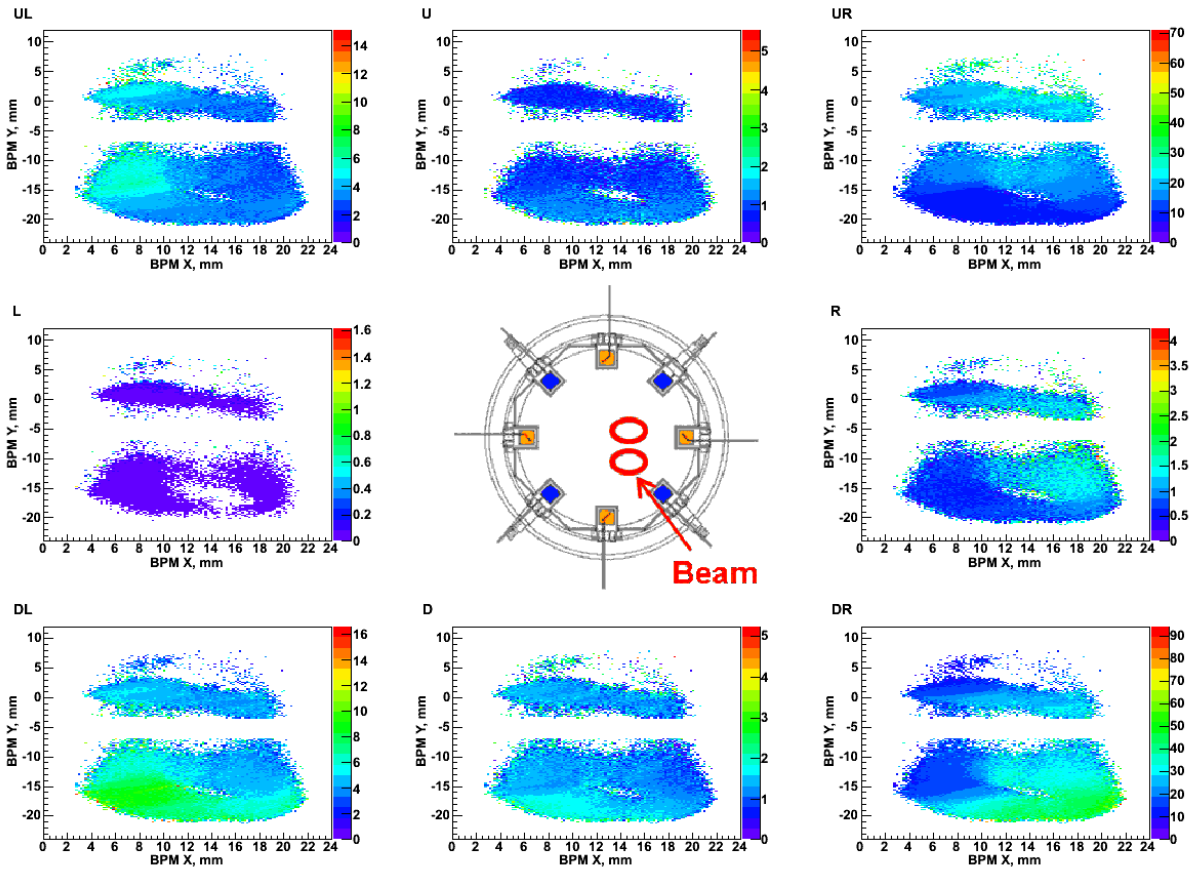


Figure 5.3.4: Average signals from all the BHM sensors normalized to the bunch charge delivered to the dump (color-coded, in mV per nC) as a function of the beam position during multi-bunch operation. Two periods with slightly different beam positions (considering sweeping) are shown. The beam is swept beam in the sensor along the red ovals, as schematically shown in the center of the figure.

The following test aimed to check correlations between the BHM signal and sweeping. The beam was centered in the last section of the beam pipe with normal sweeping on. The signals from the BHM sensors were recorded within a few minutes. The average signal defined according to the Eq. 5.3.1 as a function of beam position for a diamond and a sapphire sensors

is depicted in Figure 5.3.5. Even with the sweeping set to a relatively small radius the variation of the signal from the diamond sensor is noticeable. As it was expected the signal maximum corresponds to the beam position closest to the sensor. The situation with the sapphire is different. Signal variation here is hard to detect. Although, if the signals from these two sensors are considered in the frequency domain applying fast Fourier transform to the signals in the time domain, the sweeping frequency of 1.1 Hz can be clearly seen for both the diamond and the sapphire sensors (Figure 5.3.6).

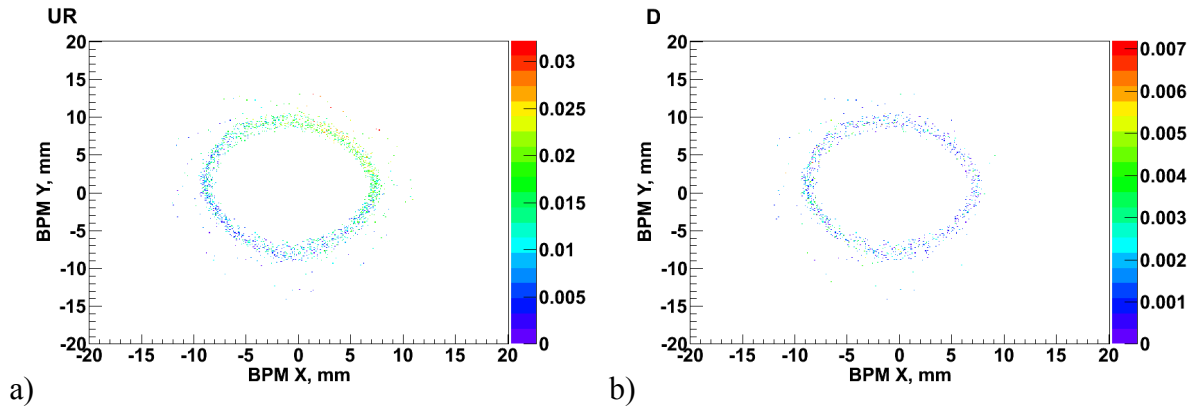


Figure 5.3.5: Signal from a diamond (a) and a sapphire (b) sensors as a function of beam position. The beam is centered, normal sweeping. The color code is in volts.

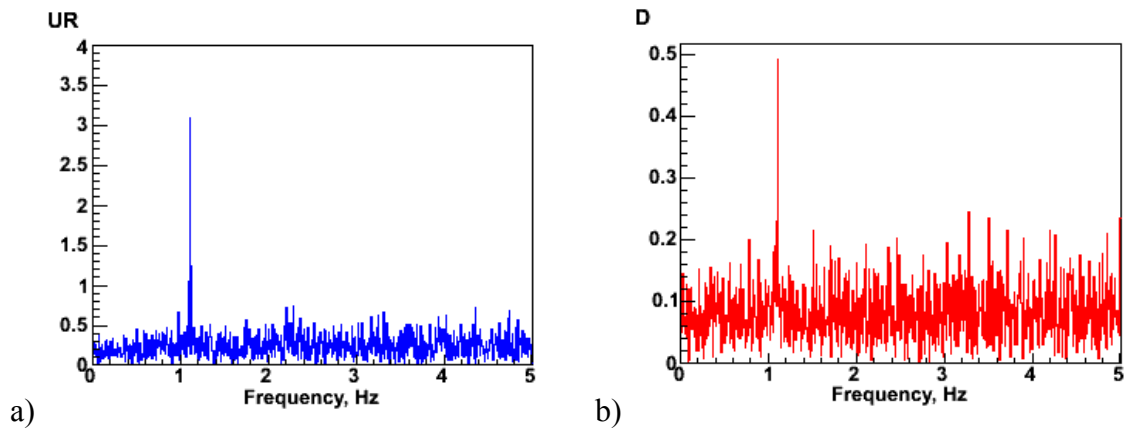


Figure 5.3.6: Results of the fast Fourier transform for the sets of the BHM signals represented in Figure 5.3.5. The sweeping frequency of 1.1 Hz can be seen for both the diamond and the sapphire sensors.

The tests described above have proven that the BHM was operational. The next step was to perform a calibration, i.e. to make correspondence between the signal from the sensors and the charge of halo particles crossing them. The BHM calibration procedure at FLASH is described below.

## 5.4 Calibration

Before describing the calibration procedure let us consider the important aspects for the matter. The energy distribution for the halo particles is not known for the real accelerator. The halo particles accompanying the beam have to have small energy difference to the beam core. Dark current can contain particles of lower energies. However, the energy difference for the dark current transmitted to the dump is limited by the energy acceptance of the collimator. Moreover, the contribution of the dark current to the total signal is relatively small as demonstrated in section 5.3. There is not enough material on the way of the particles hitting the BHM sensors for electromagnetic shower to develop as the sensors are positioned inside the beam pipe. The thickness of the sensor cups is rather small for shower to develop and big enough to significantly reduce the number of particles with low energies: coming both in forward and backward directions [5.4.1]. Taking into account all the above mentioned, it can be assumed that during the calibration rather monoenergetic primary particles are registered. Therefore, it is reasonable to perform calibration by shooting the beam of a certain energy directly to the sensors and measuring the response. The calibration factor for different energies can be obtained by repeating the procedure with the beam of required energy or by correction of the existing calibration with the factor that depends on energy deposition in the sensor material. As it has been shown in Chapter 4, the energy deposition varies with the energy of incident particles.

The calibration procedure of the BHM at FLASH for one value of the beam energy has been conducted as follows. The quadruple magnets were cycled to minimize the remanent field to keep the beam spot roughly of the same size as the sensitive area of the BHM sensors. With the sweeping switched off the beam was centered in the dump line using all BPMs. Then the power of the laser in the gun was adjusted such that the required bunch charge was measured with the toroid system in the dump. The OTR screen of the dump line was used into the beam pipe in order to observe the transverse beam profile and correct its shape, if it was stretched. The observation of the beam profile with the screen is possible in single-bunch mode for a bunch with a minimal charge of around 100 pC. For smaller bunch charges the shape was corrected at 100 pC and then the bunch charge was lowered. The toroid in the dump area is capable to measure bunch charge down to 40 pC, which was used as the first calibration point. At each point the sweeping was switched on and set to a radius of around 55 mm – the distance from the center of the beam to the center of a sensor. Thus, the sweeping beam hit each sensor in turns. The relation between the control current (in ampere) for the sweeper magnet with the sweeping radius on the front of the dump (in cm) for electrons with a momentum  $P$  in GeV is:

$$I = 17.8(A) \cdot \frac{R_{sweep}}{2} \cdot P. \quad (5.4.1)$$

A scan around the value given by the formula 5.4.1 to reach maximal values of the signals from the BHM sensors was performed for a few different bunch charges. The current corresponding to a sweeping, when the maximal signals were observed was used for calibration. The signals for all BHM sensors were recorded for a few minutes at each point. For

each period the average signal was calculated in similar way as it was described in previous subchapter using Eq. 5.3.1, but in this case not normalized to the bunch charge. The energy of the beam was set to 943 MeV, which was close to the maximum energy at FLASH at that time, in order to minimize the probability of multiple scattering in the material of the sensor cups.

Figure 5.4.1 shows the average signals for all sensors as a function of the magnetic-coupled BPM reading. One can see that at such large sweeping radii the magnetic-coupled BPM goes into saturation and the sweeping does not appear as a circle. Using formula 5.4.1, it is easy to calculate the actual radius and to reconstruct the sweeping amplitude as shown in Figure 5.4.2.

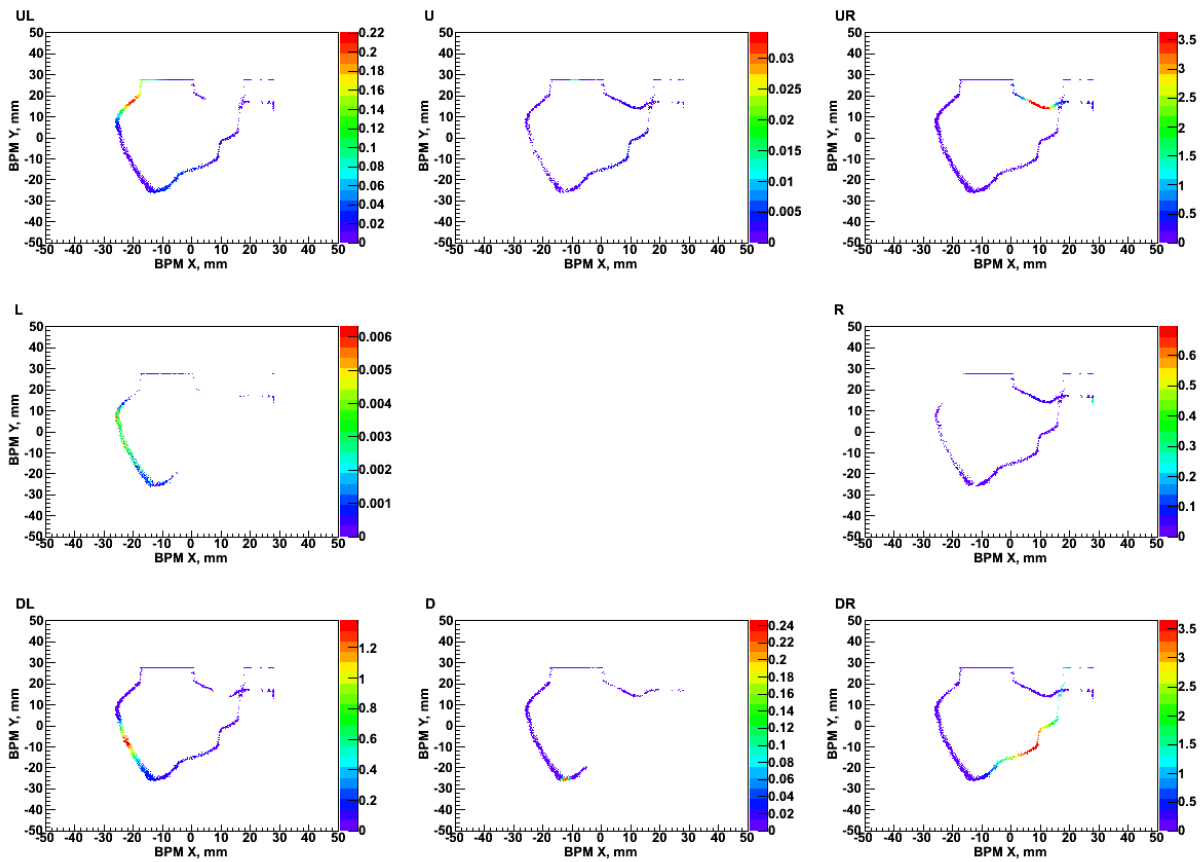


Figure 5.4.1: Average signals from all the BHM sensors as a function of the beam position measured by magnetic-coupled BPM. At large sweeping radii the BPM readings are saturated.

The average signals from all sensors take maximal values in the beam positions approximately corresponding to the position of the sensors. Small differences are due to imperfections with the reconstruction. The maximal values for all diamonds, correspondingly all sapphires, appear to be different, although the charge collection efficiencies for all diamonds were measured to be almost the same. For the sapphire sensors such measurements could not be done. The CCEs were estimated to be similar for all four sapphire sensors using the procedure explained in section 4.6.2. Therefore, under the same conditions the signals from

all sensors of the same kind should be nearly equal. The most probable explanation for the observed differences is that the beam centering or the beam shape was not perfect. Let us then consider the average signals from 2 diamonds and 1 sapphire with the maximal signals and assume that the calibration conditions were better suited for them.

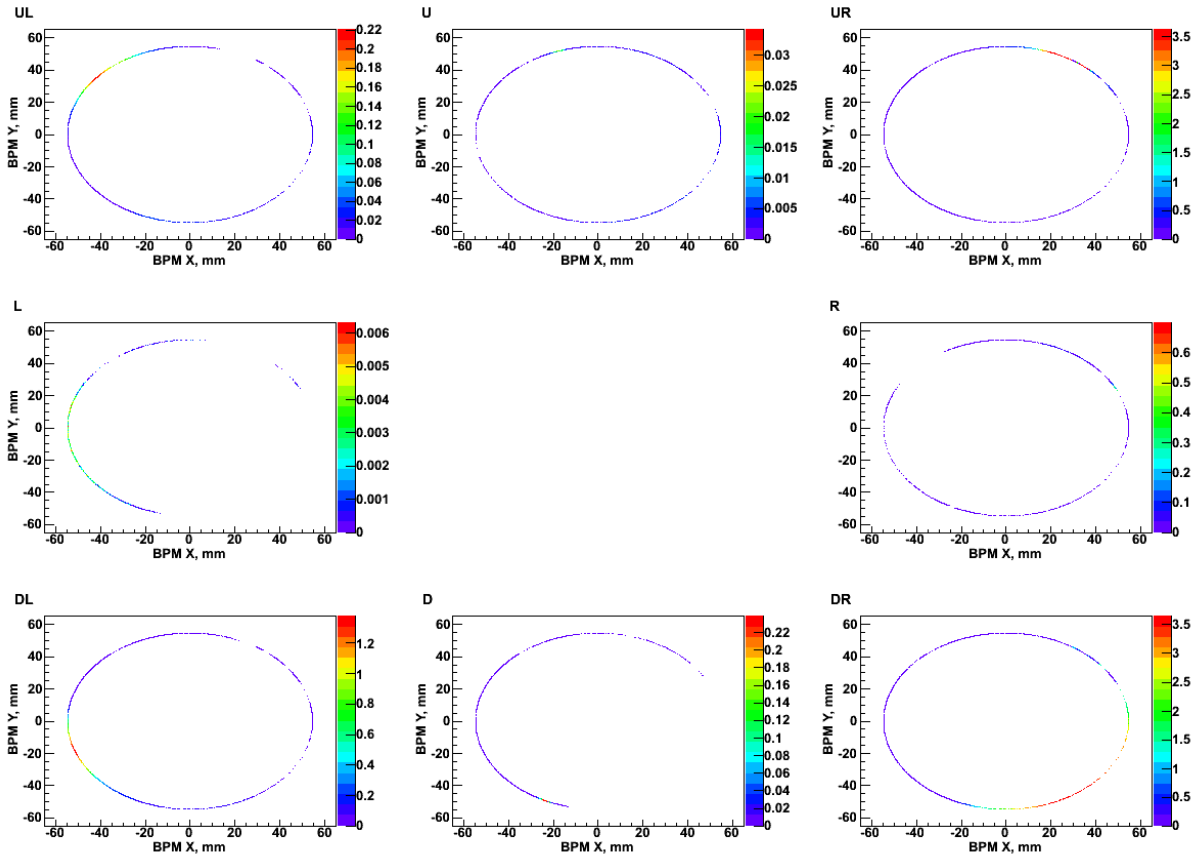


Figure 5.4.2: The average BHM signals shown in Figure 5.4.1 as a function of reconstructed beam position.

Figure 5.4.3 shows the maximal average signals for 2 diamond and 1 sapphire sensors for different bunch charges of the beam hitting the sensors. For some values of the bunch charge there were two periods of measurements and two points corresponding to the same value of the bunch charge are in the plot. For fitting only larger values were taken, the rest was omitted. Also the values lower than or almost equal to these values corresponding to smaller bunch charges were not considered for the fit. These are the signals from the sapphire at 150 pC, 400 pC and 500 pC. The minimal value of the bunch charge for the measurements was 40 pC as it was the smallest value that can be properly measured by the toroid system. As it was mentioned in chapter 4 the diamonds sensors are able to respond to a charge of 2 pC hitting the sensor.

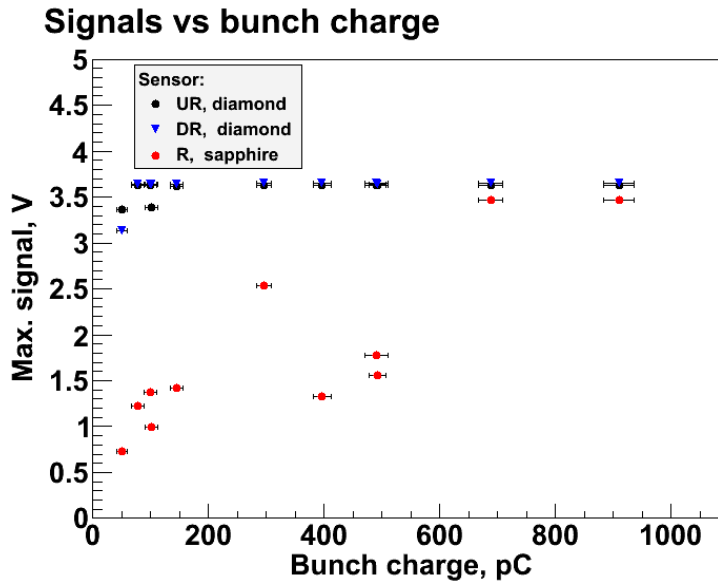


Figure 5.4.3: Maximal average signals from 2 diamond and 1 sapphire sensors for different bunch charges delivered to the dump. For some bunch charges two measurement periods are shown.

An alternative method of data representation during calibration was used to cross-check the dependence of the BHM sensors' signals on the bunch charge: the complete set of signal values taken during the measurement was plotted for each value of the bunch charge (Figure 5.4.4). If now again the values lower than or almost equal to that corresponding to smaller bunch charges are excluded from consideration, the dependence of the maximal signals from the diamonds and the sapphire is the same as the one for maximal average signals in Figure 5.4.3.

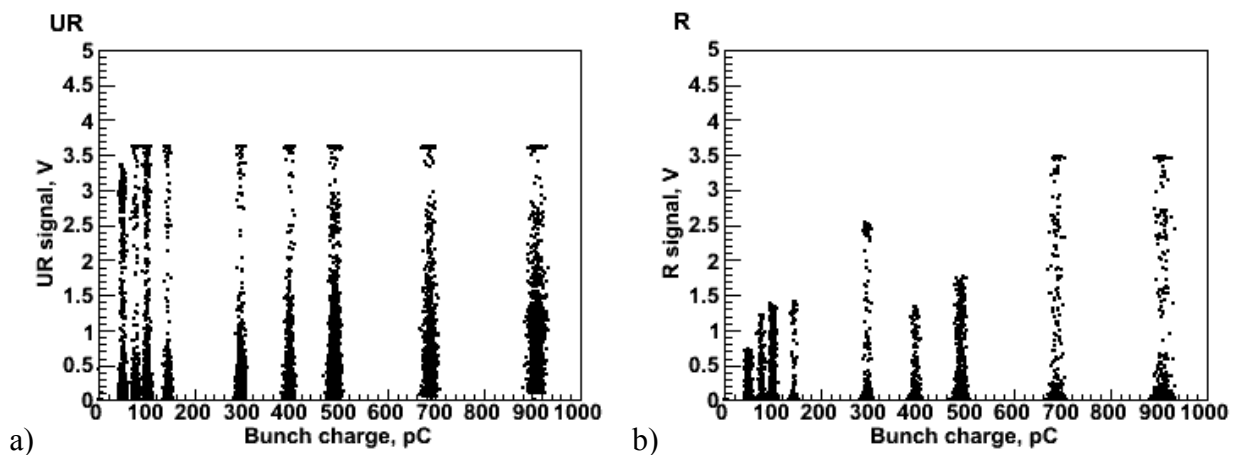


Figure 5.4.4: Complete sets of values during the measurement periods for different bunch charges for a diamond (a) and a sapphire (b).

There are three different regions for the response of a diamond sensor. For low bunch charges of incident particles the signal depends on this charge linearly. For medium charges it becomes nonlinear and goes into saturation at high charges. Therefore, the data for the diamond have been fitted accordingly. For medium charges it was found that fitting the nonlinear range with a polynomial of degree 3 gives good results. The other 2 ranges were fitted with linear function. The same fitting functions are also applied to the signals from the sapphires. This fits were applied to the data points shown in Figure 5.4.3 selected as it was described above. The fit results for the diamond and sapphire are shown in Figure 5.4.5. The parameters of the fit are summarized in Table 5.4.1. Thus, the connection between the number of electrons hitting the sensors and the sensor response is defined. During the machine operation the number of particles hitting the sensors can be estimated by taking reciprocal functions. The intensity of beam halo in the BHM sensors' positions can be measured.

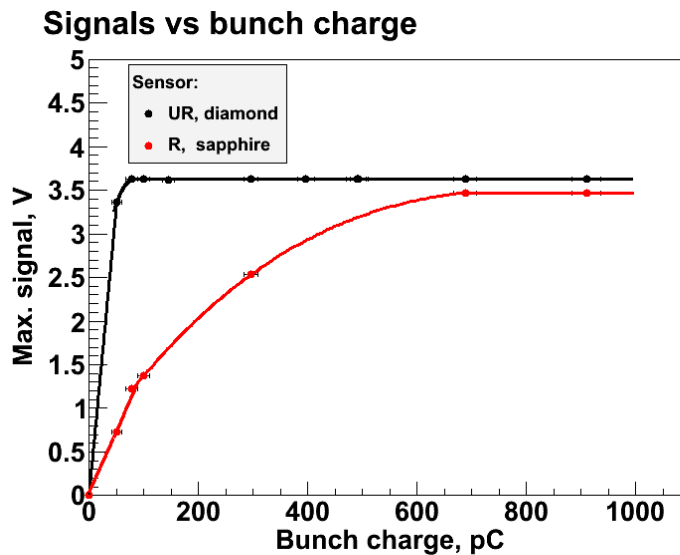


Figure 5.4.5: Fits for the maximal average signal for a diamond a sapphire sensors.

Diamond (UR)	Sapphire (R)
Low charges <50 pC $(6.6e-02)*x + (3.1e-16)$	Low charges <90 pC $(1.4e-02)*x + (3.5e-02)$
Medium charges >50 pC & <113 pC $(2.0e-06)*x^3 + (-6.7e-04)*x^2 + (6.99e-02)*x + (1.27e+00)$	Medium charges >90 pC & < 690 pC $(2.5e-09)*x^3 + (-8.7e-06)*x^2 + (9.0e-03)*x + (5.5e-01)$
High charges >113 pC $(0)*x + (3.62e+00)$	High charges > 690 pC $(0)*x + (3.47e+00)$

Table 5.4.1: Parameters for the resulting fit functions.



As the energy loss in matter depends on the energy of the incident particle, the calibration is valid for the certain energy of the electrons in the machine. As the calibration procedure is time consuming, the parameters for other energies can be estimated by calculating the ration of energy lost by incident particles to ionization in the BHM sensors at different energies to the one for the 943 MeV. As the sensors are thin enough, the losses due to radiation and their contribution to the signal can be neglected. The energy lost to ionization for the electrons of different energies in diamond and sapphire has been performed using the values given in [5.4.2]. The results are summarized in the Table 5.4.2.

Beam energy, MeV	Ratio of energy to ionization, sapphire	Ratio of energy to ionization, diamond
100	0.916	0.913
200	0.940	0.940
300	0.958	0.954
400	0.968	0.968
500	0.975	0.977
600	0.983	0.982
700	0.990	0.986
800	0.995	0.991
900	0.998	0.995
943	1	1
1000	1.002	1
1100	1.005	1.005
1200	1.010	1.009

Table 5.4.2: Ratio of the energy lost for ionization in the sapphire and the diamond sensors to the that at 943 MeV.

## 5.5 BHM for FLASH2

FLASH2 will be equipped with a BHM module of the same design as FLASH1 positioned the same way in the end of dump line in front of the dump. Figure 5.5.1 schematically shows FLASH facility with both sections. The BHM position is marked with red circle. The last section of the dump line with a BHM module for FLASH2 is shown in Figure 5.5.2. The voltage feed and signal readout scheme is similar to that at FLASH1 with the only difference in readout electronics, which will be the upgraded version to be used at the European XFEL. It will already contain circuits for signal limitation and integration and require signals of positive polarity. More details are given in chapter 6.

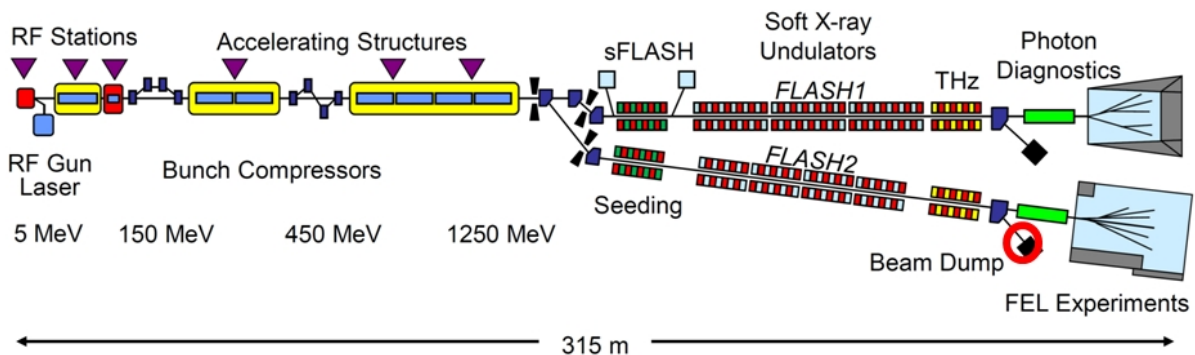


Figure 5.5.1: Schematic view of the FLASH facility with FLASH2 extension, status in March 2014. The position of the BHM at FLASH2 is marked with a red circle.

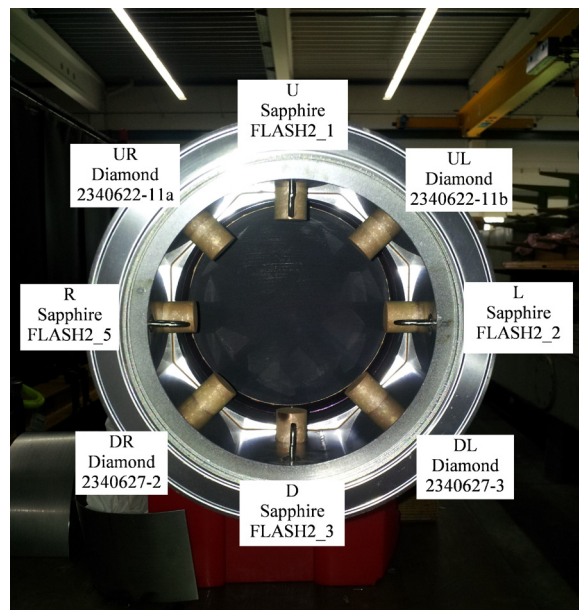


Figure 5.5.2: View to the BHM at FLASH2.

The sensors for the BHM are sapphires from the company RSA Le Rubis and diamonds from the company Element Six. They have the same dimensions and metallization type as the corresponding sensors for FLASH1. The sapphires have their CCE in the range of several percent at 300 V. Unfortunately, unlike the previous deliveries, recent diamonds from the Element Six have leakage currents up to several nA and slightly lower CCE. The higher leakage currents cannot disturb the sensors operation. However, unpredictably changing drastic currents which appear at high bias voltages can. The CCE dependence on bias voltage for these diamonds is shown in Figure 5.5.3. At low voltages polarization continues developing and dominates over signal rise due to bias voltage rise. The CCE does not reach saturation at least up to a bias voltage of 500 V. This will lead to larger signal uncertainties as bias voltage drops during charge collection. This drop will depend on the amount of charge carriers in the sensor and thus on the signal value. In case of disturbances due to drastic currents in diamond sensors during machine operation bias voltage can be lowered.

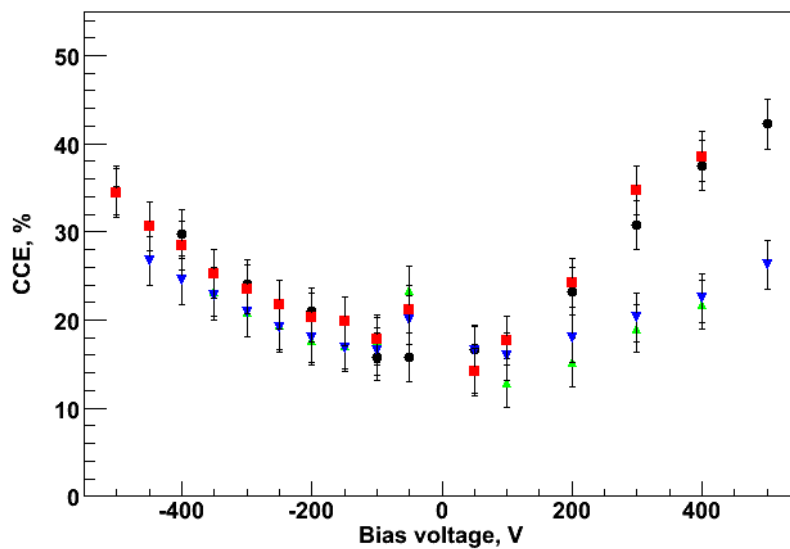


Figure 5.5.3: The CCE as a function of applied voltage for four diamond sensors for the BHM at FLASH2. The points are measured in 5 min after the bias voltage was applied.

To calibrate the BHM at FLASH2 the procedure described in this chapter can be applied, although different CCE values under the same conditions for the diamond sensors will impose an additional difficulty in centering the beam.

# Chapter 6

## BHM for the European XFEL

Successful operation of the BHM at FLASH has proven the usefulness of the system for beam dump diagnostics for linear accelerators with high beam power. Therefore, similar systems have been designed for the European XFEL, which at the time of writing of the thesis has been under construction. This chapter describes the BHM for the E-XFEL, its features and distinctions from the BHM at FLASH. The aspects of data acquisition and generation of alarm signals for the machine protection system (MPS) and possible calibration procedure are described.

### 6.1 Location and tasks

The E-XFEL is suited to provide a beam power of 600 kW when it is reaching full specification. Due to limitations of the dump construction technology the full power can only be run, if the beam is split into two parts and send downstream of two separate beam lines, each equipped with a beam stop or dump capable to take an average beam power of 300 kW. In order to reach this power several intermediate dumps are foreseen for tune up of the accelerator and for an emergency abort of the beam.

The locations where the beam can be stopped to maintain the beam transmission are: downstream the injector (injector dump) and after each of 2 bunch compressors (bunch compressor (BC) dumps). After the main linac the beam can either be send through the undulator systems towards one of the two main dumps mentioned before, or to a third dump system located in the beam distribution system, the so-called distribution dump. It is capable to absorb the beam with an average power of 300 kW and serves for tuning of the whole accelerator and as an essential location for fast beam abort in case of failures.

The bunch compressor dump lines are relatively short and not designed to take long trains on a regular basis. Therefore, their diagnostics can be handled without beam halo monitor. The injector and the main dumps are designed to handle long bunch trains. Therefore, they are extent and it is reasonable to equip them with the BHMs. Figure 6.1.1 shows locations for the

BHM at the E-XFEL. The current layout of the machine has 1 injector and 3 main dumps. The second injector dump is foreseen to be constructed later. The tasks of the BHM for the injector and for the main dumps are slightly different.

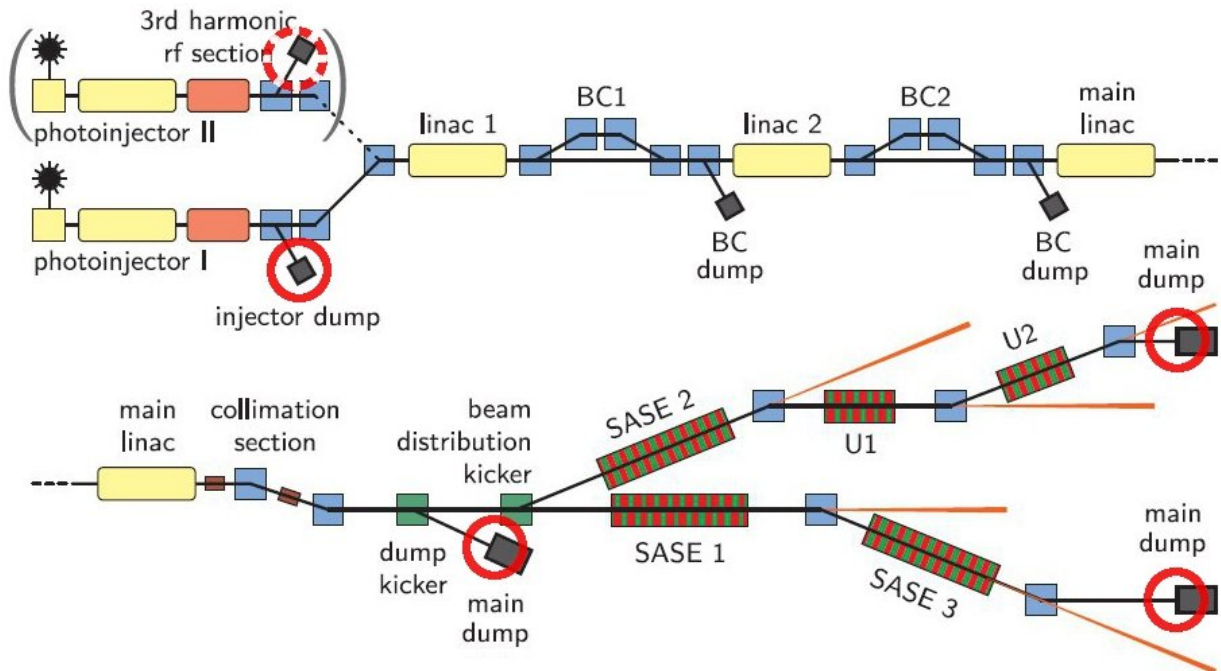


Figure 6.1.1: Layout of the E-XFEL with marked locations of the BHM (red circles). The dashed red circle marks the location of the dump in the foreseen second injector section.

Figure 6.1.2 schematically shows the injector dump line and its diagnostics components. At the end of the line containing 2 quadrupole magnets, 2 BPMs and a toroid and an OTR screen, there is a section with ionization chambers, BLMs and BHM.

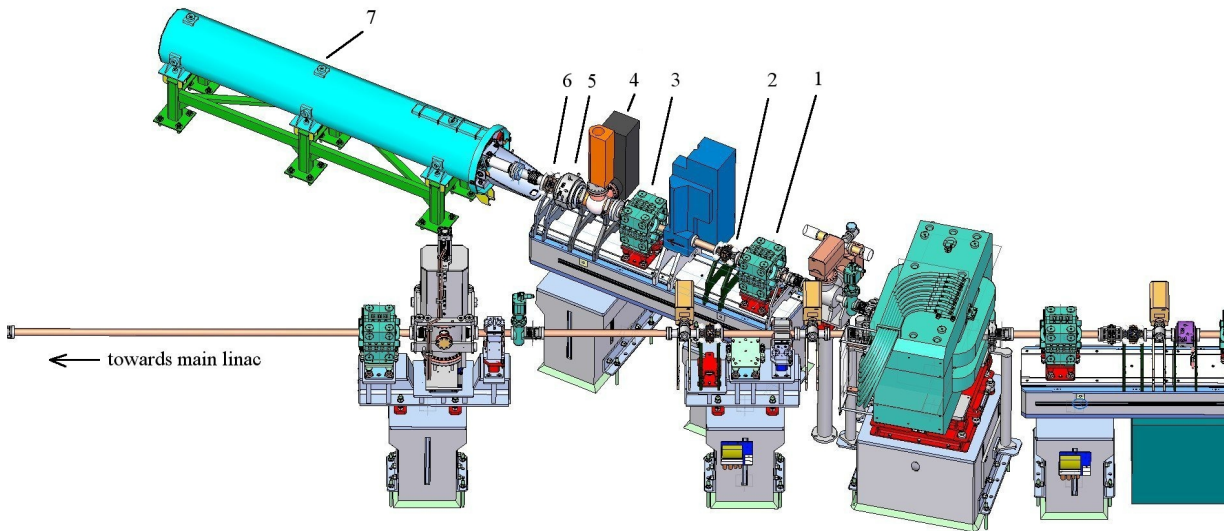


Figure 6.1.2: Schematic view of the INJ dump line: 1,3 – quadruple magnets, 2, 5 – BPM, 4 – toroid, 6 – the last section with absorber, 7 – outer dump vessel. The magnet on the right directs the beam either into the dump section or towards the main linac.

The last section of the injector dump line, which will be installed in the outer dump vessel, is schematically shown in Figure 6.1.3. The BHM is positioned directly in front of the absorber. It has the same task as the BHM at FLASH. Pipes to route the BHM cables and pipes which contain BLMs and ionization chambers are positioned upstream of the BHM module.

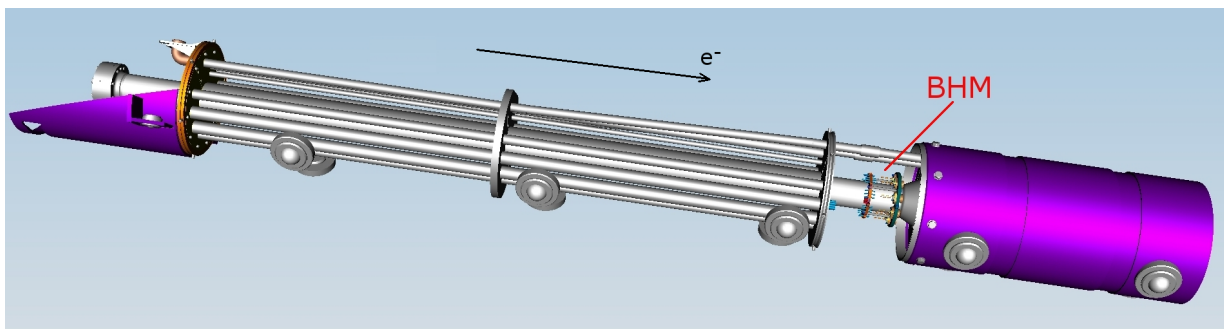


Figure 6.1.3: Last section of the injector dump line with a BHM module.

Figure 6.1.4 shows a cross section of the last section of the injector dump line upstream the BHM module. The positions of the scintillator BLMs (red circles), ionization chambers (blue circles), the cables for the BHM (light green circles) and also temperature sensors (dark green) and dose meters (dark yellow) are marked.

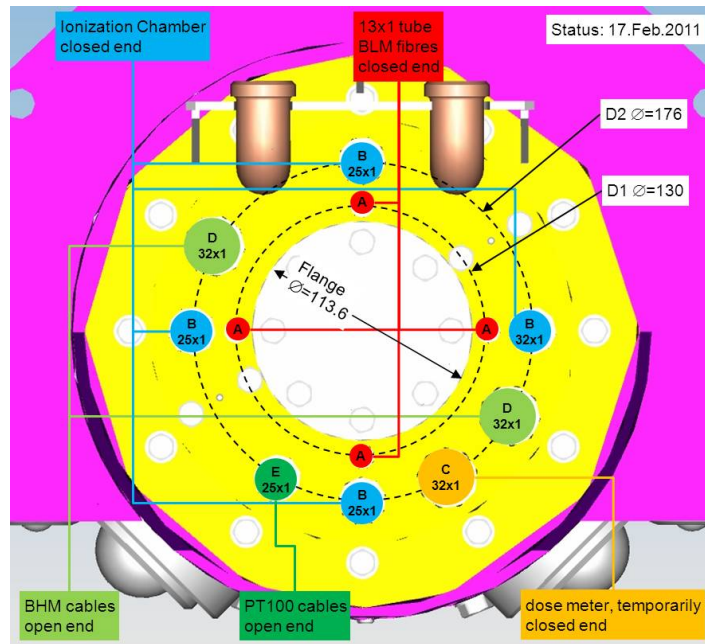


Figure 6.1.4: A cross section of the injector dump line upstream of the BHM showing the ionization chambers and BLMs.

The full energy main dump lines encompass 2 quadrupole magnets, 2 sweeper magnets, 2 steerer magnets, a toroid, a BHM, 3 BPMs, an OTR screen, 4 BLMs and 4 ionization chambers. The drawing of a main dump line downstream of the last sweeper magnet is shown in Figure 6.1.5. The BLM fibers and ionization chambers are positioned azimuthally around the beam pipe directly in front of the dump. The BHM is situated in front of the diameter step that is purposed to contain the beam envelope defocused by the quadrupole magnets. The task of the BHM in the main dumps is to ensure that the beam and the beam halo fit to the aperture defined by the beam pipe at that location. Since there are no magnets downstream this position and, and the distance to the last quadrupole is chosen correctly, particles passing this aperture can be safely transported down to the dump.

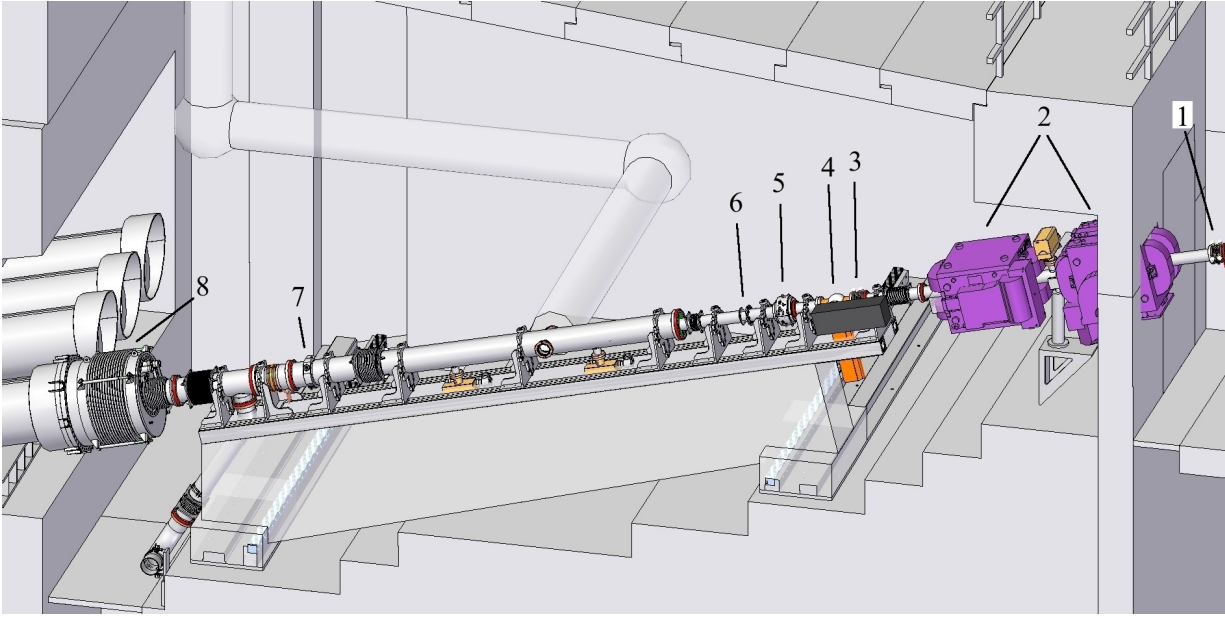


Figure 6.1.5: Schematic view of a main dump line downstream of the last sweeper magnet: 1, 3 and 7 – BPMs, 2 – dipole steerer magnets, 4 – OTR screen, 5 – toroid, 6 – BHM, 8 – position of ionization chambers and BLMs. The beam direction is from right to left.

## 6.2 Description of the BHM for the E-XFEL

A BHM module for the E-XFEL is shown in Figure 6.2.1. It contains 8 sensors, 4 pCVD diamonds and 4 synthetic sapphires, placed alternately and uniformly distributed in azimuthal direction inside cups. The design of the BHM for the injector and the main dumps is the same with the only difference in the diameter of the opening for the beam pipe. The diameter of the opening is 70 mm for the injector dump and 98 mm for the main dump. The sensor cups serve to stop low energy backscattered electrons and to protect the sensors mechanically.

The module is mounted on the beam pipe; the sensors are situated outside the pipe to avoid fragile vacuum feedthroughs and the danger of vacuum leaks. The sensor holder has been designed such that the orientation of the sensors with respect to the beam is the same as at FLASH (Figure 6.2.2). The plates of all 8 sensors are oriented perpendicular to the beam direction.

The bias voltage feed and signal readout scheme for the BHM sensors at the XFEL is shown in Figure 6.2.3. It is very similar to the one at FLASH. From the simulation of the electronics behavior it was found that reflections of the signal, shown in Figure 5.3.1, can be cancelled out by adding a 50  $\Omega$  termination resistor in series to charge storage capacitor inside the HV filter box.



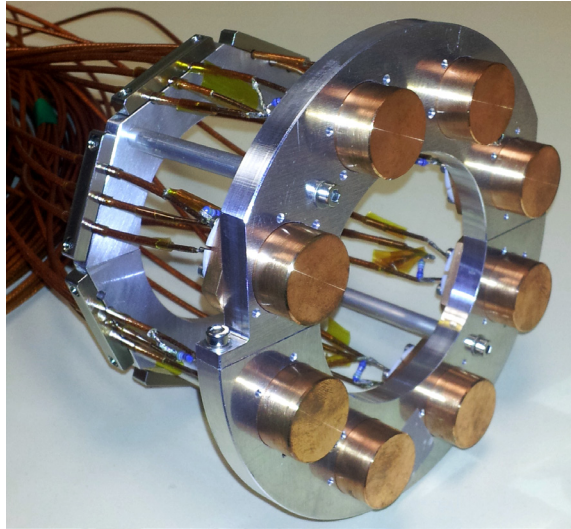


Figure 6.2.1: The XFEL-type BHM.

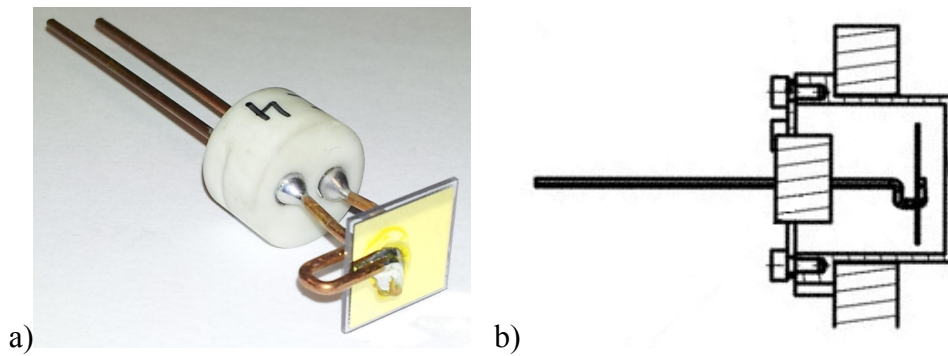


Figure 6.2.2: A BHM sensor: a) in holder ready for installation, b) schematic position inside the cup.

Kapton KAP50-5 cables with a radiation tolerance up to  $10^7$  Gy [6.2.1] will be used in the injector dump to connect the sensor and the HV filter box, since the last section of the injector dump line will be hidden inside a concrete block and access to it will be difficult. In the main dumps the BHM is easy to access and radiation hard GX 03272 D-06 cable with lower radiation tolerance will be used. The cables upstream of the HV filter box will be the same in the injector and main dumps. Standard HV cables will connect the HV filter box with the connector adaptor and the connector adaptor with the HV power supply. Standard  $50\ \Omega$  cables will be used for the signal line connecting the HV filter box to the connector adaptor. Short  $50\ \Omega$  cables will connect the connector adaptor and the readout electronics.

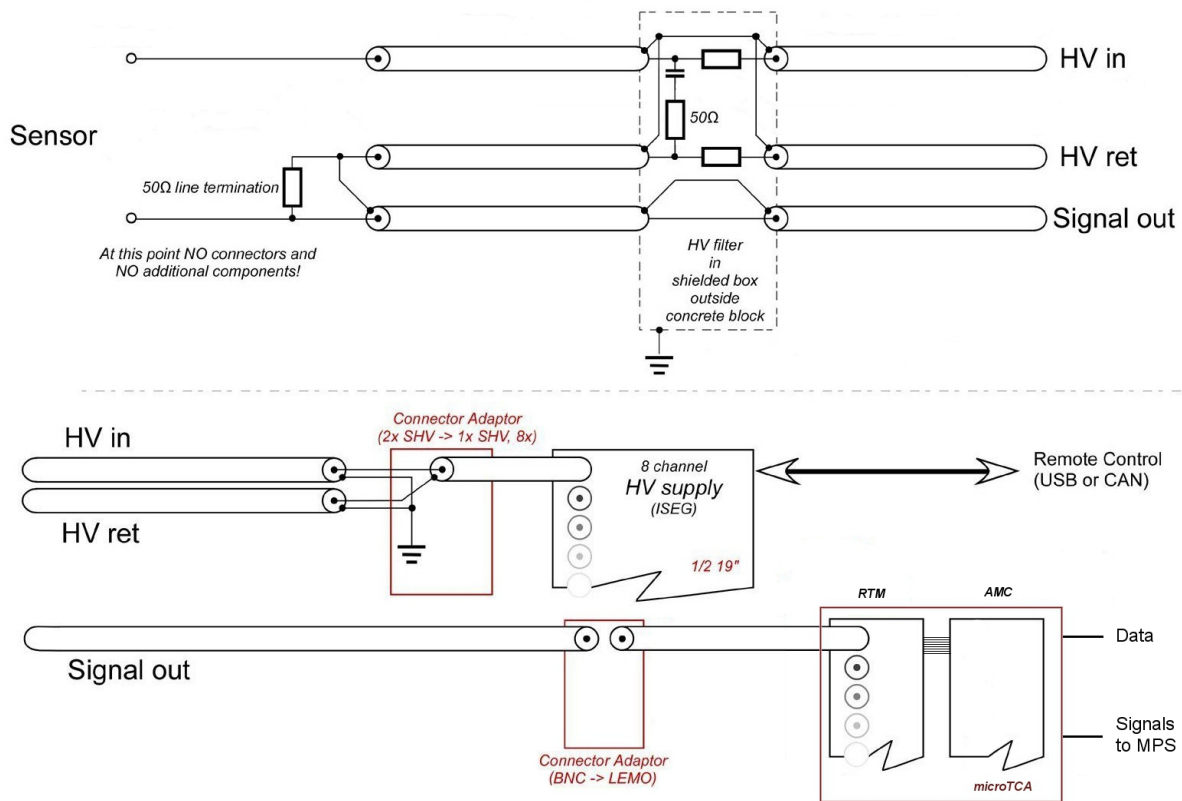


Figure 6.2.3: Bias voltage feed and signal readout scheme for each BHM sensor at the E-XFEL.

At the E-XFEL microTCA ( $\mu$ TCA) [6.2.2] was chosen to be the standard for the readout electronics. Figure 6.2.4 shows a  $\mu$ TCA crate with 2 main components for signal processing and data handling for a system like BHM. The Rear Transition Module (RTM) accepts signals and supports analog signal processing and digitization. The Advanced Mezzanine Card (AMC) maintains digital signal handling.

The BHM RTM module contains all stages of analog signal processing. Positive single-ended signals are converted into bipolar signals, attenuated, protected from over-voltage, fed into a logarithmic amplifier and shaped in order to match the requirements of the analog-to-digital converter (ADC). A 45 Msamples/s 14-bit ADC with data sampling synchronous to the 4.5 MHz bunch clock is used to digitize the signals from all 8 BHM channels. The shaping time of the signal is within 222 ns, hence the signals from consecutive bunches do not overlap. Digital data from the ADC located on the RTM is transmitted serially to an FPGA on the AMC board via the Zone 3 connection of the two boards. The RTM also carries 8 channels of analog comparators and 8 channels of digital-to-analog converter (DAC) that support fast algorithm of alarm generation for the machine protection system. The description of all algorithms of alarm generation for the BHM is described later in section 6.3.2.

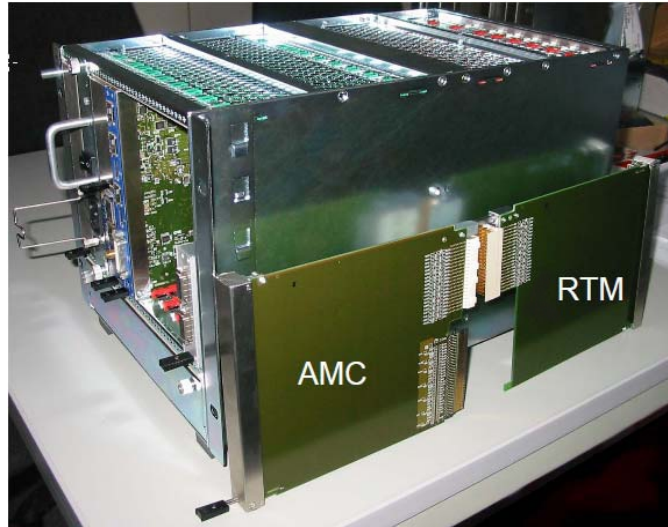


Figure 6.2.4: A  $\mu$ TCA crate with an AMC and an RTM.

The multipurpose AMC board manufactured for DESY (DAMC02) [6.2.3] carries a Virtex-5 FPGA that manages the ADC readout, data handling, controls the DAC's codes and data transfer to data server and alarm generation for the MPS.

The signal from a prototype of the BHM RTM imitating signal from a BHM sensor for a single bunch and the digital data from the ADC are shown in Figure 6.2.5. This figure shows the ideal case of losses attributed to the bunch and does not reflect the case when losses arise between bunches. The losses between bunches, e. g. due to dark current, will contribute to the integrated analog signal of each of these two bunches. The electronics picks up 10 samples per channel for each bunch. The FPGA on the AMC board calculates the integral below the signal waveform and/or defines the amplitude as the maximal value out of the 10 and transmits either of them to the data server. The final decision on which of these two quantities is transmitted will be made during commissioning of the BHM. For debugging purposes the regime with transmission of the full set of data, 10 samples per bunch per channel, is foreseen either in form of raw data set or as a plot representing the data. The algorithms of alarm generation for the MPS utilize the integral signal calculated over a certain time interval. The transmission of alarms to the MPS will be described in the following section.

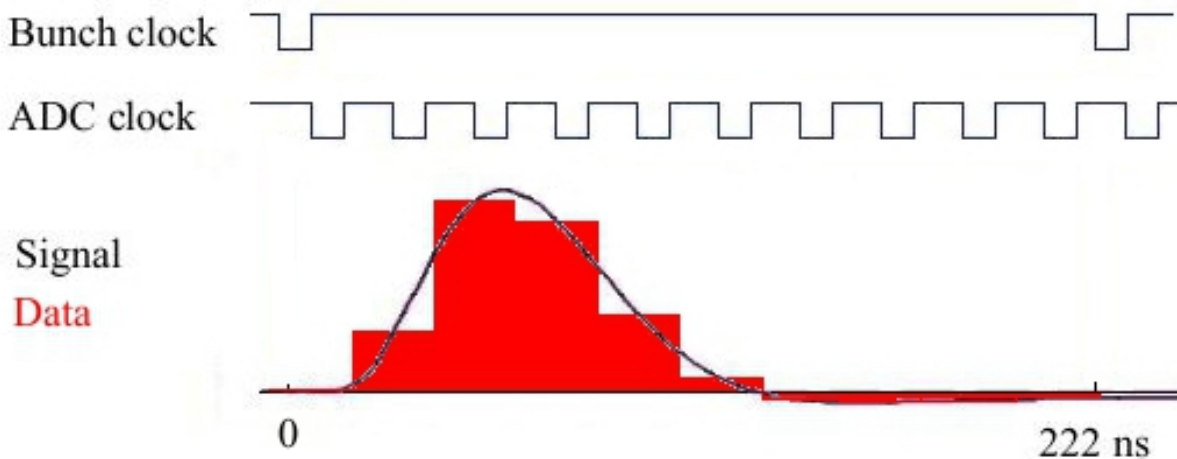


Figure 6.2.5: Analog signal and digital data of the BHM for 1 bunch. The analog signal shape is simulated by using a BHM RTM prototype.

## 6.3 The MPS and BHM alarm signals

### 6.3.1 MPS system

The MPS aims to ensure safe operation of the E-XFEL. In order to reach the goal it performs the following tasks during the machine operation:

- collects the status signals and alarms provided by different subsystems in the accelerator
- evaluates the response using internal alarm-response matrices
- constantly informs the timing system about the maximum number of allowed bunches and available accelerator sections
- in case of a critical situation, immediately stops the beam by directly acting on the laser or on dump kicker
- forwards certain signals to other subsystems.

The MPS architecture is an issue in the large machines like E-XFEL. Taking into account its total length, bunch repetition rate and latency of the electronics, up to 100 bunches could be lost before the laser is blocked. This number is mainly defined by the size of the facility, i. e. traveling time of the signals and the number of bunches released in the gun before the stop signal arrives. The MPS purposes to achieve short reaction times and minimize the number of possible lost bunches. The MPS implements a distributed master/slave architecture keeping short distances between components as shown in Figure 6.3.1.1. 2 master and 130 slave modules are distributed along the machine in a mixed daisy chain – star topology. Each slave module has digital inputs from the critical subsystems, such as BLMs, BHMs, toroids, BPMs etc. These slave modules are connected via optical fibers with one of the two master modules. Optical fibers allow fast signal transmission with no electromagnetic interference. The master

modules are located near the injector and near the linac dump kicker and have direct connections, respectively, to the injector lasers and to the dump kicker. These direct connections allow them in case the alarms are received and considered as dangerous to stop injection of new bunches and to dump bunches that are already in the machine safely in the beam distribution area.

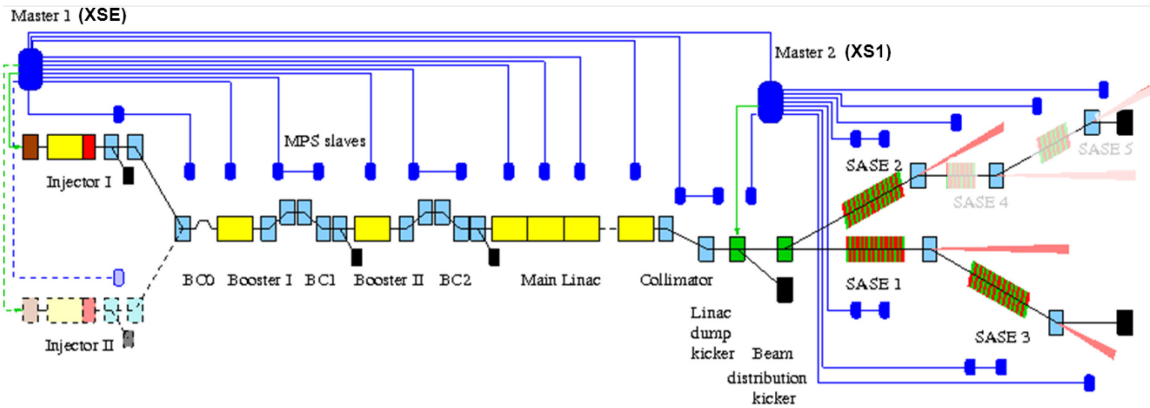


Figure 6.3.1.1: The MPS architecture at the E-XFEL.

The MPS bases its operation on two data structures: the beam mode vector and the section pattern vector. The beam mode vector defines the number of bunches allowed in a certain accelerating section. The section pattern vector defines beam transmission in several subsections of the machine. The MPS forwards this information to the timing system, which, together with the desired bunch pattern set by the operator, generates the table of bunch patterns for each train.

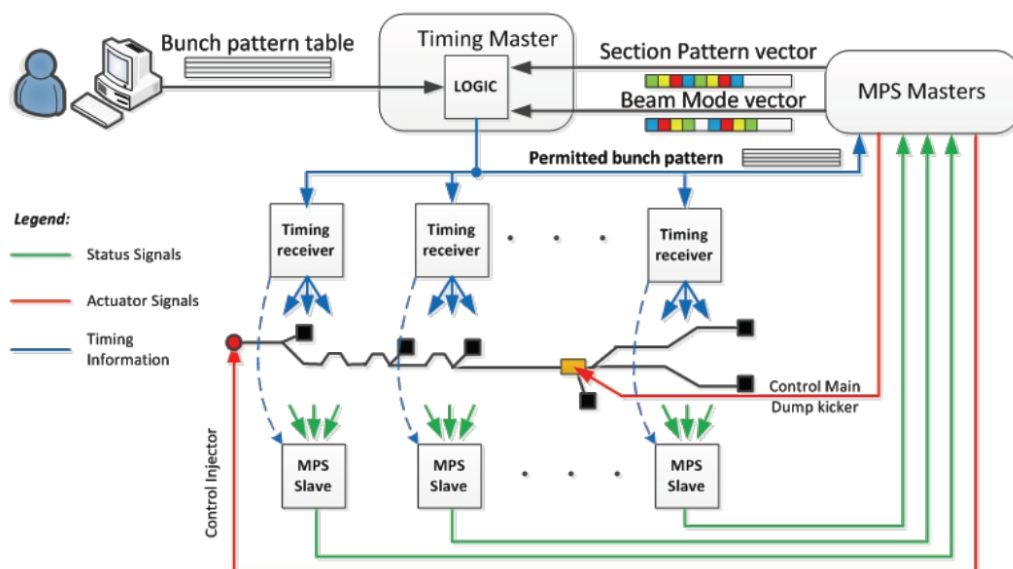


Figure 6.3.1.2: The interface of the MPS to the timing system at the E-XFEL.

The beam mode vector represents the 32-bit sequence that sets the beam mode individually for each of the 6 sections in the E-XFEL (Figure 6.3.1.3). 8 bits are reserved for 2 additional sections. Five different beam modes are distinguished:

- “0” – no bunches allowed in the section
- “1” – single bunch mode
- “S” – short bunch mode with not more than 30 bunches per train
- “M” – medium mode with 300 to 500 bunches per train
- “F” – full mode with no restrictions.

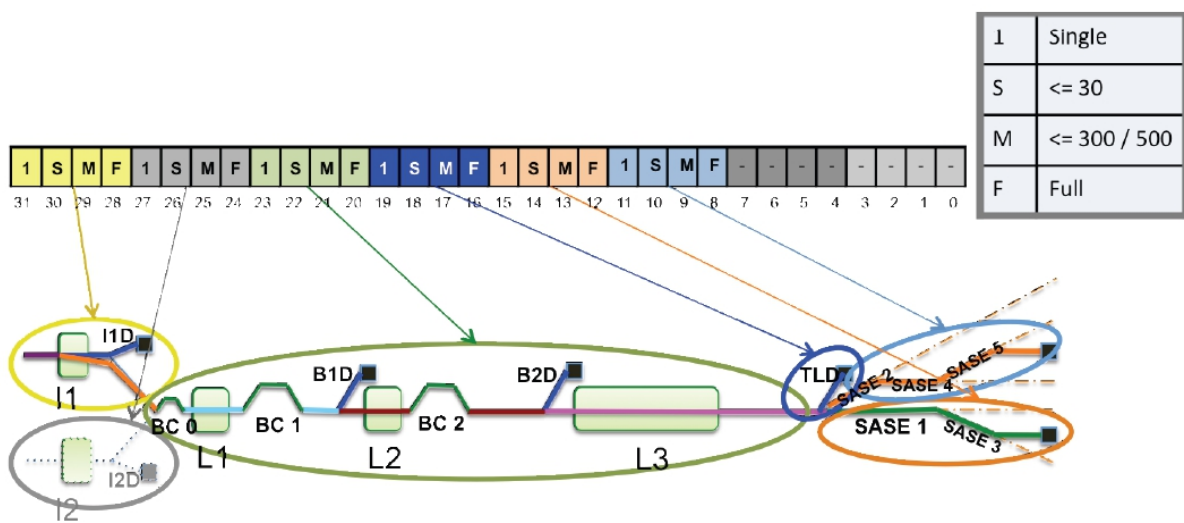


Figure 6.3.1.3: Beam mode vector generated by the MPS.

Section pattern vector is a 32-bit sequence each bit of which corresponds to a subsection of the machine as shown in Figure 6.3.1.4. It defines the beam distribution scheme.

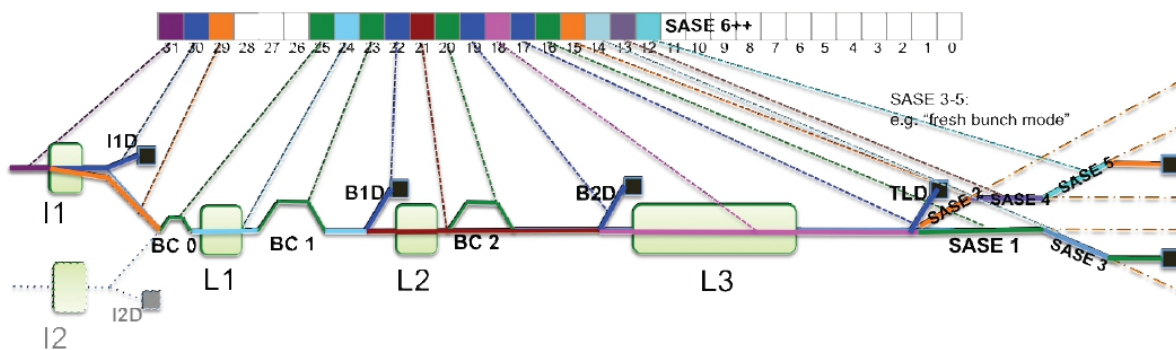


Figure 6.3.1.4: Section pattern vector generated by the MPS.

### 6.3.2 BHM alarm signals

The BHM at the E-XFEL is supposed to deliver alarm signals to the MPS. One fast alarm algorithm based on analog signal and three alarm algorithms based on digital data handling will be implemented. The three algorithms are:

- single bunch
- multiple bunches
- integral over bunch train.

These algorithms are common for BLMs and BHM and cover all possible dangerous conditions which needed to be signaled upon with a certain redundancy. Very large losses during a single bunch meaning very large signal amplitudes from the BLMs and BHMs indicate that the following bunches can bring further losses and the situation may become dangerous. To warn about this situation is the task of single bunch algorithm. Large losses during many bunches of the same frame are dangerous. To make alarm about this the multiple bunches algorithm and integral over train algorithm are used.

The fast alarm algorithm is a redundant algorithm realized on the RTM in analog circuitry design and the firmware of the FPGA. It has to provide single bunch alarms even in case of AMC/FPGA malfunction. The principle of the algorithm is explained with the Figure 6.3.2.1. Behind the receiver the signal is split and fed in parallel to 2 shapers. The first one, marked as “slow”, shapes the signal for the ADC, the second, marked as “fast”, shapes the signal for analog comparator. The signal amplitude is compared with a predefined threshold and the alarm is generated, as soon as the threshold has been overcome. The analog comparators provide shortest possible response on potentially dangerous conditions compared to alarms generated by other algorithms. These will have a certain delay defined by the time required for digitization, for data transmission to the AMC and its handling by the FPGA.

All three digital algorithms are realized on the AMC board. The FPGA processes the digital data from the ADC for each BHM sensor and makes decision upon alarm generation. The idea for the single bunch algorithm is the following. The integral over 10 data samples - the interval between bunches – is calculated. If the value exceeds a predefined threshold, alarm is generated.

Multiple bunches algorithm implies counting events specific for the single bunch algorithm within the same bunch train. Alarm is generated when the number of the events reaches a certain predefined threshold.

According to the integral over bunch train algorithm, the integral is calculated consequently for each bunch within a train. The integrals for the bunches are summed up. Alarm is generated, if the sum larger than a certain value is reached.

Analog and digital alarms are transmitted to the MPS using RS-422 standard. Each pair of cables corresponds to one sensor channel.

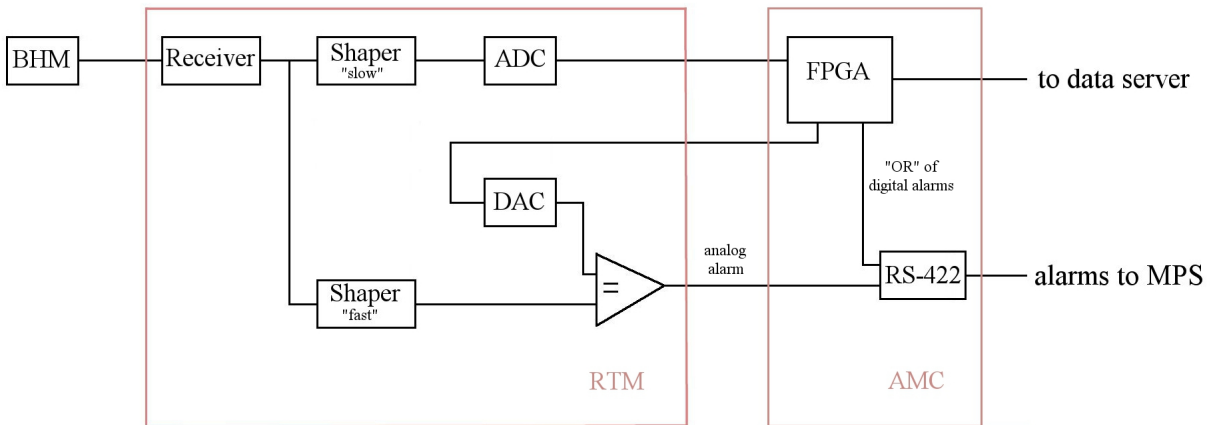


Figure 6.3.2.1: Schematic view of the BHM RTM. The analog signal amplitude is compared with to a predefined threshold and alarm is generated, if the amplitude exceeds the threshold.

The alarm handling is solely the task of the MPS. It can either react to or ignore the alarm applying a mask for certain systems.

The thresholds for each of the alarm algorithms are to be defined during the BHM commissioning and further operation.

## 6.4. Calibration procedure

As the dump lines of FLASH and the E-XFEL are different, the calibration procedure established for the BHM at FLASH has to be adopted. The E-XFEL is under construction at the moment of the thesis writing, only general considerations about the BHM calibration procedure can be discussed here.

In case of the main dump, the calibration procedure can be the following. The beam without defocusing is directed to a sensor, for example by means of the steerer magnets. The signal of the sensor is recorded for different bunch charges at nominal beam energy of 17.5 GeV. The nearest to the BHM OTR screen is used to observe the beam shape after each measurement. To cross check the measurements GEANT4 simulations shall be performed. Figure 6.4.1 shows two possible directions of the beam for the foreseen simulations. Among a variety of ways for the beam particles to hit a BHM sensor these two directions represent two ultimate paths. In the first case a Gaussian shaped beam with the nominal parameters for the accelerator is generated in the position where the beam pipe is deflected to the dump line. The beam is then directed parallel to the pipe and hit a BHM sensor. In the second case a Gaussian beam widened by the quadrupole magnets will be generated in the center of the last magnet (steerer magnet) and directed to a BHM sensor. In order to have more comprehensive picture, simulations with different beam directions can be performed.



The beam energy in the injector dump is 130 MeV. The BHM calibration in the injector dump will be the same as for the main dump.

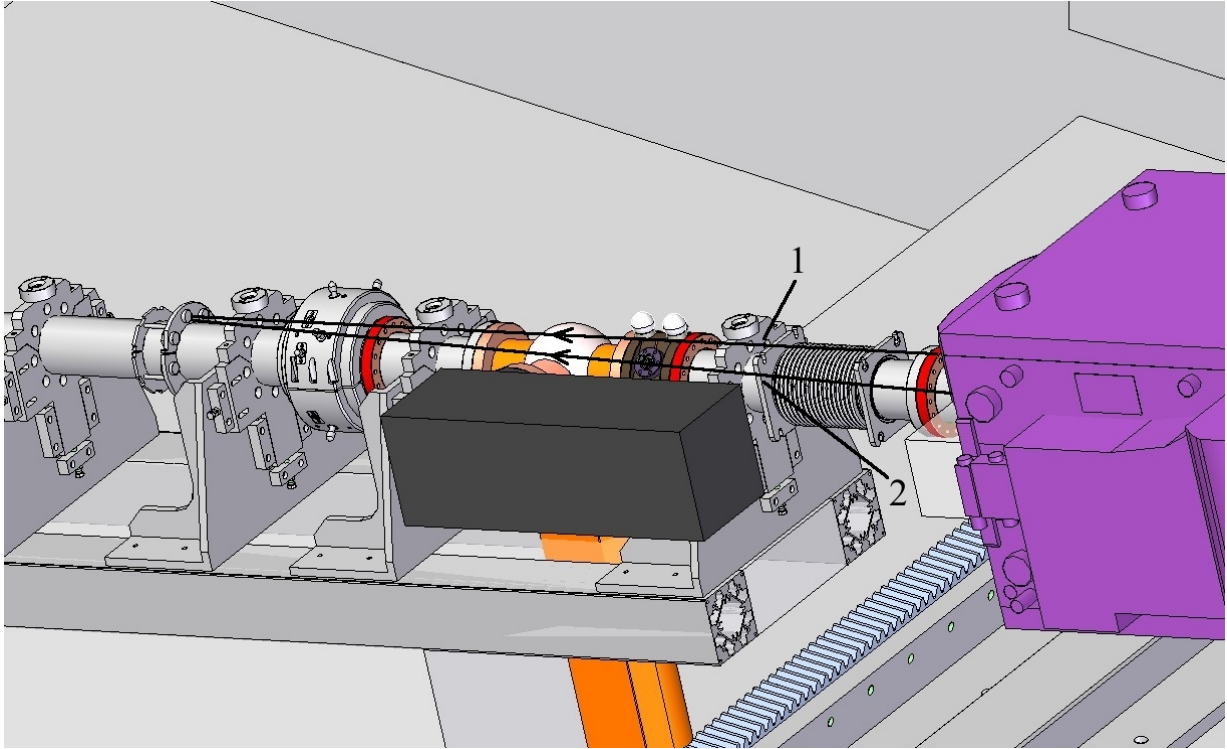


Figure 6.4.1: Beam directions in the simulations to support the BHM calibration in a main dump: 1 –beam is generated in the center of the last steerer magnet and directed a BHM sensor, 2 – the beam is generated in the position where the beam is deflected to the dump line and directed parallel to the beam pipe to a BHM sensor.

At the moment of the thesis writing the BHM module for the injector dump was assembled only. The CCE as a function of bias voltage for 4 BHM diamonds is shown in Figure 6.4.2. The CCE for all 4 diamonds rises with bias voltage reaching saturation at around 200 V for both polarities. The saturated values of the CCE are roughly the same. The reasonable operating bias voltage is 300 V. It can be lowered in case if erratic currents are observed. The sapphire sensors are made of the material produced by the Rubis RSA company. Their estimated CCE is several percent at 500 V, equal for all 4 sensors. The sapphire sensors can be operated at bias voltages up to 500 V.

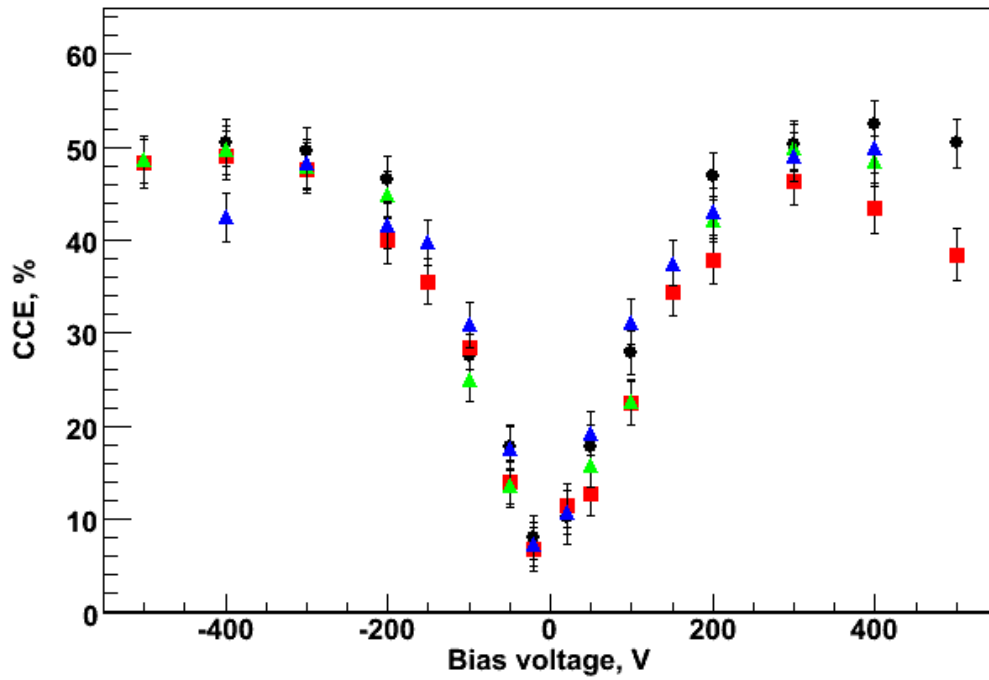


Figure 6.4.2: CCE as a function of bias voltage for the 4 BHM diamond sensors in the injector dump.

Equal values of the CCE for the BHM sensor of the same type in the same module mean that the signals from the sensors of the same type will be the same under equal conditions. It is expected that the BHM sensors of the same type for the main dumps will be have equal CCEs as well.

# Chapter 7

## Summary and Conclusions

### 7.1 Summary

This thesis is dedicated to development of radiation hard sensors based on synthetic diamond and sapphire material and their application in the Beam Halo Monitor for the FLASH and the European XFEL.

In order to complete the data on radiation hardness of pCVD diamonds – a rather well-studied sensor material – radiation hardness tests with electrons were performed. Synthetic sapphire was used for the first time as a sensor material. The main sensor characteristics of sapphire sensors were measured, and sapphire sensors were proven to be operational.

For both sensor types a full system was designed, built and commissioned to use them in the BHM at FLASH. Encouraged by the success, a similar system was designed for the European XFEL which is currently under construction.

#### 7.1.1 Development of diamond and sapphire sensors

Radiation hardness tests of ultra pure pCVD diamonds sensors have been performed with 10 MeV electrons. After absorption of 10 MGy, the main sensor characteristics – charge collection efficiency – has the value of 65 % of its initial value at an operational bias voltage.

The first sensors based on synthetic sapphires revealed low and repeatable leakage currents below 1 pA at bias voltages up to 500 V for both polarities. Sensors from three different manufacturers with different purity ranging from 99.994 % to 99.998 % were studied. The charge collection efficiency was measured for the different purities. No signal was detected for the sensors with the lowest purity. The sensors with the highest purity revealed charge collection efficiency up to 5 % at 500 V. Further improvement of the sapphires may lead to higher charge collection efficiency but will likely also lead to an increase of the costs.

A more promising direction in development of sapphire sensors is dedicated design of an assembly composed of several plates of synthetic sapphire. The first prototype consisting of 8

plates has been tested at the DESY synchrotron with 5 GeV electrons. It was proven to be operational with the signal corresponding to the expected level.

### **7.1.2 Beam Halo Monitor for the European XFEL**

The Beam Halo Monitor using four pCVD diamond and four synthetic sapphire sensors of 1 cm<sup>2</sup> size and 500 micrometer thickness developed for FLASH has been successfully commissioned, calibrated and operated for 4 years. The use of pCVD diamond sensor and synthetic sapphire sensors with about a factor of 10 different charge collection efficiency improved the dynamic range of the system. Tests of a pCVD diamond at PITZ have shown that the diamond sensor in the given configuration is capable to detect bunches of electrons with a charge as low as 1-2 pC.

The experience gained during the years was essential for the BHM design at FLASH2 and the European XFEL. The system for FLASH2 is ready for commissioning.

For the European XFEL several BHMs were designed for the injector and the main dump.

## **7.2 Conclusions**

The technology of beam halo monitors based on pCVD and synthetic sapphire sensors has been demonstrated at FLASH. It can be applied as diagnostics tool for accelerators with high power beams.

Based on the experience acquired during four years of operation at FLASH beam halo monitors are designed for several beam dumps at the European XFEL. These BHMs will be integrated in the safety system of the European XFEL.

Further investigation of synthetic sapphire as a promising sensors material is necessary. These sensors may become a good and less expensive alternative for synthetic diamond sensors in beam halo and beam conditions monitoring.

# Bibliography

- [1.1] <http://www.xfel.eu>
- [1.2] M. Alterelli et al. (eds), "The European X-Ray Free-Electron Laser. Technical design report", DESY-06-097
- [1.3] <http://flash.desy.de>
- [1.4] M. Vogt, B. Faatz, J. Feldhaus, K. Honkavaara, S. Schreiber, R. Treusch, The Free-Electron Laser FLASH at DESY, Proc. of IPAC2013, TUPEA004, Shanghai, China, 2013
- [2.0.1] <http://doris.desy.de>
- [2.0.2] H. J. Behrend, E. E. Koch, C. Kunz and G. Mulhaupt, DORIS as a part-time dedicated source of synchrotron radiation, Nucl. Instrum. and Meth. 152, pp. 37-41, 1978
- [2.0.3] <http://www.helmholtz-berlin.de/zentrum/historie/bessy>
- [2.0.4] D. Arnold, The BESSY electron storage ring as a standard radiation source for X-radiation and the determination of photon emission probabilities of radionuclides." PhD thesis, TU Berlin, 1991
- [2.0.5] <http://petra3.desy.de>
- [2.0.6] [http://photon-science.desy.de/facilities/petra\\_iii](http://photon-science.desy.de/facilities/petra_iii)
- [2.0.7] H. Franz et al., PETRA III: DESY's New High Brilliance Third Generation Synchrotron Radiation Source, Synchrotron Radiat. News, 19, pp. 25-29, 2006
- [2.0.8] <http://www-als.lbl.gov>
- [2.0.9] A. Jackson, The Advanced Light Source at the Lawrence Berkeley Laboratory, Nucl. Instrum. and Meth. in Phys. Res. B 56/57, pp. 375-378, 1991
- [2.0.10] <http://www.aps.anl.gov>
- [2.0.11] D. M. Mills, The Advanced Photon Source: a status report, Nucl. Instrum. and Meth. in Phys. Res. A 319, pp. 33-39, 1992

- [2.0.12] <http://www.spring8.or.jp>
- [2.0.13] T. Shintake et al., Status of Spring-8 compact SASE source FEL project, Nucl. Instrum. and Meth. in Phys. Res. A 507, pp. 382-387, 2003
- [2.0.14] <http://www.esrf.eu>
- [2.0.15] J. M. Filhol, Status of the ESRF, Proc. of EPAC'1994, p. 8, 1994
- [2.0.16] [https://portal.slac.stanford.edu/sites/lcls\\_public](https://portal.slac.stanford.edu/sites/lcls_public)
- [2.0.17] H. Winick, The linac coherent light source (LCLS): a fourth-generation light source using the SLAC linac, J. Electron. Spectrosc. Relat. Phenom. 75, pp. 1-8, 1995
- [2.0.18] K. Balewski, W. Brefeld, W. Decking, et al. PETRA III: A Low Emittance Synchrotron Radiation Source. Technical report, DESY, Hamburg, Germany, 2004
- [2.0.19] D. H. Bilderback, J. D. Brock, D. S. Dale, et al. Energy recovery linac (ERL) coherent hard x-ray sources. New Journal of Physics, 12, 035011, 2010
- [2.1.1] J. M. J. Madey, "Stimulated emission of bremsstrahlung in a periodic magnet field". J. Appl. Phys. 42(5), pp. 1906-1913, 1971
- [2.1.2] L.R. Elias, et al., "Observation of stimulated emission of radiation by relativistic electrons in a spatially periodic transverse magnetic field". Phys. Rev. Lett. 36(13), pp. 717-720, 1976
- [2.1.3] A. M. Kondratenko and E. L. Saldin. Generation of coherent radiation by a relativistic electron beam in an undulator. Part. Accelerators, 10, 207, 1980
- [2.1.4] R. Bonifacio, C. Pellegrini, and L. Narducci. Collective instabilities and high-gain regime in a free electron laser. Optics Communications, 50, 373, 1984
- [2.1.5] B. Faatz, J. Feldhaus, J. Krzywinski, E. L. Saldin, E. A. Schneidmiller, M. V. Yurkov, Nucl. Instrum. And Meth. A 429, 424
- [2.1.6] J. Feldhaus, E. L. Saldin, J. R. Schneider, E. A. Schneidmiller, M. V. Yurkov, Opt. Commun. 140, 341, 1997
- [2.1.7] C. Pellegrini, Nucl. Instrum. And Meth. A 445, p. 124, 2000
- [2.1.8] W. Brefeld, B. Faatz, J. Feldhaus, M. Körfer, J. Krzywinski, T. Möller, J. Pflüger, J. Rossbach, E. L. Saldin, E. A. Schneidmiller, S. Schreiber, M. V. Yurkov, Nucl. Instrum. And Meth. A 483/1-2, 62, 2002
- [2.1.9] G. Stupakov, Using the beam-echo effect for generation of short-wavelength radiation, Phys. Rev. Lett. 102, p. 074801, 2009

- [2.2.1] R. Brinkmann et al. (eds), TESLA Technical Design Report – Part II: The Accelerator, DESY 2001-011, p. II-19
- [2.3.1] <http://www.desy.de>
- [2.3.2] <http://www.linearcollider.org>
- [2.3.3] Phinney, N. Toge, N. Walker (eds), ILC Reference Design Report, ILC-REPORT-2007-001, DESY Report DESY 07-046
- [2.3.4] <http://sflash.desy.de>
- [2.3.5] <http://flash2.desy.de>
- [3.1.1] C. Chen, R. Partker, Mechanisms and control of beam halo formation in intense microwave sources and accelerators, *Phys. Plasmas* 7, 2203, 2000
- [3.1.2] A. W. Chao, *Physics of Collective Beam Instabilities in High-Energy Accelerators*, John Wiley, New York, 1993
- [3.1.3] R. B. Neal and W. K. H. Panofsky, *Science* 152, 1353, 1966
- [3.1.4] W. K. H. Panofsky and M. Bander, *Rev. Sci. Instrum.* 39, 206, 1968
- [3.1.5] A.V. Fedotov, Resonances and beam loss in high intensity rings, 20th IEEE Particle Accelerator Conference, PAC 2003, Portland, OR, e-proceedings (JACoW), pp. 383–7, 2003
- [3.1.6] A. V. Fedotov, Beam halo formation in high-intensity beams, *Nucl. Instrum. Methods Phys. Res. A* 557, pp. 216–19, 2006
- [3.1.7] A. V. Fedotov, Mechanisms of halo formation, *AIP Conf. Proc.* 693, 3, 2003
- [3.1.8] M. P. Zorzano and R. Wanzenberg, Intrabeam scattering and the coasting beam in the HERA proton ring, DESY HERA 00-06, October 2000, CERN-SL-2000-072 AP
- [3.1.9] T. O. Raubenheimer, Ion effects in future circular and linear accelerators, SLAC-PUB-95-6847
- [3.1.10] H. Burkhardt et al., Halo estimates and simulations for linear colliders, EUROTeV Report 2007–064, CLIC-Note-714
- [3.1.11] X.-L. Zhang et al., Generation and diagnostics of uncaptured beam in the Fermilab Tevatron and its control by electron lenses, *Phys. Rev. ST Accel. Beams* 11, 051002, 2008
- [3.2.1.1] H. Loos et al., Proc. FEL'08, Gyeongju, Korea, August 2008, THBAU01, p. 485, 2008

- [3.2.1.2] V. Ginzburg, and I. Frank, Radiation of a uniformly moving electron due to its transition from one medium into another, *J. Phys., USSR*, 9, 353, 1945
- [3.2.1.3] E. L. Saldin, E. A. Schneidmiller, and M. V. Yurkov, An analytical description of longitudinal phase space distortions in magnetic bunch compressors, *Nuclear Instruments and Methods in Physics Research A* 483, 2002
- [3.2.1.4] A. H. Lumpkin, N. S. Sereno, W. J. Berg, M. Borland, Y. Li, and S. J. Pasky, Characterization and mitigation of coherent-optical-transition-radiation signals from a compressed electron beam, *Phys. Rev. ST Accel. Beams* 12, 080702, 2009
- [3.2.1.5] P. Lecoq et al., *Inorganic Scintillators for Detector Systems*, Springer Verlag, Berlin–Heidelberg, 2006
- [3.2.1.6] B. Walasek-Höhne, G. Kube, Scintillating screen applications in beam diagnostics, *Proc. of DIPAC2011*, Hamburg, Germany, 2011
- [3.2.1.7] O. H. Altenmueller, R. R. Larsen, and G. A. Loew, Investigations of Travelling-Wave Separators for the Stanford Two-Mile Linear Accelerator, *Review of Scientific Instruments*, 35, p. 438, 1964
- [3.2.2.1] N. Kurita et al., *Proc. PAC 95*, Dallas, p. 2512, 1995
- [3.2.2.2] P. Forck, Lecture notes on beam instrumentation and diagnostics, [http://www-bd.gsi.de/conf/juas/juas\\_script.pdf](http://www-bd.gsi.de/conf/juas/juas_script.pdf), JUAS, Archamps, France, January-March, 2011
- [3.2.2.3] R. Lorenz, Cavity Beam Position Monitors, *Proc. Beam Instr. Workshop BIW 98*, Stanford AIP 451, p. 53, 1998
- [3.2.4.1.1] G. F. Knoll, *Radiation Detection and Measurement*, John Wiley, New York, 1999
- [3.2.4.1.2] Average Energy Required to Produce an Ion Pair, *International Commission on Radiation Units and Measurements*, ICRU Report 31, Washington D.C., 1979
- [3.2.4.2.1] K. Wittenburg, Radiation damage in pin photodiodes, *NIM A270* (1988) pp.56-61
- [3.2.4.3.1] E. J. Sternglass, Theory of secondary electron emission by high-speed ions, *Phys. Rev.* 108, 1, 1957
- [3.2.4.3.2] D. Kramer et al., Secondary electron emission beam loss monitor for LHC, *Proc. 8th European Workshop on Diagnostics and Beam Instrumentation*, DIPAC 2007, Venice, (2007)
- [3.2.4.3.3] V. Agoritsas and C. Johnson, EMI aluminum cathode electron multipliers: CERN tests, *CERN MPS/CO Note* 71–51, 1971



- [3.2.4.3.4] L. Fröhlich, Experience from the commissioning of the FLASH machine protection system, Proc. 37th ICFA Advanced Beam Dynamics Workshop on Future Light Sources, Hamburg, Germany, 2006
- [3.2.4.3.5] L. Fröhlich, First operation of the flash machine protection system with long bunch trains, Linear Accelerator Conference, Linac06, Knoxville, TN, (2006)
- [3.2.4.4.1] W. R. Leo, Techniques for Nuclear and Particle Physics Experiments, Springer, Berlin, ISBN 3-540-17386-2, 1987
- [3.2.4.4.2] Glenn F. Knoll, Radiation detection and measurement (3rd ed.). New York: Wiley. ISBN 0-471-07338-5, 1999
- [3.2.4.5.1] A. Pietryla, W. Berg and R. Merl, A Cherenkov radiation detection system for the advanced photon source storage ring, Proc. 2001 Particle Accelerator Conference, Chicago, IL, 2001
- [3.2.4.5.2] J. Cohen-Tanugi et al., Optical properties of the DIRC fused silica Čerenkov radiator, SLAC PUB-9038
- [3.3.1] H. Aoyagi et al., Beam Halo Monitor Using Diamond Detector for Interlock Sensor at XFEL/Spring-8, Proc. of DIPAC09, Basel, Switzerland, TUPB24
- [3.3.2] A. Bell, Fast Beam Conditions Monitor BCM1F for the CMS Experiment, arXiv:0911.2480
- [3.3.3] E. Griesmayer et al., A Fast CVD Diamond Beam Halo Monitor for LHC, Proceedings of DIPAC2011, Hamburg, Germany
- [3.3.4] V. Cindro et al., The ATLAS Beam Conditions Monitor, JINST 3 P02004, 2008
- [4.0.1] R. J. Tapper, Diamond detectors in particle physics, Rep. Prog. Phys. 62, pp. 1273-1316, 2000
- [4.0.2] C. Grah et al., Polycrystalline CVD Diamonds for the Beam Calorimeter of the ILC, Nuclear Science Symposium Conference Record, IEEE Vol. 2, 721-724, 2006
- [4.1.1] W. Shockley, Currents to Conductors Induced by a Moving Point Charge, J. Appl. Phys., 9, 635-636, 1938
- [4.1.2] S. Ramo, Currents Induced by Electron Motion, Proc. IRE, 27, 584-585, 1939
- [4.2.1] J. Beringer et al., Particle Data Group, Phys. Rev. D86, 2012
- [4.2.2] J. Lindhard, M. Scharff and H. E. Schiott, Mat. Fys. Medd. Dan. Vid. Selsk., 33, No. 14, 1963

- [4.2.3] H. H. Andersen and J. F. Ziegler, Hydrogen Stopping Powers and Ranges in All Elements , Vol. 2 of "The Stopping and Ranges of Ions in Matter", Pergamon Press, New York, 1977
- [4.2.4] H. A. Bethe, Zur Theorie des Durchgangs schneller Korpuskularstrahlen durch Materie, Ann. Phys. 5, 325, 1930
- [4.2.5] W. H. Barkas, M. J. Berger, Tables of energy losses and ranges of heavy charged particles, NASA Report, SP-3013, 1964
- [4.2.6] W. H. Barkas, J. N. Dyer, H. H. Heckman, Resolution of the, Mass Anomaly, Phys. Rev. Lett., vol. 11, no. 1, p. 26, 1963
- [4.2.7] J. Lindhard, A. H. Sørensen, Relativistic theory of stopping for heavy ions, Phys. Rev. A, vol. 53, no. 4, p. 2443, 1996
- [4.2.8] L. Landau, J. Phys., Moscow, 8:201, 1944
- [4.2.9] H. Bichel, Straggling in thin silicon detectors, Rev. of Mod. Phys., 60(3):663, 1988
- [4.2.10] H. A. Bethe, Ann. Phys. 5, p. 325, 1930
- [4.2.11] H. A. Bethe, Phys. Rev. 98, pp. 1256–1266, 1953
- [4.2.12] U. Fano, Annu. Rev. Nucl. Sci. 13, 1, 1963
- [4.2.13] CRU, ICRU Report 49, Stopping Powers and Ranges for Protons and Alpha Particles, 1993
- [4.3.1] J. Beringer et al.(PDG), PR D86, 010001, 2012
- [4.3.2] B. L. Berman and S.C. Fultz, Rev. Mod. Phys. 47, 713, 1975
- [4.4.1] G. Cavalleri et al., Extensions of Ramo's theorem as applied to induced charge in semiconductor detectors, NIM 92, pp. 137-140, 1971
- [4.4.2] K. Hecht, Zum Mechanismus des lichtelektrischen Primärstromes in isolierenden Kristallen, 1932
- [4.5.1] J. H. Crawford, L. M. Slifkin, Point Defects in Solids, New York: Plenum Press, ed. (1975)
- [4.5.2] J. D. Bacon, D. Hull, Introduction to Dislocations, 1984, ISBN 0-08-028720-4
- [4.5.3] R. J. D Tilley, Defects in Solids, John Wiley & Sons, Inc., Hoboken, New Jersey, 2008
- [4.5.4] B. R. Gossick, Disordered regions in semiconductors bombarded by fast neutrons, J. Appl. Phys., vol. 30, no. 8, pp. 1214–1218, Aug. 1959

- [4.5.5] M. Pomorski, Electronic Properties of Single Crystal CVD Diamond and its Suitability for Particle Detection in Hadron Physics Experiments, PhD thesis, Johann Wolfgang Goethe – University, Frankfurt am Main, 2008
- [4.5.6] R. J. Keddy, T. L. Nam and R. C. Burns, Synthetic diamonds as ionization chamber radiation detectors in biological environments Phys. Med. Biol. 32, 751 – 9, 1987
- [4.5.7] RD42 collaboration, Development of diamond tracking detectors for high luminosity experiments at the LHC LDRB Status Report /RD42 CERN LHCC 97-3, 1997
- [4.6.3.1] [http://www.ikp.tu-darmstadt.de/sdalinac\\_ikp/index.de.jsp](http://www.ikp.tu-darmstadt.de/sdalinac_ikp/index.de.jsp)
- [4.6.3.2] R. S. Schmidt, Optimisation of a Testbeam Setup and Background Estimates for Detectors at the ILC using Monte Carlo Simulations, Diploma thesis, BTU Cottbus, 2007
- [4.7.0.1] E. Berdermann et al., The use of CVD-diamond for heavy-ion detection. Diamond Relat. Mater., 10, pp. 1770–1777, 2001
- [4.7.0.2] E. Berdermann et al., The Diamond Project at GSI – Perspectives, Proc. of the 7th Int. Conf. on Advanced Technology and Particle Physics (ICATPP-7), October 2001, Como, Italy, 2001
- [4.7.1.1] <http://www.e6.com>
- [4.7.1.2] M. Schreck, H. Roll, and B. Stritzker, Diamond / Ir / SrTiO<sub>3</sub>: A material combination for improved heteroepitaxial diamond films; Appl. Phys. Lett. 74, 650, 1999.
- [4.7.2.1] C. Grah et al., Polycrystalline CVD Diamonds for the Beam Calorimeter of the ILC, Nuclear Science, IEEE Transactions, Volume 56, Issue 2, April 2009, pp. 462-467
- [4.7.3.1] <http://pitz.desy.de>
- [4.8.0.1] <http://www.crystal-gmbh.com>
- [4.8.0.2] <http://www.rubisrsa.com>
- [4.8.0.3] <http://global.kyocera.com/company/index.html>
- [4.8.2.1] A. Ignatenko et al., Test and First Application of Artificial Sapphire Sensors, Nuclear Science Symposium Conference Record, Knoxville TN, USA, Nov. 2010, pp. 650-654
- [4.8.3.1] S. Schuwalow, Sapphire Detectors, Instrumentation SeminarTalk, DESY Hamburg, 2013
- [4.8.3.2] <http://desy2.desy.de>
- [5.1.1] N. Baboi, New Electron Beam Diagnostics In The FLASH Dump Line, Proceedings of BIW10, Santa Fe, USA, 2010

- [5.1.2] N. Baboi et al., Magnetic Coupled Beam Position Monitor for the FLASH Dump Line, Proceedings of BIW10, Santa Fe, USA, 2010
- [5.2.1] J. Andruszkow, P. Jurkiewicz, F. Tonisch, 8-channel Fast ADC with 14 bit resolution, Reference manual v. 3.0, March 2005
- [5.3.1] [http://flash.desy.de/sites/site\\_vuvfel/content/e870/e66712/infoboxContent66713/Carwardine\\_9mA\\_FLASH\\_Seminar\\_Nov24\\_wkg.pdf](http://flash.desy.de/sites/site_vuvfel/content/e870/e66712/infoboxContent66713/Carwardine_9mA_FLASH_Seminar_Nov24_wkg.pdf)
- [5.4.1] A. Ushakov, S. Riemann, Geant4 Simulations for Diagnostic Elements in the FLASH Dump Line, TESLA-FEL\_2010-02 Report, [http://flash.desy.de/sites/site\\_vuvfel/content/e403/e1642/e71562/e71563/infoboxContent71573/TESLA-FEL\\_Add\\_2010-02.pdf](http://flash.desy.de/sites/site_vuvfel/content/e403/e1642/e71562/e71563/infoboxContent71573/TESLA-FEL_Add_2010-02.pdf)
- [5.4.2] <http://physics.nist.gov/PhysRefData/Star/Text/ESTAR.html>
- [6.2.1] <http://www.mdevacuum.co.uk/resources/downloads/pdfs/sec6.7.11.pdf>
- [6.2.2] <http://www.picmg.org/v2internal/microTCA.htm>
- [6.2.3] <http://accelconf.web.cern.ch/AccelConf/icalepcs2009/papers/tha006.pdf>

# Acknowledgements

I would like to thank Prof. Dr. Wolfgang Lohmann for the opportunity to do research on diamond sapphire sensors, for being a supervisor for my PhD studies and careful and critical reading of the thesis.

I am thankful to the FCAL-CMS group at DESY in Zeuthen for giving the opportunity to characterize the sensors. I would like to thank Dr. Wolfgang Lange and Hans Henschel for useful ideas about the design of the BHM system.

I acknowledge Dr. Sergej Schuwalow for the new ideas, fruitful discussions and useful advices.

I appreciate the support of MDI group at DESY in Hamburg, especially my local supervisors Dr. Dirk Nölle and Dr. Nicoleta Baboi for fast and critical reading of the thesis. I wish to express my gratitude to Dr. Kay Wittenburg for the opportunity to do research in the group.

I acknowledge Michael Schmitz for his support and advices during the BHM modules assembly, Annette Delfs and Maike Pelzer for the design of the mechanics for the BHM modules, Olaf Hensler and Vahan Petrosyan and Vladimir Rybnikov for their support concerning data acquisition and remote control of the high voltage power source, Petr Smirnov for the design of the readout electronics.

I am grateful for a fruitful long-term collaboration and support in sensor contact fabrication to the Detector Laboratory and the Target Laboratory at GSI. Here I would like to thank Dr. Eleni Berdermann, Michael Träger, Dr. Mladen Kis, Dr. Bettina Lommel and Dr. Birgit Kindler.

I am deeply grateful to my mother, Antonina Ignatenko, for her support and encouragement throughout my entire life, to my wife, Tatiana Gurieva, for her support and understanding during the thesis writing.